
Article:
Tankov, N., Utton, C. orcid.org/0000-0002-1813-8708 and Tsakiropoulos, P. orcid.org/0000-0001-7548-3287 (2025) Directional solidification of a refractory complex concentrated alloy (RCCA) using optical floating zone (OFZ) solidification processing: implications for alloy design and development. Alloys, 4 (4). 29. ISSN: 2674-063X

https://doi.org/10.3390/alloys4040029

---

alloys

MDPI

Article

Directional Solidification of a Refractory Complex Concentrated Alloy (RCCA) Using Optical Floating Zone (OFZ) Solidification Processing: Implications for Alloy Design and Development

Nik Tankov, Claire Utton and Panos Tsakiropoulos *

Department of Materials Science and Engineering, Sir Robert Hadfield Building, The University of Sheffield, Mappin Street, Sheffield S1 3JD, UK; tankof@gmail.com (N.T.); c.utton@sheffield.ac.uk (C.U.)
* Correspondence: p.tsakiropoulos@sheffield.ac.uk

Abstract

Some cast metallic alloys for ultra-high-temperature structural applications can have better mechanical properties compared with Ni-based superalloys. Research on the directional solidification (DS) of such alloys is limited. The production of DS components of these alloys with "tailor-made" microstructures in different parts of the component has not been considered. This paper attempts to address these issues. A bar of the RCCA/RM(Nb)IC with nominal composition 3.5Al–4Crc6Ge–1Hf–5Mo–36Nb–22Si–1.5Sn–20Ti–1W (at.%) was directionally grown using OFZ processing, where the growth rate R increased from 1.2 to 6 and then to 15 cm/h. The paper studies how the macrosegregation of the elements affected the microstructure in different parts of the bar. It was shown that the synergy of macrosegregation and growth rate produced microstructures from the edge to the centre of the OFZ bar and along the length of the OFZ bar that differed in type and chemical composition as R increased. Contamination with oxygen was confined to the "root" of the part of the bar that was grown with R = 1.2 cm/h. The concentrations of elements in the bar were related (a) to each of the parameters VEC, $\Delta\chi$, and δ for different sections, (i) across the thickness and (ii) along the length of the bar, or to each other for different sections of the bar, and demonstrated the synergy and entanglement of processing, parameters, and elements. In the centre of the bar, the phases were the Nb_{ss} and Nb_5Si_3 for all R values. In the bar, the silicide formed with Nb/(Ti + Hf) less or greater than one. There was synergy of solutes in the solid solution and the silicide for all R values, and synergy and entanglement of the two phases. Owing to the synergy and entanglement of processing, parameters, elements, and phases, properties would "emerge" in each part of the bar. The creep and oxidation properties of the bar were calculated as guided by the alloy design methodology NICE. It was suggested that, in principle, a component based on a metallic UHTM with "functionally graded" composition, microstructure and properties could be directionally grown.

Keywords: refractory metal intermetallic composites; refractory complex concentrated alloys; refractory high entropy alloys; macrosegregation; directional solidification; optical floating zone processing; alloy design; alloy development

Academic Editor: Frank Czerwinski

Received: 14 October 2025
Revised: 26 November 2025
Accepted: 2 December 2025
Published: 18 December 2025

Citation: Tankov, N.; Utton, C.; Tsakiropoulos, P. Directional Solidification of a Refractory Complex Concentrated Alloy (RCCA) Using Optical Floating Zone (OFZ) Solidification Processing: Implications for Alloy Design and Development. *Alloys* **2025**, *4*, 29. https://doi.org/10.3390/alloys4040029

1. Introduction

Metallic ultra-high temperature materials (UHTMs) that could replace Ni-based superalloys in the hot sections of gas turbines are materials using (based on) refractory metals

(RMs). Currently, these materials are multiphase RMICs and single-phase or multiphase RHEAs and RCCAs (see the Abbreviations). RMICs include those with Nb and Si additions, i.e., RM(Nb)ICs, also known as Nb silicide in situ composites or Nb silicide-based alloys [1]. Some of the RCCAs or RHEAs are also RM(Nb)ICs owing to their chemical composition, i.e., they are RCCAs/RM(Nb)ICs or RHEAs/RM(Nb)ICs and vice versa (i.e., RM(Nb)ICs/RCCAs or RM(Nb)ICs/RHEAs).

The RHEAs and RCCAs have evolved from the study of high entropy alloys (HEAs) [2], and the RMICs from the study of high-temperature intermetallics [3,4]. The mechanical properties of some multiphase metallic UHTMs with Nb and Si additions meet specific property goals for toughness or creep and have closed the gap with the oxidation property goal [3,4]. To the authors' knowledge, to date there are no metallic UHTMs that simultaneously meet property goals for mechanical and oxidation properties [4]. Components manufactured from metallic UHTMs would require protection with environmental coating systems [1,5], as is currently the case for aerofoils manufactured from Ni-based superalloys [6].

In the aforementioned metallic UHTMs, the phases that make up their microstructures can be "conventional" or high entropy (HE) or complex concentrated (CC, compositionally complex), according to their chemical composition [1]. (HEA and HE phases are those alloys and phases where the maximum and minimum concentrations of elements are not above or below, respectively, 35 and 5 at.%, whereas RCCAs and CC phases are those where the maximum and minimum concentrations of elements are above 35 at.% (up to about 40 at.%) and below 5 at.%). In metallic UHTMs with Nb, Si, and Ti additions, the bcc Nb solid solution can be "normal" or Si-free or Ti-rich [7], and the Nb_5Si_3 silicide can be "normal" or Ti-rich or Ti- and Hf- rich [8] depending on solute partitioning. The said phases in metallic UHTMs can be contaminated with interstitials [3,4,7,9]. The latter are scavenged by specific elements in the alloys, for example, Hf [4].

The alloy design landscape of the alloy design methodology NICE [10] links with risk (IRIS), environment—material interactions (CEMIs), material evolution (ETS), and survivability (ESSERE), see Figures 1 and 2 and Table 1 in [1], and the Abbreviations. In this said alloy design landscape, the processability of metallic UHTMs is not ignored.

In our recent paper [11], we drew attention to the microstructures of the metallic UHTMs alloys OHS1 [12], JZ5 [13], NT1.1 [11], and NT1.2 [9] (see Appendix A for nominal chemical compositions), and suggested that RCCAs with Al, Cr, Ge, Hf, Mo, Nb, Si, Sn, Ti, and W element additions could be suitable for directional solidification (DS) processing. In particular, (a) solute macrosegregation in OHS1 [12], JZ5 [13], NT1.1 [11], and NT1.2 [9], (b) correlations between phases and parameters, (c) the VEC, $\Delta\chi$, and time diagrams, (d) the differences regarding the phases in the as-cast microstructures, and (e) the different stable phases in the said alloys suggest that, with DS, utilising (i) macrosegregation patterns and (ii) solidification parameters, it should be possible to create different microstructures in different parts of a DS component. In other words, in [11] (also, see [4]) it was suggested (1) that it should be possible to produce DS components with "tailor-made" microstructures in different parts of the component, and (2) that this is a challenge for alloy design and development and for solidification processing.

The objective of the research presented in this paper was (a) to perform a preliminary study that addressed for the first time (1) and (2), and (b) to draw attention to some of the issues that, in our opinion, could assist the design of metallic UHTMs suitable for DS processing. Synergy and entanglement of alloy parameters and solute macrosegregation, and thus the importance of solute macrosegregation and entanglement for alloy processability, will be shown for the first time. Also, it will be shown that macrosegregation of solutes and interstitial contamination of microstructures can assist the alloy designer in designing a

component, say an aerofoil, with different chemical compositions and properties across its thickness (i.e., radially) and along its length (i.e., longitudinally). This would be possible owing to solute profiles resulting (i) from macrosegregation and associated relationships between solutes, (ii) between the parameters VEC (number of valence electrons per atom filled into the valence band), $\Delta\chi$ (based on electronegativity), and δ (based on atomic size) in different locations (sections) of a DS rod, (iii) between solutes and said parameters, and (iv) guidance from the alloy design methodology NICE [10] regarding the importance of said parameters for creep and oxidation.

The structure of the paper is as follows. First, we shall ponder on the importance of solidification methods for the processing of metallic UHTMs. Then, because of the limited research on the DS processing of metallic UHTMs, we shall briefly reflect on the DS processing of Ni-based superalloys, for which there is extensive literature, and afterwards we shall review the "state of the art" (i) of the DS of HEAs, RM(Nb)ICs, RCCAs, and RHEAs and (ii) of OFZ processing of advanced materials, with an emphasis (a) on processing parameters in OFZ, with which readers of our paper might not be familiar, and (b) on intermetallics and advanced engineering materials, in order to highlight similarities and differences in processes and material types. Next, the experimental approach of this research will be described, followed by the results and their discussion. Finally, implications of this research for the design and development of metallic UHTMs will be considered.

2. Why Solidification Processing for Metallic UHTMs

The production of metallic UHTMs using solidification processing methods, some of which have been (are) used for the production of Ni-based superalloys, is desirable for a number of reasons [4]. For example, the compressive strength of the multiphase vacuum arc-melted and subsequently directionally solidified RM(Nb)IC alloy Nb–18Si–10Ti–10Mo–15W (at.%) was 650 MPa at 1427 °C [14], and for the multiphase RM(Nb)IC alloys Nb–16Si–22Ti–5Mo–2Cr–2Al–2Hf (at.%) and Nb–16Si–14Ti–5Mo–2Cr–2Al–1W (at.%), which were produced as large buttons/ingots using plasma arc induction melting, the compressive strength properties were σ_{max} = 788 MPa and $\sigma_{0.2}$ = 725 MPa at 1200 °C for the former alloy, whereas the latter alloy had σ_{max} up to 1034 MPa at 1200 °C and 725 MPa at 1500 °C, and $\sigma_{0.2}$ up to 952 MPa at 1200 °C and 680 MPa at 1500 °C [15]. (Note that the aforementioned compressive yield strengths of the said RM(Nb)ICs are superior to those of the denser, vacuum arc-melted RHEAs HfMoNbTaTiZr and HfMoTaTiZr at 1200 °C (556 and 404, respectively, [16]) and of the significantly denser, vacuum arc-melted buttons (of about 10 mm thickness and about 60–70 mm in diameter) RHEAs MoNbTaW (421–506 MPa) and MoNbTaVW (656–735 MPa) in the 1400–1600 °C temperature range [17]). If cast metallic UHTMs can have better mechanical properties compared with Ni-based superalloys, should DS be a feasible and desirable processing route for metallic UHTMs?

The solidification processing of metallic UHTMs faces significant challenges owing to the reactivity of their melts and their high liquidus temperatures (T_L > 2000 °C). Research on the solidification processing of HEAs and metallic UHTMs has investigated methods/techniques used for Ni-based superalloys and high-temperature intermetallics, particularly DS processing, and has also explored modifications to existing methods and alternative methods. For alloys that have T_L significantly higher than those of Ni-based superalloys, solidification processing is limited by the availability of suitable moulds. Instead, cold crucible methods must be used, where the control of thermal gradient (G, see below) is not straightforward.

2.1. Directional Solidification of Ni-Based Superalloys

DS is an established solidification processing method used to manufacture aeroengine and industrial gas turbine hot-section components with directional or single-crystal structures. The original Bridgman and Stockbarger technique [18–20] of DS was further developed by Versnyder and Shank [21] for high-rate solidification and by Giamei and Tschinkel [22] for liquid metal cooling (LMC), and nowadays enables the production of DS turbine blades as well as the study of solidification theories. Alternatives to LMC have been fluidised bed quenching (FBD) [23] or gas cooling casting (GCC) [24]. Chemical inhomogeneities in the structure of DS Ni-based superalloys due to microsegregation and macrosegregation are common. The macrosegregation is linked with channel segregates (usually referred to as freckles) due to multicomponent thermosolutal convective instability above or in the mushy zone.

DS relies on good control of the temperature field and growth rate. The thermal gradient G (for Ni-based superalloys typical values (without LMC, FBD, or GCC) are in the range of 20 to 50 K/cm) and the imposed casting speed R (typical values are in the range of 10 to 25 cm/h) set the cooling rate GR (typical values are in the range of 200 to 1250 K/h) and the ratio G/R (this ratio controls the growth morphology, typical values are in the range of 2 to 3.5 Kh/cm^2), and enable control of the DS microstructure [6,25]. For the DS processing of aeroengine blades, high G is desirable, LMC enables more efficient heat removal and G two to three times higher compared with the Bridgman—Stockbarger process in the 900 to 1500 °C temperature range. For example, G $\leq$ 800 K/cm can be achieved using zone-intensified overheating and LMC, and G = 360 K/cm with R = 90 cm/h [26]. (Note that for functional materials, a low G is desirable to control thermal gradient-induced stresses and associated defects.)

2.2. Directional Solidification of HEAs

In this section we shall consider the DS processing of HEAs for which data about crucibles, G, R, and the use or not of LMC is available; for example, see [27–32]. The processing of HEAs has combined vacuum arc melting and DS. The former method was used to prepare a button/ingot from which rods (diameters 4 mm [28], 6.5 mm [29], 7 mm [30], 9 mm [31], and 10.5 mm [32], and lengths 55 mm [32], 80 mm [30], 85 mm [28,29], and 140 mm [31]) were machined to be subsequently subjected to DS using the Bridgman method. Published research gives data (a) about (i) crucibles (Al_2O_3) [27,29,31,32], (ii) G (100 K/cm [32], 200 K/cm [30], 250 K/cm [28], and 450 K/cm [27]), (iii) R (0.5 to 5 cm/h [32], 1.8 to 72 cm/h [31], 18 to 180 cm/h [28,30], 3.6 to 36 cm/h [29], or 1.8 cm/h [27]), and (iv) heating method (induction heating [27,29]), and (b) about DS with LMC with Ga-In-Sn liquid alloy [27–29,31] or without LMC [30,32], and (c) for the use of Ni-based superalloy seed to grow the DS microstructure of an HEA with a particular orientation [28].

Studied HEAs include (1) single-phase fcc ($CoCrFeNiAl_{0.3}$) or bcc (CoCrFeNiAl) HEAs [27], (2) two-phase (fcc and bcc (A2 and B2)) $Al_{0.7}$CoCrFeNi HEA [28], (3) two-phase CoCrFeNiCu HEA (liquidus and solidus temperatures of 1382 °C and 1107 °C, respectively, with CoCrFeNiCu fcc solid solution and a Cu-rich solid solution) [29], (4) two-phase (fcc + Laves) $CoCrCuFeNiTi_{0.8}$ HEA [30], and (5) eutectic $AlCoCrFeNi_{2.1}$ [31] and $Al_{0.8}CrFeNi_{2.2}$ HEAs [32] (eutectic grains with a lamellar array surrounded by a cellular morphology with anomalous eutectic formation (intercellular regions) and NiAl-rich (B2) and CrFeNi-rich (fcc) phases [32]). (Note that the liquidus temperatures of the aforementioned HEAs are in the range of the liquidus temperatures of Ni-based superalloys).

Macrosegregation in DS HEAs has not been studied or reported; instead, emphasis was given to microsegregation and solute partitioning. In one study [27], the DS processing of the fcc $CoCrFeNiAl_{0.3}$ and bcc CoCrFeNiAl HEAs involved two steps. After the first

step, the same sample was turned by 180° lengthwise, and the DS was repeated under the same conditions as the first step. The as-cast microstructure of the fcc HEA evolved from dendrites to equiaxed grains, then to columnar crystals, and finally to a single crystal. The as-cast microstructure of the bcc HEA evolved from dendrites to equiaxed grains and then to columnar crystals, meaning no single crystal was formed. This difference was attributed to the Al content of the alloys.

2.3. Solidification Processing of Metallic UHTMs

In this section we shall consider the solidification processing of RM(Nb)ICs, RCCAs, and RHEAs. For RM(Nb)ICs, (a) cold crucible-based methods with (i) consumable and (ii) non-consumable electrode vacuum arc melting, or (iii) plasma melting techniques, without or with levitation melting, for example, see [15], and (b) DS techniques were used (for references see Table 2 and Section 3 in [4], and below). For RCCAs and RHEAs, vacuum arc melting with non-consumable W electrode is currently the popular solidification processing technique.

Arc melting is the most widely used method for preparing metallic UHTMs. With non-consumable electrode vacuum arc melting, mostly small buttons (<20 g) are produced for RM(Nb)ICs, RCCAs, and RHEAs. However, for RM(Nb)ICs and RM(Nb)ICs/RCCAs, buttons/ingots up to 1.5 kg in weight have also been produced using non-consumable electrode vacuum arc melting, for example, see [9,33,34], and large ingots using vacuum arc melting. Plasma melting techniques can also produce large buttons/ingots [15]. From large ingots, prototype components can be manufactured [3]. Reproducibility of results obtained from the study of metallic UHTMs produced as small buttons, and "poor-quality" microstructures in vacuum arc-melted ingots (macrosegregation [35], non-uniformity in microstructure), are challenges that must be addressed by alloy development R&D [3,4].

2.3.1. Directional Solidification of RM(Nb)ICs

The DS processing of RM(Nb)ICs has utilised (i) techniques used for the DS of Ni-based superalloys with specified [33,36,37] or unspecified ("suitable", self-made, or "special") crucibles [38,39] that were claimed to withstand higher melt temperatures, with specified LMC [33,36,37] or unspecified LMC [38], or without LMC and with confirmed mould–alloy melt interaction [38]; (ii) a self-made ultra-high temperature and high vacuum DS furnace that could "handle" high-temperature melts with specified R but unspecified G [39–41], (iii) the Bridgman technique with a segmented water-cooled copper crucible (often referred to as electromagnetic cold crucible directional solidification (CCDS) [42]) withdrawn in a controlled manner through an electromagnetic field that is used to induction-levitate the alloy melt in the crucible [3], (iv) the Czochralski technique for containerless growth of specimens using segmented water-cooled copper crucible in which the melt was induction-levitated [3]; or (v) containerless DS with optical floating zone (OFZ) melting techniques, for example, see [43–47]. Techniques (i), (ii), and (v) have combined vacuum arc melting and DS, the former to cast buttons/ingots from which rods were machined and afterwards used for DS. For (i) and (ii), the rods had diameters 3.5 mm [41], 6.8 mm [39,40,48–50], or 14 mm [33,37], and lengths 70 mm [33,50], 75 mm [41,48,49], 78 mm [39,40], or 150 mm [37]. The macrosegregation of solutes that occurs in arc-melted buttons/ingots of RM(Nb)ICs [1] has knock-on effects on the rods that are produced from the as-cast buttons/ingots for subsequent DS study, as noted in [33], or for studies evaluating the suitability of different mould shells for investment casting of RM(Nb)ICs [51]. However, it is not clear if and how this problem has been resolved in different research programmes.

Y_2O_3 crucibles were used for the DS of the RM(Nb)IC alloy Nb–24.7Ti–16Si–8.2Hf–2Cr–1.9Al, (at.%, often referred to as MASC (metal and silicide composite developed by the

General Electric company (GE)), where the alloy melt temperature was about 1850 °C and liquid tin was used for LMC [36]. Al_2O_3 crucibles with high-purity Y_2O_3 applied on the interior wall surface were used for DS of the Nb–15Si–22Ti–2Al–2Hf–2V–2Cr (at.%) and Nb–15Si–22Ti–2Al–2Hf–2V– 14Cr (at.%) RM(Nb)ICs using induction heating to a 1900 °C melt temperature, R equal to 108 cm/h or 216 cm/h, and LMC with liquid Ga-In-Sn [33]. DS of a Nb–22Ti–16Si–6Hf–2Al–2Cr (at.%) RM(Nb)IC was studied using yttria moulds with melt temperatures of 1850 or 1900 °C, R = 36 cm/h, and LMC with liquid Ga-In-Sn [37]. Ma et al. [37] described how the yttria moulds were prepared and confirmed that during DS a reaction layer of HfO_2 and Y_2O_3 formed at the metal–mould interface owing to a reaction between the yttria mould and the Hf-containing RM(Nb)IC. The thickness of the reaction layer depended on both melt temperature and holding time. Though not clearly documented, it is highly likely that interaction between mould and alloy melt also occurred in the research reported by Zhang et al. [33].

Wang et al. [51] investigated the investment casting of the RM(Nb)IC alloy Nb–20Ti–15Si–5Cr–3Hf –3Al (at.%) using different mould shells. They prepared Y_2O_3 mould shells with zirconia face coat and yttria face coats doped with and without CaO + ZrO_2, MgO + ZrO_2, La_2O_3 + ZrO_2, and CeO_2 + ZrO_2, and studied their interactions with the alloy melt held at 1850 °C for 30 min. Wang et al. [51] reported (a) that the interfaces between the alloy and the mould shells with yttria face coats doped with CaO + ZrO_2, MgO + ZrO_2, and La_2O_3 + ZrO_2 consisted of HfO_2 + Y_2O_3 and TiO + HfO_2 reaction layers; (b) that the interface between the alloy and the mould shell with yttria face coats doped with CeO_2 + ZrO_2 consisted of HfO_2 + Y_2O_3 and cubic HfO_2 reaction layers; (c) that a single reaction layer of HfO_2 + Y_2O_3 formed at the interface between the alloy and the pure yttria mould shell; and (d) that the interface between the alloy and the mould shell with a zirconia face coat consisted of a single reaction layer of cubic HfO_2. It was suggested that both pure yttria and yttria doped with La_2O_3 + ZrO_2 mould shells were more suitable for the investment casting of the aforementioned RM(Nb)IC. Note that no comments about macrosegregation were made in [33,36,37,51].

Research on the DS of RM(Nb)ICs using self-made directional solidification facilities (in the papers described as integral directional solidification (IDS)) has been reported by different research groups, for example, see [39–41,48–50]. In one study [39,40], the RM(Nb)IC alloy Nb–22Ti–16Si–6Cr–4Hf–3Al–1.5B–0.06Y (at.%) was cast in an Ar atmosphere using a non-specified crucible with unspecified G, a range of R values, namely 1.8, 3.6, 5.4, 10.8, 18, 28.8, and 36 cm/h, maximum melt temperature of 2000 °C, and LMC using a Ga-In-Sn alloy melt at 700 °C. HfO_2 was formed in the as-cast microstructure. The authors claimed that the "axial thermal gradient during IDS would be higher than those during either floating zone melting or cold crucible Czochralski processes" [40]. In a separate study [41], the RM(Nb)IC alloy Nb–15Si–22Ti–5Cr–3Al–3Hf (at.%) was cast in an Ar atmosphere using unspecified crucible and G with the alloy melt at 2050 °C and LMC (a Ga-In-Sn alloy). The alloy was first withdrawn at 36 cm/h for 3 cm, then the withdrawal rate was abruptly decreased to 3.6 cm/h for 3 cm, followed by LMC. In a separate experiment, the alloy was directionally solidified at 3.6 cm/h for 5 cm and then quenched. The same alloy was cast using the same facility but with higher R values, namely 36, 72, 108, 180, and 360 cm/h [48,49]. Changes in the cast microstructure, for example, morphology and crystallographic orientation of phases [49], were accompanied by segregation of Cr and Ti, which initially increased and then decreased with increasing R [48].

Regarding the Bridgman technique with segmented water-cooled copper crucible, ingots up to 3.5 cm in diameter of the MASC alloy have been produced [3], and the RM(Nb)IC alloy Nb–12Si–24Ti–4Cr–4Al–2Hf (at.%) has also been studied [52,53]. Using this Bridgman technique, control over the alloy microstructure was claimed to be inferior compared with

the Czochralski technique [3]. Data for the former technique is limited [42,52,53], and the same applies to the latter [3,54,55]. According to Wang et al. [42], a flat solid/liquid (S/L) interface is required to achieve a directionally solidified microstructure in industrial-sized ingots processed with electromagnetic CCDS. A simulation of electromagnetic CCDS of the RM(Nb)IC alloy Nb–16Si–22Ti (at.%) regarding the shape of the S/L interface at various temperature gradients during the initial melting stage indicated that processing at 50 kHz and 2400 A would give a nearly flat S/L interface [42]. Compared with DS, IDS, Czochralski, and OFZ techniques, CCDS can achieve higher G values and produce larger ingots with (claimed) lower interstitial contamination [42].

For the CCDS of the RM(Nb)IC alloy Nb–12Si–24Ti–4Cr–4Al–2Hf (at.%), the alloy was first prepared using vacuum arc melting with a non-consumable tungsten electrode, followed by induction skull melting. Rods about 22 mm in diameter and 170 mm in length were cut by electrical discharge machining (EDM). The CCDS device used in [53] was equipped with a pool of liquid Ga–In alloy, as was the case in [56]. Casting was performed in an Ar atmosphere with a withdrawal rate into the Ga–In alloy pool of 7.2 cm/h [53]. Note that the CCDS experimental setup used in [53] was the same as that used for the CCDS of a Ti–47Al–2Cr–2Nb (at.%) alloy, in which case the thermal gradient G was 240 K/cm [56]. The CCDS ingot of the RM(Nb)IC alloy consisted of four parts that had different morphologies: the non-melt (NM) zone, the initial transient (IT) zone, the steady-state growth (SSG) region, and the final solidification (FS) zone. The NM zone, with equiaxed micromorphology, was the RM(Nb)IC alloy bed which supported the molten pool at the start of DS. In the IT zone, a transition occurred from equiaxed morphology to DS morphology. In the SSG zone, the DS microstructure was parallel to the withdrawal direction. Finally, the solidification front was frozen (FS zone) when melt feed ended [53].

With the Czochralski technique, DS samples approximately 10 mm in diameter and approximately 100 mm long were prepared, see [54,55]. The alloy studied by GE researchers was directionally solidified by lowering a seed crystal of the same alloy into the melt and withdrawing the seed at a constant and controlled rate (typically in the range of 3 to 90 cm/h depending on alloy and desirable structure). During DS, the temperature gradient in the crystal and the temperature distribution in the melt were monitored using an infrared camera; however, no data about G is available. When volatile elements were present in the alloy, directional solidification was performed under an atmosphere of ultrahigh-purity argon (total impurity content less than 0.75 ppm). When an argon atmosphere was used, before melting the charge, the chamber containing the cold crucible was evacuated to a vacuum better than 10^{-5} Torr in order to minimise contamination of the DS sample with interstitial elements such as oxygen, nitrogen, and hydrogen.

2.3.2. Directional Solidification of RHEAs and RCCAs

Zhang et al. [57] studied the suitability of different refractories, namely Al_2O_3, MgO, and $BaZrO_3$, for the DS of a TiZrNbV RHEA and reported (i) that interaction occurred between each refractory and the molten alloy, and (ii) that $BaZrO_3$ exhibited the best resistance. In particular, (a) the attack of Al_2O_3 was severe and resulted in the formation of a 400 μm thick interaction layer and Zr oxides, (b) MgO formed a 50 μm thick interaction layer and Zr oxides, whereas (c) BaZrO3 formed no reaction products. The authors pointed out that RCCAs could be produced using $BaZrO_3$ refractory. Note (1) that $BaZrO_3$ has a congruent melting point in the range of 2600 to 2700 °C, and (2) that He et al. [58] reported that $BaZrO_3$ refractory was suitable for DS processing of TiAl. To the authors' knowledge, DS of RCCAs and RHEAs has not been attempted using the aforementioned methods and techniques.

2.4. Directional Solidification Processing of Materials Using OFZ Melting

Optical floating zone (OFZ)-based processing has been used extensively for the containerless growth (DS) of bulk or single-crystal metal oxides, e.g., [50], intermetallics, e.g., [59–61], and much less for metallic alloys, e.g., [62–66], and RM(Nb)ICs, e.g., [43–47,67,68]. The key processing parameters in OFZ are the growth rate, the growth atmosphere and gas pressure, the temperature gradient within the sample, the molten zone temperature, and the rotation rate. The quality of the feed rod is also important. Data to guide the OFZ processing of materials to achieve desirable properties for a particular application are very limited owing to the nonexistence of comprehensive studies of the effect(s) changes in the aforementioned parameters have on the directional solidification of said materials. Also, the availability of OFZ facilities is limited worldwide.

In OFZ furnaces, one or more ellipsoidal or parabolic mirrors are used to focus the light from halogen or xenon lamps onto a vertically held rod-shaped sample to produce a molten zone, which is then moved along the sample to grow (directionally solidify) a bulk or single crystal. Four mirrors increase the power of the furnace and give more uniform sample heating. A non-porous and straight feed rod of constant diameter is crucial in OFZ processing.

From the literature about materials that were grown (directionally solidified) using OFZ processing, we can infer the following: (1) Used growth rates in OFZ were in the range 0.005 cm/h to 24 cm/h, most reported rates were in the range 0.01 to 5.5 cm/h, and most commonly used rates were in the range 0.1 to 1 cm/h. (2) Metallic materials were processed in high-purity Argon atmosphere. (3) A lower growth rate was more likely to give a planar S/L front and a more stable molten zone. (4) Type of image furnace, sample dimensions, material physical properties (e.g., thermal conductivity and anisotropic thermal expansion), type of atmosphere and pressure, lamp defocusing, and secondary radiation from the sample affected the temperature gradient. (5) A large temperature gradient along the growth direction could cause thermal stresses and cracks in the solidified material. (6) A steep temperature gradient could help to reduce the length of the melting zone and lead to a more stable zone. (7) The temperature gradient along the sample could control the shape of the S/L interface. (8) A four-ellipsoidal-mirror furnace could give a smaller radial temperature gradient in the sample than a single-mirror or double-mirror type image furnace. (9) The opacity of the material affected the shape of the S/L interface; convex S/L interfaces formed in opaque materials. (10) Rotation ensured melt homogeneity and a more homogeneous temperature distribution within the melt. (11) A higher rotation rate was an effective way of achieving a more stable molten zone. (12) The effect of rotation was not considered in many studies.

Xu et al. [60] claimed that the (calculated) steep temperature gradient of 750 K/cm, typical of the vertical floating zone melting technique, is a prerequisite for the control of the morphological instability of the crystal/melt interface at moderate growth rates. They used a URN-2-ZM (National Research University, Moscow Power Engineering Institute (MPEI), Krasnokazarmennava 14, Moscow 111250, Russia) furnace with a vertical double-ellipsoid optical configuration and a 5 kW air-cooled xenon lamp to grow Tb_5Si_3 single crystals about 6 mm in diameter and up to 30 mm in length under a 0.1 MPa flowing Ar atmosphere, with axially symmetric counter-rotation of the crystal (30 rpm) and feed rod (10 rpm) and a growth rate of 0.3 cm/h, in which the operating temperature of the floating zone and longitudinal temperature profiles were measured in situ with a two-colour pyrometer using a stroboscopic method. Using the same facility with the same processing setup and conditions as in [60], Xu et al. [62] grew Gd_2PdSi_3 single crystals where the temperature gradient was about 800 K/cm. Cao et al. estimated that the temperature gradient during

the OFZ growth of $ErPd_2Si_2$ single crystals was about 350 K/cm [61]. For OFZ-grown Cr-Cr_3Si eutectic, the temperature gradient in the hot zone was about 250–330 K/cm [67].

The effects of longitudinal and radial segregation on functional properties of OFZ-grown single crystals of $HoNi_2B_2C$ were studied in [69]. In the same study, "sizeable macrosegregation" was suspected in floating zone-grown single crystals of $CeSi_x$, but the macrosegregation was not investigated.

OFZ Processing of Metallic UHTMs

For the OFZ processing of metallic UHTMs, rods of 8 mm [45,47] or 10 mm [44] diameter and 70 mm [45,47] or 80 mm [44] length were machined from vacuum arc-melted buttons/ingots. Rods were directionally solidified in high-purity Argon atmospheres using unspecified image furnace type and temperature gradients, and with growth rates of 0.3, 0.5, 1, and 1.8 cm/h for the RM(Nb)IC alloy Nb–17Si–10Mo–3Al [43], or 1 and 10 cm/h for the Nb–17.5Si and Nb–10Ti–17.5Si (at.%) alloys [46], or 0.9 cm/h for the RM(Nb)IC alloy Nb–22Ti–16Si–7Cr–3Al–3Ta–2Hf–0.1Ho (at.%) [47]. The near-eutectic composition RM(Nb)IC alloy Nb–21.1Si–8.3Ti–5.4Mo–4W–0.7Hf (at.%) was processed using an image furnace with four xenon lamps, with counter-rotation of the support and feeder rods at 30 rpm and pulling of the system downwards at three different velocities of 1.2, 6, and 15 cm/h [44]. The growth rates used in [44] and in [45–47] were significantly lower than those in arc melting. Indeed, in the OFZ facility used in [44], a growth rate of 420 cm/h (not employed in [44]) is comparable to that in arc melting [70].

Based on their results for the DS processing of the RM(Nb)IC alloy Nb–21Ti–16Si–7Cr–3Al–2Hf (at.%) with an FZ-35WHV OFZ furnace under an Ar atmosphere with growth rates of 0.3, 0.5, 0.8, and 1.2 cm/h., Huang et al. [68] suggested (i) that the longitudinal continuous growth of silicides was destroyed gradually with increasing growth rate, (ii) that low growth rate was beneficial to coupled growth, (iii) that when the growth rate was too low, such as 0.3 cm/h, because of the low temperature gradient, growth of silicides developed along the transversal direction, resulting in coarse silicides, and (iv) that a growth rate of 0.5 cm/h was appropriate to realise coupled growth of Nb_{ss} and silicide and the simultaneous formation of silicides with high aspect ratio.

In summary, the brief review of literature on the directional solidification of HEAs and metallic UHTMs shows (i) that control of the solidification processing parameters has been possible only in the case of HEAs with liquidus temperatures not significantly different from those of Ni-based superalloys, which enabled the use of existing DS facilities and setups (meaning crucibles, G and R values, and LMC alloys) used for the latter materials, (ii) that self-made DS facilities with alternative crucibles enabled the solidification processing of RM(Nb)ICs with liquidus temperatures not exceeding 1950 °C but without avoiding alloy—crucible interaction(s), (iii) that all DS studies of HEAs and RM(Nb)ICs have used as starting material cylindrical rods machined from arc-melted buttons/ingots with dimensions in the ranges 3.5 mm to 22 mm diameter and 55 mm to 170 mm length, (iv) that R values for RM(Nb)ICs have been in the range 1.8 cm/h to 360 cm/h, which is wider than the typical range for Ni-based superalloys and HEAs, (v) that R values were in a significantly narrower range of 0.3 cm/h to 15 cm/h when OFZ processing was used for RM(Nb)ICs, (vi) that high-temperature gradients were possible in floating zone processing, (vii) that in some studies, alloys were "grown" using DS with different (increasing) R values in the same experiment, (viii) that macrosegregation has not been studied in the DS processing of HEAs and RM(Nb)ICs, and (ix) that DS of an RHEA has been attempted only regarding the study of crucible material(s).

3. Experimental

The RCCA/RM(Nb)IC with nominal composition 3.5Al–4Cr–6Ge–1Hf–5Mo–36Nb–22Si–1.5Sn–20Ti–1W (at.%, alloy NT1.2) was selected for this research. Owing to the strong macrosegregation of Si, Ti, and other elements in the buttons/ingots of this alloy, see [9], rods (9 mm diameter and 80 mm length) for the DS experiments were machined using electrical discharge machining (EDM) from the central part of the button/ingot where the macrosegregation was minimal, see Figure 1 in [9]. The OFZ solidification processing was performed in an FZ-T-12000 Crystal Systems optical furnace with four Xenon lamps, at the Rolls-Royce University Technology Centre (UTC) in Advanced Materials at the University of Cambridge. The rods were sectioned into two pieces, one to act as a seed rod and the other as the feed rod that was to be directionally solidified.

The seed and feed rods were held in place using refractory wires and were sealed inside a quartz glass tube, see Figure 1. The seed rod was 30 mm in length. High-purity Argon was continuously fed through the bottom of the quartz tube. The rods and molten zone inside the quartz tube were kept at 6 bar pressure. The lamps (maximum 4 kW each) and mirrors surrounding the quartz tube were exposed to the laboratory atmosphere. The seed and feed rods were rotated at 15 rpm counter to each other; this was the optimum rotational speed to allow adequate mixing in the liquid phase while maintaining stability of the floating zone. The four Xenon lamps, operating from 54% up to 64.5% power, were used with circular mirrors to focus light into a molten zone that was approximately disc-shaped, about 3 mm in height and 20 mm in diameter. Material was fed into the molten zone at the top and drawn out and solidified (grown) at the bottom at different rates, namely 1.2 cm/h, 6 cm/h, and 15 cm/h. Note that the experimental parameters used in this research did not differ from those used in previous research on the DS processing of metallic materials (see Section 2).

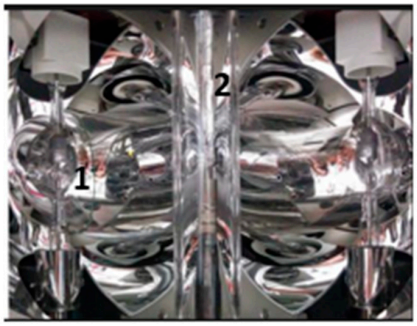

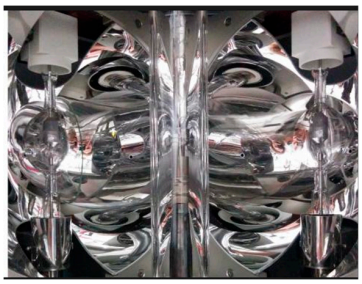

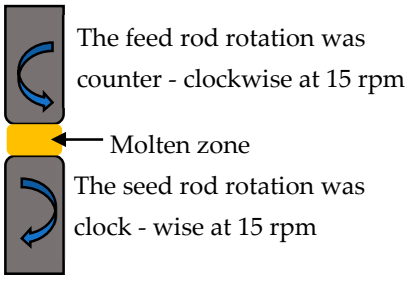

Figure 1. (**Left**) View of the optical floating zone furnace, one Xenon lamp, and two glass tubes (image used with kind permission from the Rolls-Royce UTC in Advanced Materials at the University of Cambridge). (**Right**) Schematic showing the molten zone and the seed and feed rods.

The melting was initiated with 54% lamp power, and when a stable molten zone was achieved, the power was turned down to 52%. The sample was moved downwards at 1.2 cm/h, i.e., the floating molten zone travelled upwards at 1.2 cm/h. After moving the molten zone for approximately 11 mm at 1.2 cm/h, the assembly movement speed,

and hence the solidification (growth) rate, was changed to 6 cm/h, and the power was increased to 59% to sustain a faster-moving molten zone. During the 6 cm/h growth rate, the molten zone showed signs of instability (wobbling left and right). The molten zone was stabilised when the power was increased to 64.5%. After approximately another 11 mm, the movement speed of the assembly, and hence solidification (growth) rate, was changed to 15 cm/h. The lamp power remained at 64.5%. The solidification (growth) rate was kept at 15 cm/h for a further 5.5 mm, after which the lamps were turned off, the process stopped, and the sample was allowed to cool to room temperature with a continuous argon flow. The duration of the whole process was 2.5 h.

For the characterisation of the alloy, specimens were cut and mounted in conductive Bakelite. Grinding was performed using silicon carbide sandpaper with successive grit of P800, P1200, P2400, and P4000, and polishing was performed with 1 µm diamond suspension, followed by a final polish using 50 nm diamond suspension. Scanning electron microscopes (SEMs) equipped with back-scatter detector and energy-dispersive detector were used for imaging and quantitative analysis. XL30 Philips FEG and InspectF FEG SEMs were used for imaging and quantitative chemical analysis. The EDS with standards (elemental standards for all elements and Forsterite (O: 45.5%, Mg: 34.5%, Si: 20.0%) and alumina for oxygen) was performed on the XL30 FEG SEM using INCA Oxford Instruments analysis software, with 20 kV per channel. Acquisition duration and processing time were optimised to maintain good spectral resolution with a count rate of 40 kcps and a dead time of up to 20%. For both EDS and BSE imaging, the aperture was set to 3 and the spot size to 5.

4. Results and Discussion

Figure 2a shows the DS rod of the RCCA/RM(Nb)IC alloy NT1.2 after OFZ processing with three different rates. The strong discolouration at the start of the rod and the early stages of growth with rate R = 1.2 cm/h (right-hand side of the figure) occurred because of contamination with oxygen. The latter was scavenged by Hf and resulted in the formation of HfO_2 near the edge of the rod (see below). Note that the diameter of the rod changed when the growth rate was increased.

The average chemical composition of each part of the rod and the "termination" at the very end, on the left-hand side of the rod shown in Figure 2a, is given in Table 1. All the average chemical compositions corresponded to an RCCA. The standard deviation values in Table 1 indicated strong macrosegregation of elements, particularly for the 1.2 and 6 cm/h growth rates (see below). Note the decrease in the standard deviation values of elements as the growth rate increased and in the "termination". Figure 2b is a schematic of the rod showing the growth direction and where the microstructure was studied.

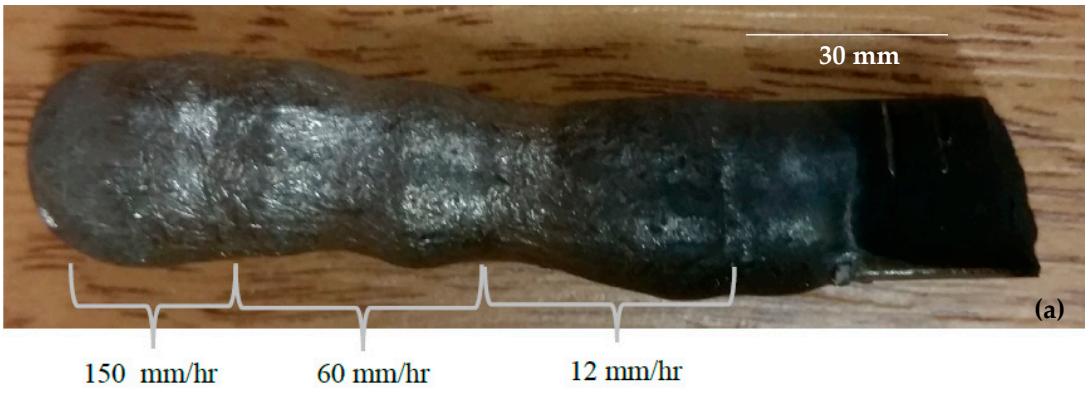

Figure 2. *Cont.*

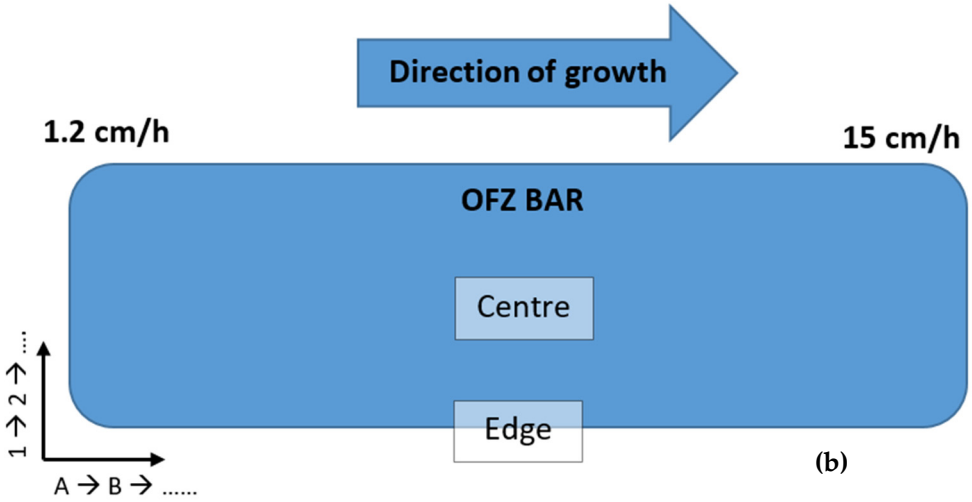

Figure 2. (**a**) Image of the bar (rod) of the RCCA/RM(Nb)IC alloy NT1.2 after it was directionally solidified with three different growth rates using OFZ processing. The original rod dimensions were 9 mm diameter and 80 mm length. (**b**) Schematic of the rod showing the growth direction from low-to-high R, locations (sections) A, B, etc., from start (A) of growth and locations 1, 2, etc., and from edge (1) of rod towards its centre/bulk (4). The last location (section) for R = 1.2 cm/h (i.e., before the onset of R = 6 cm/h) was section G. The last location (section) for R = 6 cm/h and 15 cm/h was section E (see text). Part of the seed rod is shown on the right-hand side of the bar (black colour part) in (**a**).

Table 1. (**a**) Chemical composition (at.%) (average value and standard deviation) of each part of the rod and for the "termination". The data for R = 1.2 cm/h is from the non-contaminated with oxygen areas, see text below. (**b**) Solute ratios for the different growth rates and the termination. TM = Cr + Hf + Ti, RM = Mo + Nb + W, and SM = Al + Ge + Si + Sn.

(**a**)

R (cm/h)	Nb	Ti	Si	Al	Cr	Hf	Mo	W	Sn	Ge
1.2	36.7 ± 1.9	19.9 ± 1.8	19.7 ± 4.7	3.9 ± 1.1	4.6 ± 2.3	1.1 ± 0.4	6.4 ± 1.3	1 ± 0.4	1.8 ± 0.8	4.9 ± 0.9
6	37.5 ± 0.7	19.4 ± 1.5	20.5 ± 5.3	3.9 ± 0.9	3.4 ± 1.4	1.1 ± 0.2	6.7 ± 2.2	1.1 ± 0.7	1.2 ± 0.4	5.2 ± 0.9
15	37.9 ± 0.9	19.7 ± 1.3	22.7 ± 2.5	2.9 ± 0.6	3.1 ± 0.9	1.1 ± 0.1	5.9 ± 0.8	0.7	0.7	5.3 ± 0.3
termination	37.9 ± 0.4	19.2 ± 0.5	22.7 ± 1.2	2.9 ± 0.4	3.2 ± 0.4	1 ± 0.1	6.1 ± 0.4	0.8	0.8	5.4 ± 0.2

(**b**)

Solute Ratios	R = 1.2 cm/h	R = 6 cm/h	R = 15 cm/h	termination
(TM + RM)/SM	2.3	2.25	2.25	2.14
RM/TM	1.72	1.9	1.9	1.91
RM/SM	1.46	1.47	1.47	1.41
TM/SM	0.84	0.78	0.78	0.74

Owing to macrosegregation (see below) and the synergy and entanglement of parameters and solutes [1,35], and of the phases that formed (see below, and Figure 29 and Table 7 in [11]), the chemical composition of the part of the rod that was grown with R = 1.2 cm/h was close to that of the alloy NT1.2-AC [9] regarding the elements Al, Hf, Nb, Ti, and W, close to that of the alloy NT1.1-AC [11] for Cr, Ge, Hf, Ti, and W, and close to that of the alloy JZ5-AC [13] for Cr, Hf, Mo, Si, and W, whereas for R = 6 cm/h it was close to that of NT1.2-AC for Al, Cr, Hf, Sn, Ti, and W, close to NT1.1-AC for Ge, Hf, Mo, Si, Ti, and W, and close to that of JZ5-AC for Ge, Hf, W, and Mo. For R = 15 cm/h and the termination, the chemical composition was close to that of NT1.2-AC for Hf, Si, Ti, and W, close to that of NT1.1-AC for Ge, Hf, Ti, and W, and close to that of JZ5-AC for Ge, Hf, and W. (See Appendix A for alloy chemical compositions).

Table 1b, which is based on the chemical analysis data given in Table 1a, shows how the ratios (TM + RM)/SM, RM/TM, RM/SM, and TM/SM changed as the growth rate increased from 1.2 cm/h to 15 cm/h, and in the termination. Notable changes occurred as the growth rate increased (a) from R = 1.2 cm/ to 6 cm/h for the RM/TM and TM/SM ratios, of which the former increased and the latter decreased, and (b) from R = 1.2 cm/h to R = 15 cm/h for the (TM + RM)/SM ratio, which decreased. The ratios did not change from R = 15 cm/h to the termination.

For R = 15 cm/h and the termination, the ratio TM/SM was the same as for the RCCAs/RM(Nb)ICs alloys JZ5, NT1.1, and NT1.2. The ratio RM/TM was the same as for NT1.2 for R = 1.2 cm/h and R = 15 cm/h, but the (TM + RM)/SM and RM/SM ratios were higher compared with the alloys JZ5, NT1.1, and NT1.2 (see Table 7 in [9]). The data in Table 1b suggest that the solidification processing method (clean melting and directional solidification with OFZ in this case) "has an effect on" the (TM + RM)/SM and RM/SM ratios. Note that the (TM + RM)/SM ratio is important for the creep of metallic UHTMs (see Section 2.5 in [10]). The XRD data can be found in [9,11,13]. Linkage between chemical analysis data (EPMA, EDS) and XRD data regarding phase identification can be found in [10] and references within.

4.1. Growth Rate of 1.2 cm/h

The concentration profiles of each element from the edge of the rod towards the centre (bulk) of the rod (see Figure 2b) are shown in Figure 3.

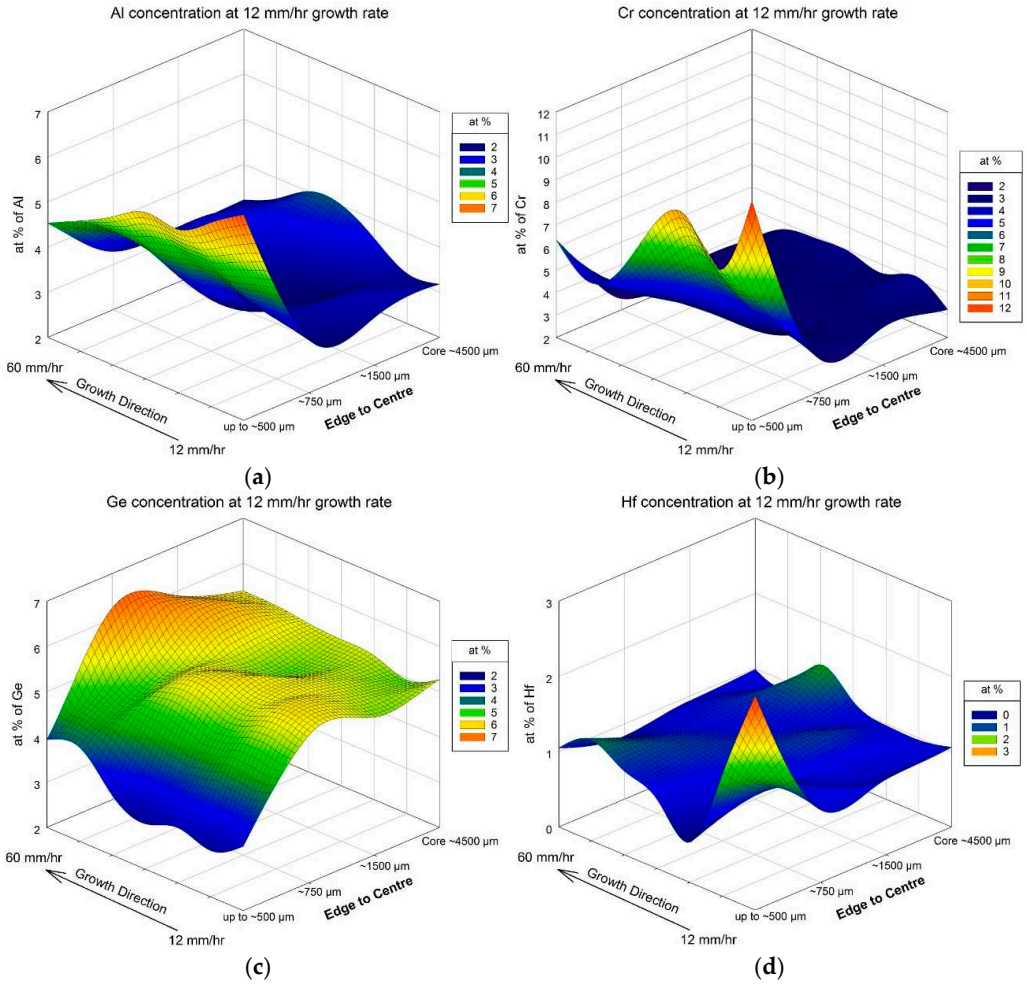

Figure 3. *Cont.*

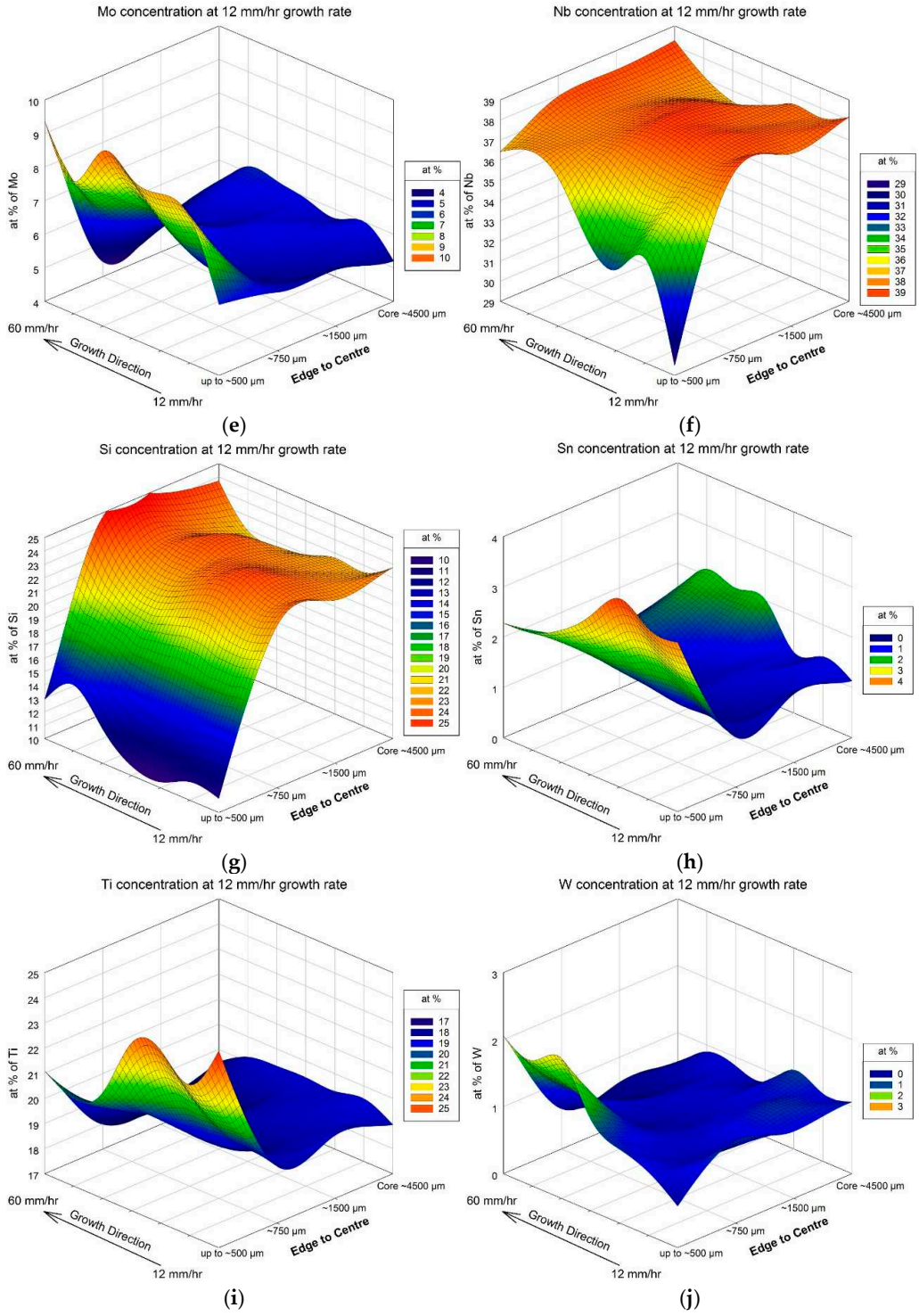

Figure 3. Concentration profiles of elements of the alloy NT1.2 that was directionally solidified using OFZ processing with growth rate of 1.2 cm/h: (**a**) Al, (**b**) Cr, (**c**) Ge, (**d**) Hf, (**e**) Mo, (**f**) Nb, (**g**) Si, (**h**) Sn, (**i**) Ti, and (**j**) W.

The concentrations of Al, Cr, Hf, Mo, Sn, Ti, and W were high near the edge of the rod, whereas those of Ge, Nb, and Si were low. At the start of directional solidification with growth rate of R = 1.2 cm/h, a transition in the microstructure occurred from the edge towards the centre (bulk) of the rod, as shown in Figure 4a,b. The transition was observed from location A to location G (see Figure 2b). However, from location E towards location G, the transition became less well-defined but was still noticeable.

Table 2. Chemical composition (at.%) of phases in the contaminated area, Figure 4c,d. The data for the Nb_{ss} is for the microstructure shown in Figure 4d.

Phase	Nb	Ti	Si	Al	Cr	Hf	Mo	W	Sn	Ge
Ti-rich A15-Nb_3X	33.3 ± 2.8	28.7 ± 2.1	2.6 ± 1.1	8.6 ± 0.9	6.7 ± 0.4	-	8.9 ± 0.1	0.7	9.2 ± 0.8	1.3 ± 0.2
$NbCr_2$ Laves	24.6 ± 0.2	12.1 ± 0.7	7.7 ± 1.2	5.5 ± 0.3	46 ± 0.4	-	3.1 ± 0.3	-	-	1
Nb_5Si_3	40.6 ± 0.5	16 ± 0.2	30 ± 0.4	1.9 ± 0.4	0.8	1	3.8 ± 0.1	-	-	5.9 ± 0.2
Ti-rich Nb_5Si_3 Nb/(Ti + Hf) > 1	31.7 ± 1.8	25.4 ± 1.7	22.1 ± 2	4.9 ± 0.5	2.9 ± 0.3	1	2.6 ± 0.2	-	3 ± 0.2	6.4 ± 0.3
Ti-rich Nb_5Si_3 Nb/(Ti + Hf) < 1	24.4 ± 1.1	33 ± 2.5	24.3 ± 0.5	4.9 ± 0.4	3.1 ± 0.3	1	1.9 ± 0.1	-	-	7.4 ± 0.4
Ti_{ss}	2.2 ± 0.2	96.5 ± 0.6	0.7	0.6	-	-	-	-	-	-
Nb- and Cr-rich silicide	25.1	21	15.7	5.4	25.9	-	3	-	-	3.9
Ti-rich silicide	13.9	50.5	16.6	5.8	5.1	-	1.3	-	1	5.8
Nb_{ss}	38.4 ± 1.2	25.3 ± 1	0.8	5.3 ± 0.6	11.8 ± 0.8	-	12.1 ± 1	2.3 ± 0.2	3 ± 0.3	1 ± 0.2
Ti-rich Nb_{ss}	25.1 ± 0.9	33.6 ± 1.1	2 ± 0.6	12.1 ± 0.4	14.4 ± 0.6	-	9.7 ± 0.9	1.1 ± 0.3	2.1 ± 0.2	-

Table 3. Chemical composition (at.%) of the Nb_{ss} and A15-Nb_3X phases in Figure 4b.

Phase	Nb	Ti	Si	Al	Cr	Hf	Mo	W	Sn	Ge
Nb_{ss}	37.1 ± 0.8	23.1 ± 0.8	0.5	6.7 ± 0.3	12.3 ± 0.8	-	14.9 ± 0.5	2.8 ± 0.4	2.6 ± 0.3	-
A15-Nb_3X	39.1 ± 0.8	21.3 ± 1.7	4.3 ± 0.1	7 ± 0.3	7.1 ± 0.6	-	10.7 ± 0.9	1.1 ± 0.4	7.5 ± 0.6	1.9 ± 0.1

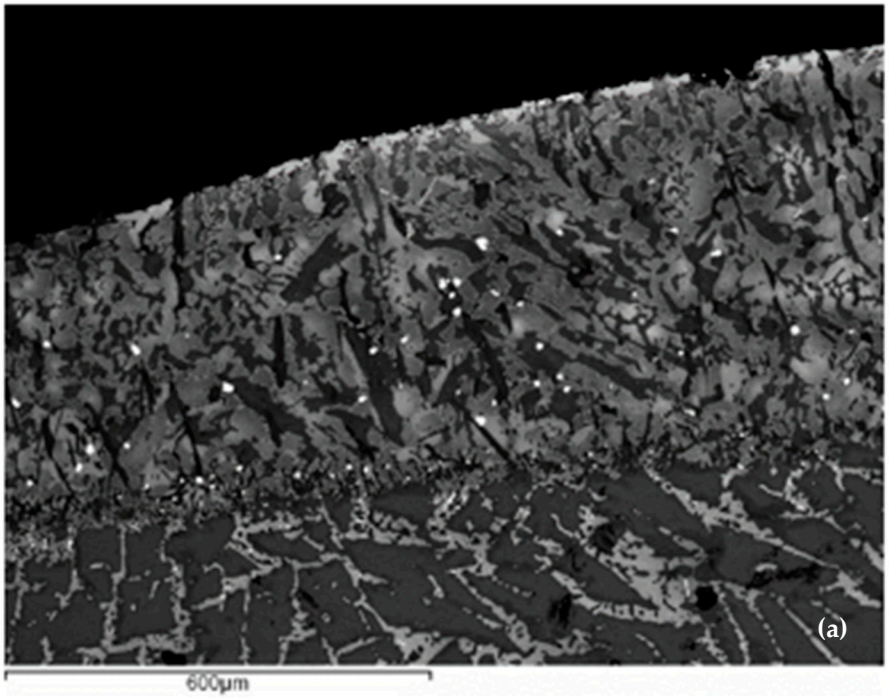

Figure 4. *Cont.*

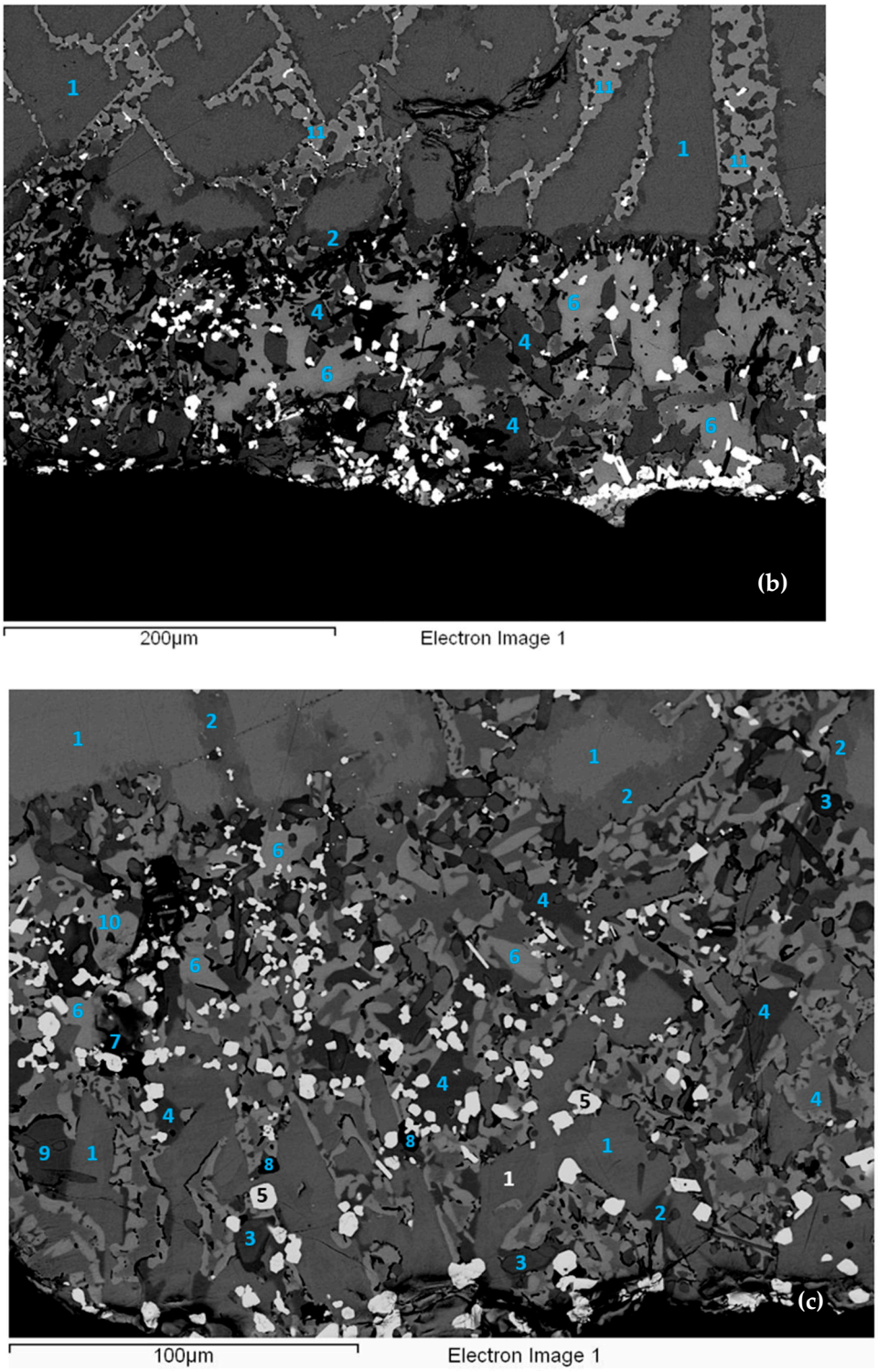

Figure 4. *Cont.*

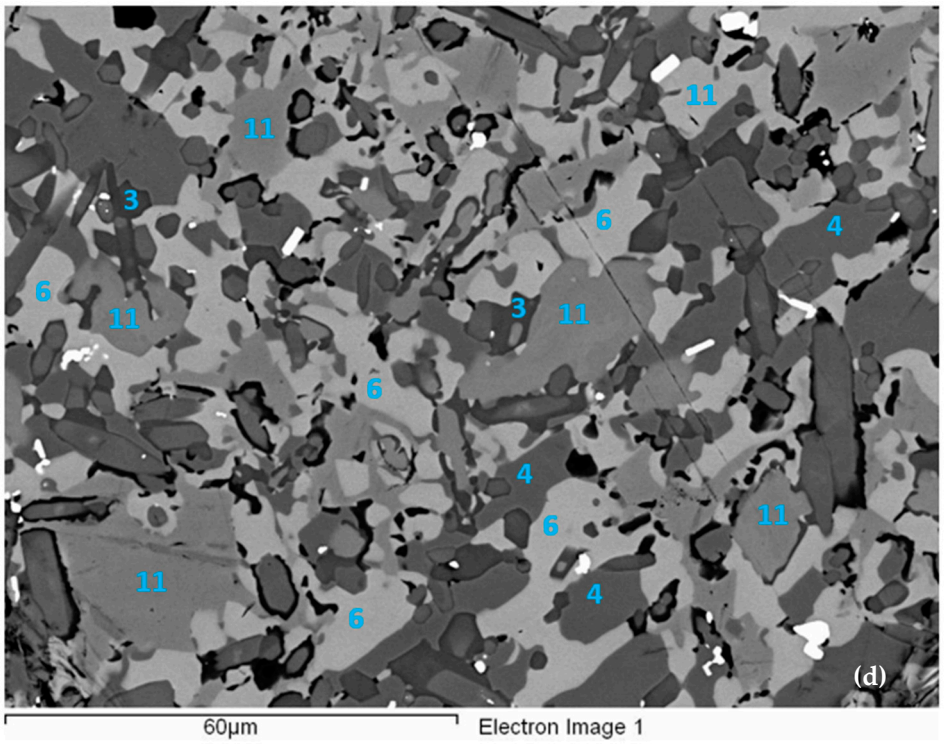

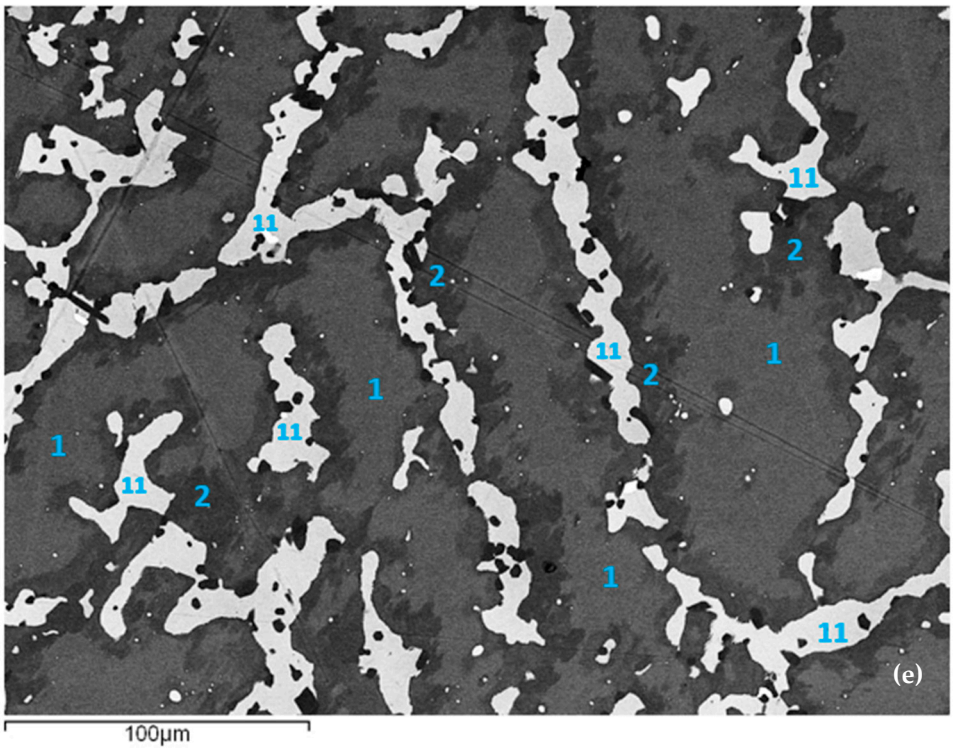

Figure 4. *Cont.*

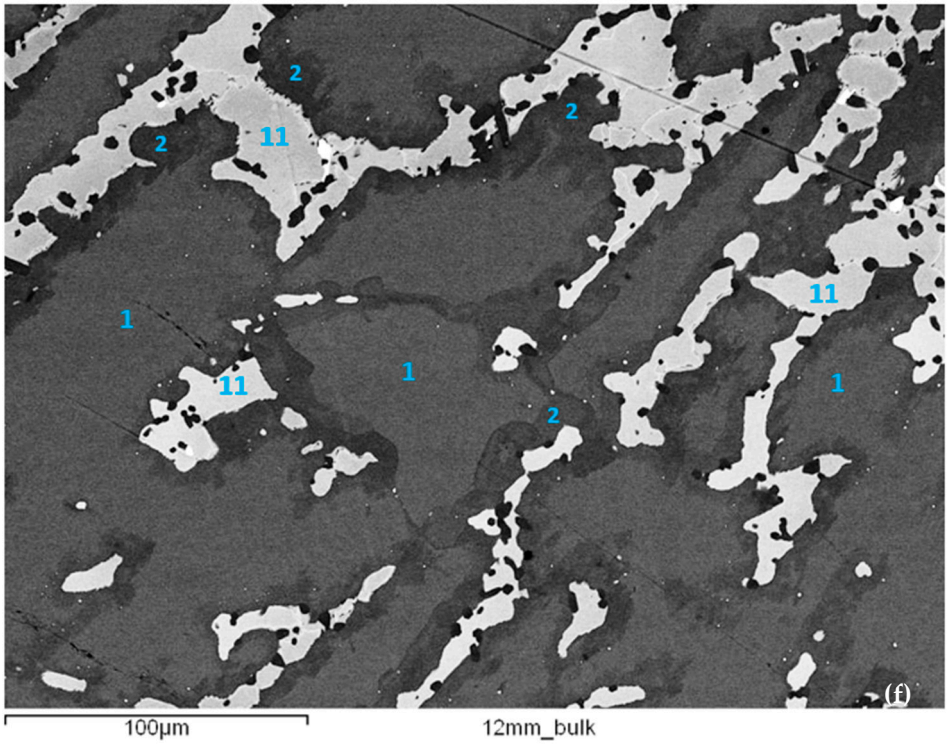

Figure 4. Back-scatter electron (BSE) images of the RCCA/RM(Nb)IC alloy NT1.2 that was directionally solidified using OFZ processing with growth rate of R = 1.2 cm/h: (**a**,**b**) show transition in the microstructure at the edge of the rod which was contaminated with oxygen, (**c**,**d**) show phases formed in the contaminated area, and (**e**,**f**) show the microstructure in the centre (bulk) of the rod. Phases are identified with numbers as follows: 1 = silicide, 2 = Ti-rich silicide with Nb/(Ti + Hf) > 1, 3 = Ti-rich silicide with Nb/(Ti + Hf) < 1, 4 = $NbCr_2$ Laves phase, 5 = hafnia, 6 = A15–Nb_3X, 7 = Ti-rich A15–Nb_3X, 8 = Ti_{ss}, 9 = Nb- and Cr-rich silicide, 10 = Ti-rich silicide, and 11 = Nb_{ss}. For chemical composition of phases, see text and Tables 2–4.

Table 4. Chemical composition (at.%) of the phases in the centre (bulk) of the rod (Figure 4e,f).

Phase	Nb	Ti	Si	Al	Cr	Hf	Mo	W	Sn	Ge
Nb_{ss}	37.8 ± 2.2	20.9 ± 1.6	1.3 ± 0.1	5.5 ± 0.5	13.2 ± 2.3	-	15.4 ± 2	2.8 ± 0.8	2.6 ± 0.1	0.5
Nb_5Si_3	36.7 ± 2.9	20.5 ± 2.1	26.6 ± 0.4	3.8 ± 0.6	1.7 ± 0.4	1.3 ± 0.6	2.4 ± 0.6	-	-	7.0 ± 0.6
Ti-rich Nb_5Si_3 Nb/(Ti + Hf) > 1	31.7 ± 1.9	26.1 ± 1.9	23 ± 1.8	5.2 ± 0.9	2.5 ± 0.4	1 ± 0.2	2.3 ± 0.2	-	2.2 ± 0.8	6 ± 0.2

There was contamination of the microstructure with oxygen, which was scavenged by Hf that formed hafnia (white phases in Figure 4a–d), and different phases formed in the contaminated areas and between the edge and centre (bulk) of the rod. The chemical composition of phases in Figure 4c,d is given in Table 2. Solid solution (Nb_{ss}) was not observed in all sections. For example, no Nb_{ss} was observed in the microstructure shown in Figure 4c but solid solution was observed in the microstructure shown in Figure 4d. Note that the data for the Nb_{ss} in Table 2 are for the solid solution shown in Figure 4d. The chemical composition of phases in the microstructures shown in Figure 4b,e,f are shown, respectively, in Tables 3 and 4.

The typical microstructure at the locations (and sections starting at) A1 to C1 (i.e., at the start of growth with R = 1.2 cm/h) is shown in Figure 4a,b. The microstructure at locations D1, E1, and F1 still contained hafnia, but the vol.% of the latter gradually decreased, and no hafnia was present at location G1, where the microstructure consisted of Nb_{ss}, and Nb_5Si_3 and Ti-rich Nb_5Si_3, the latter two silicides with Nb/(Ti + Hf) > 1.

Compared with locations D1, E1, and F1, hafnia was still present in the microstructure at locations D2, E2, and F2 but at a lower vol.%, and the same was the case at locations D3, E3, and F3 but the vol.% hafnia was further reduced, and no hafnia was present at locations D4, E4, and F4, where the microstructure consisted of Nb_{ss}, and Nb_5Si_3 and Ti-rich Nb_5Si_3 both with Nb/(Ti + Hf) > 1. In other words, in sections G1, G2, G3, and G4, no hafnia was observed in the microstructure.

The average chemical composition (at.%) of the areas contaminated with oxygen (sections from A1, B1, C1) was 24.1 ± 0.9Nb $- 20.6 \pm 0.8$Ti $- 10.0 \pm 0.9$Si $- 5.2 \pm 0.7$Al $- 8.5 \pm 1.1$Cr $- 2.0 \pm 0.4$Hf $- 6.0 \pm 0.7$Mo $- 0.7$W $- 2.9 \pm 0.3$Sn $- 2.9 \pm 0.6$Ge $- 17.1 \pm 2.3$O, which means that these areas also corresponded to an RCCA/RM(Nb)IC contaminated with oxygen. (Note that the Si concentration at the edge of the rod was low compared with the centre (bulk) of the rod; see Figure 3g).

The phases that were observed in the contaminated area were "normal" and Ti-rich Nb_5Si_3 with Nb/(Ti + Hf) ratios greater or less than 1 (see Table 2), $NbCr_2$ Laves phase, hafnia, "normal" and Ti-rich A15–Nb_3X (see Tables 2 and 3), Ti_{ss}, Nb- and Cr-rich silicide, and Ti-rich silicide (only few chemical analyses were possible for these silicides owing to their low vol.% in the microstructure) (Figure 4c,d), and occasionally "normal" and Ti-rich Nb_{ss} (Figure 4d). Of the aforementioned phases, owing to their chemical composition, the A15–Nb_3X, Nb_5Si_3, and Nb_{ss} were classified as complex concentrated (CC), the Nb- and Cr-rich silicide as high entropy (HE), whereas the $NbCr_2$, Ti_{ss}, and Ti-rich silicide were classified as "conventional". Note (i) that as the Ti concentration in the solid solution increased, the concentrations of Mo and W decreased and vice versa (see the data for the Nb_{ss} in Tables 2–4), in agreement with [9,13,44], and (ii) that in the centre (bulk) of the rod, Ti-rich Nb_5Si_3 with Nb/(Ti + Hf) < 1 was not observed (compare Table 4 with Table 2).

It should be noted that in the cast alloy (see [9]) the phases A2-Nb_{ss}, $D8_m$ βNb_5Si_3 (with Nb/(Ti + Hf) > 1, which is indicative of tetragonal silicide [71]), both "normal" and Ti-rich, and the C14-$NbCr_2$ Laves, Ti_{ss}, and hafnia were observed, and that in addition to these phases, the A15-Nb_3X, Nb_5Si_3 with Nb/(Ti + Hf) < 1 (which would suggest hexagonal silicide [71]), Nb- and Cr-rich silicide, and Ti-rich silicide were also observed in the areas contaminated with oxygen in the OFZ alloy. Furthermore, in the latter alloy, the Nb/(Ti + Hf) ratio of the "normal" Nb_5Si_3 silicide decreased from 2.4 near the edge to 1.7 in the centre (bulk) of the rod (compare data in Tables 2 and 4), whereas for the Ti-rich Nb_5Si_3 this ratio did not change (was 1.2). Moreover, it should be noticed that the A15-Nb_3X ("normal" and Ti-rich) was observed together with the silicide ("normal" and Ti-rich), Laves phase and hafnia in the cast alloys JZ4 and JZ5 [13] (see Appendix A for alloy chemical compositions). The formation of the Nb_5Si_3 with Nb/(Ti + Hf) < 1, Nb- and Cr-rich silicide, and Ti-rich silicide were attributed to contamination with oxygen and the synergy of the latter with macrosegregation. Furthermore, the <Cr> = Al + Cr + Ge + Si concentration of the Laves phase was in agreement with [72].

4.2. Growth Rate of 6 cm/h

The concentration profiles of each element from the edge of the rod towards its centre (bulk) of the rod (Figure 2b) are shown in Figure 5.

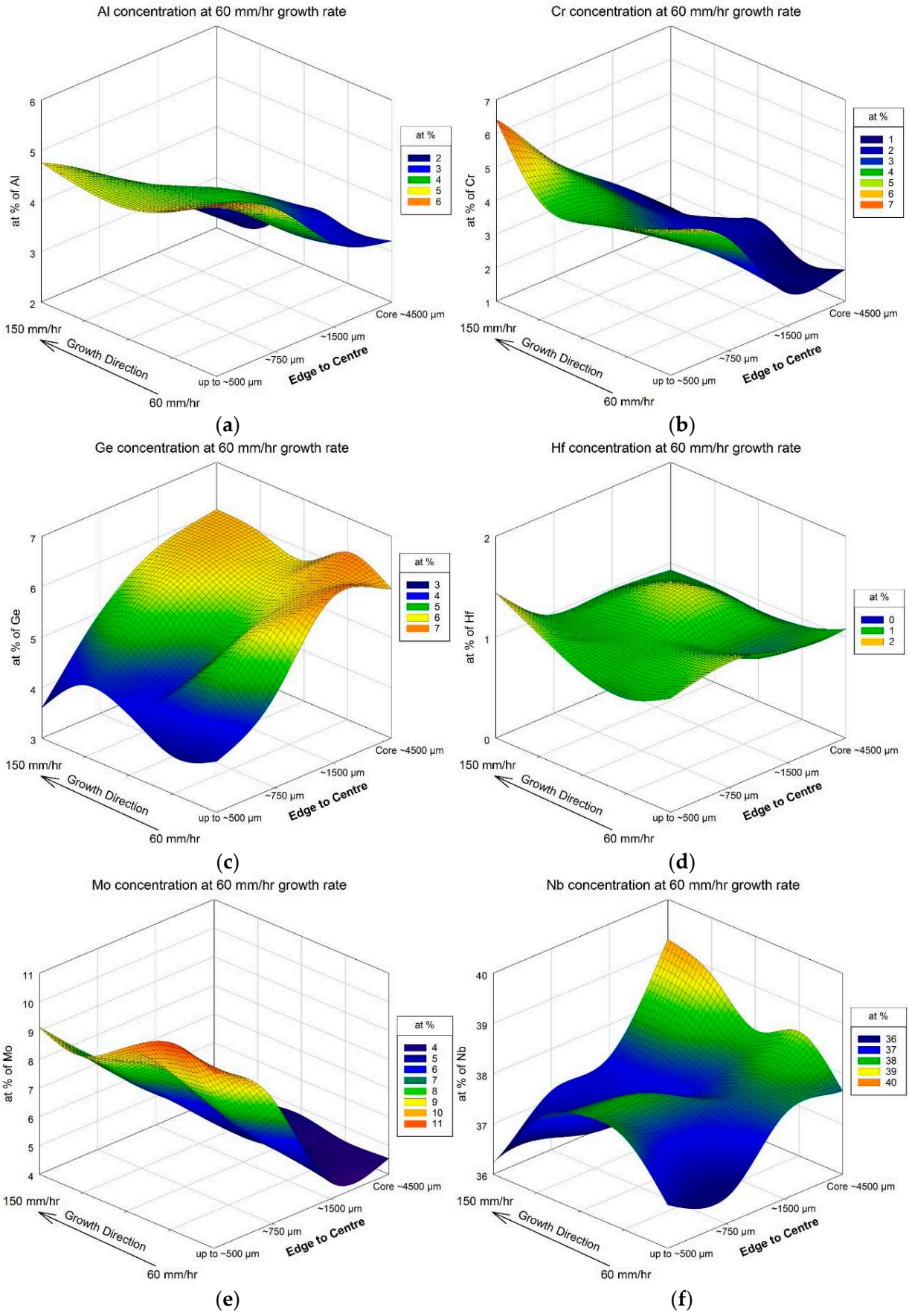

Figure 5. *Cont.*

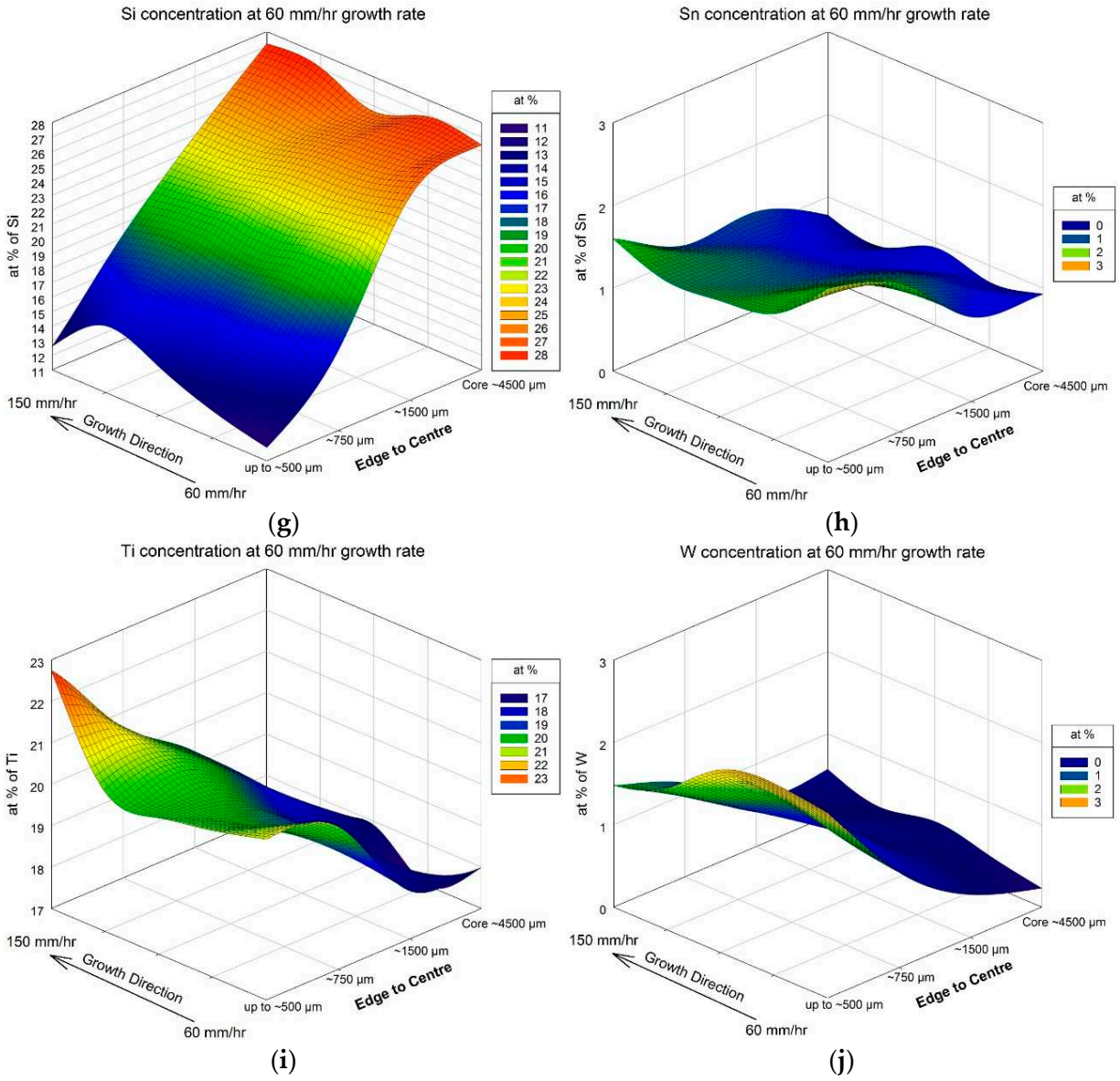

Figure 5. Concentration profiles of elements of the alloy NT1.2 that was directionally solidified using OFZ processing with growth rate of 6 cm/h: (**a**) Al, (**b**) Cr, (**c**) Ge, (**d**) Hf, (**e**) Mo, (**f**) Nb, (**g**) Si, (**h**) Sn, (**i**) Ti, and (**j**) W.

The concentrations of Al, Cr, Hf, Mo, Sn, Ti, and W were high near the edge of the rod, whereas those of Ge, Nb, and Si were low. The microstructure of the rod for this growth rate is shown in Figure 6.

No hafnia was observed in this part of the rod. There was still evidence of a transition from the edge towards the centre (bulk) of the rod, which became less distinct further away from the start of growth with R = 6 cm/h. For the microstructure of Figure 6b, the chemical composition of the Nb_{ss} near the edge was 36Nb–26Ti–2.9Si–4.6Al–13.9Cr–1.1Hf–11.9Mo–1W–2.3Sn–0.3Ge; further in, but still before the transition, it was 42.6Nb–21.5Ti–2.3Si–5Al–11Cr–0.7Hf–11.5Mo–2.6W–1.2Sn–1.7Ge; at the transition, it was 32.7Nb–18.8Ti–1.5Si–3.8Al–7.2Cr–0.5Hf–16.3Mo–3.6W–1.4Sn–0.7Ge; and away from the transition towards the centre (bulk) of the rod, it was 37.5Nb–21Ti–0.5Si–5Al–9.5Cr– 0.4Hf–18.1Mo–4.9W–1.9Sn–1.2Ge. In other words, at and near the edge, the Nb_{ss} was richer in Cr, Sn, and Ti compared with the Nb_{ss} in the centre (bulk), and in the centre (bulk), the Nb_{ss} was poor in Si, and richer in Mo and W compared with the Nb_{ss} near the edge. The concentrations of Mo and W in the

Nb_{ss} increased significantly at the transition and then increased further in the centre (bulk) of the rod. It should be noted that the Nb/(Ti + Hf) ratio of some of the Ti-rich Nb_5Si_3 was very close to 1 and that no Ti-rich Nb_5Si_3 was observed before the transition.

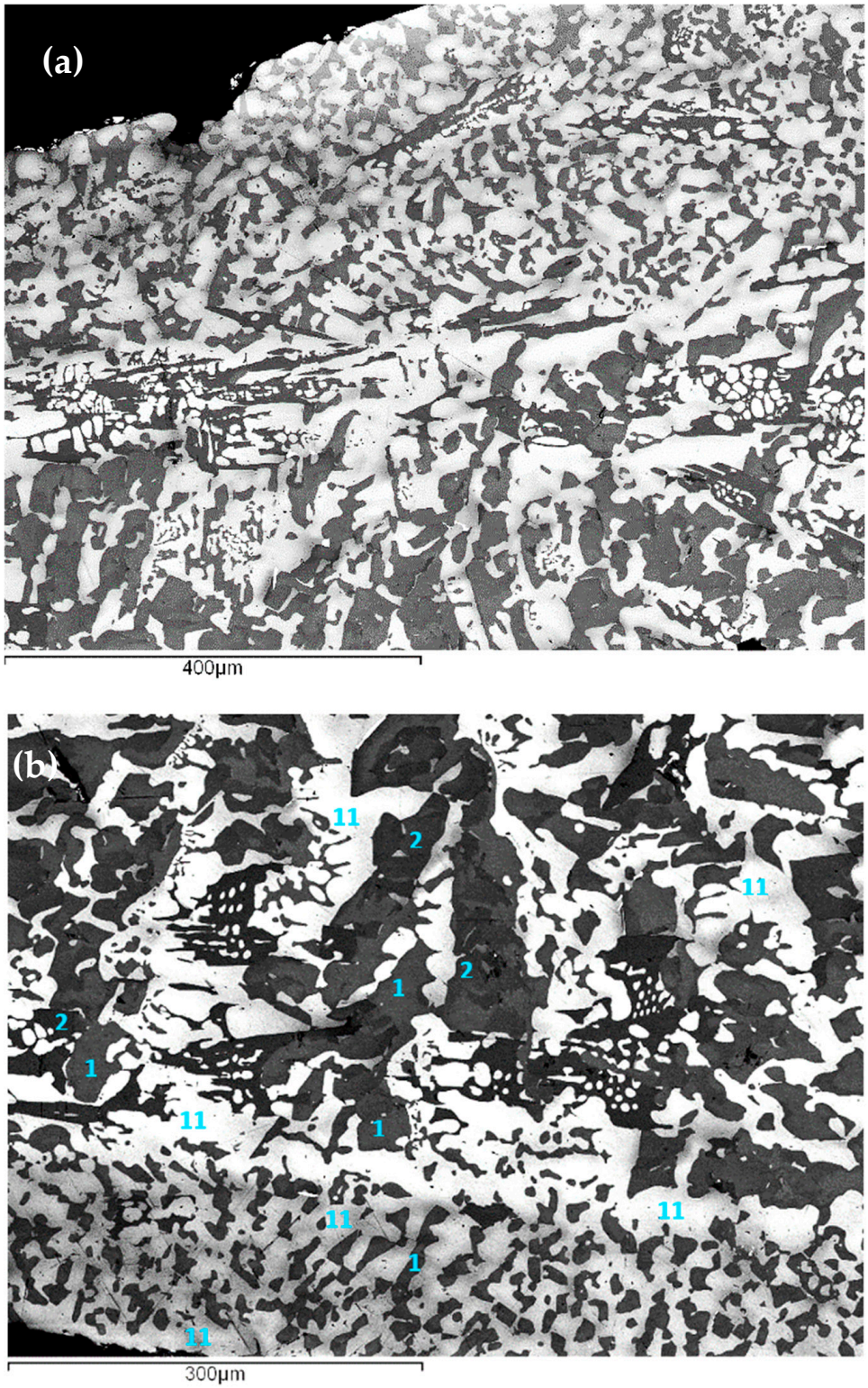

Figure 6. *Cont.*

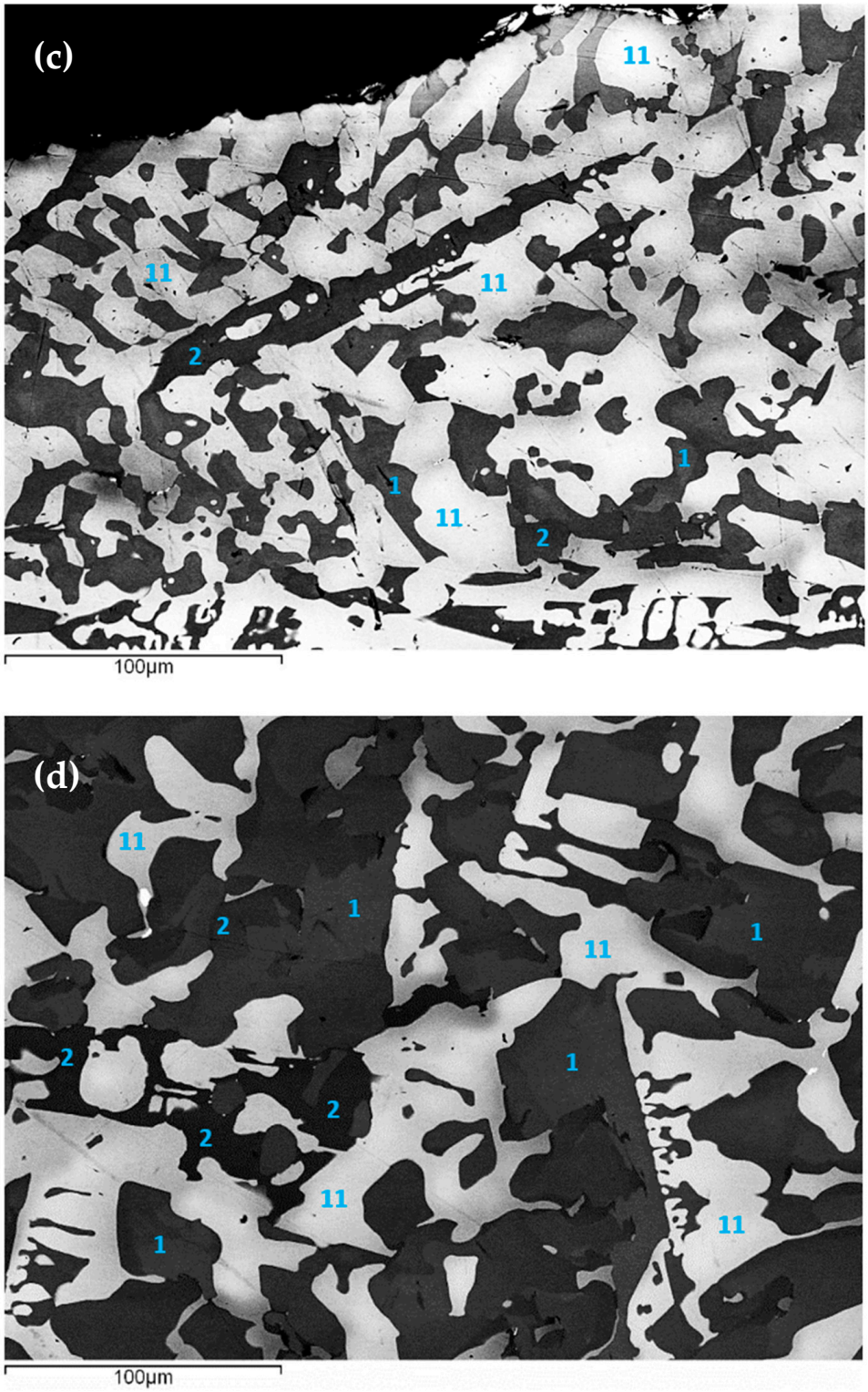

Figure 6. Back-scatter electron (BSE) images of the alloy NT1.2 that was directionally solidified using OFZ processing with growth rate of R = 6 cm/h (following on from R = 1.2 cm/h): (**a**,**b**) show edge microstructures at the start of growth with R = 6 cm/h and transition, (**a**) shows the microstructure slightly further away from (**b**), and (**c**) slightly further away of (**a**), and (**d**) shows the microstructure in the centre (bulk) of the rod. Phases are identified with numbers as follows: 1 = silicide and 2 = Ti-rich silicide with Nb/(Ti + Hf) > 1, 11 = Nb_{ss}. For the chemical composition of phases in (**a**,**c**), and the centre (bulk) of the rod, see text and Tables 5–7, respectively.

Table 5. Chemical composition (at.%) of phases in Figure 6b.

Phase	Nb	Ti	Si	Al	Cr	Hf	Mo	W	Sn	Ge
Nb_{ss}	40.4 ± 2.3	22.5 ± 2.4	1.9 ± 1	4.6 ± 0.6	11.1 ± 2.2	0.8	13.2 ± 3	2.6 ± 1.4	1.9 ± 0.6	1 ± 0.6
Ti-rich Nb_5Si_3 Nb/(Ti + Hf) > 1	30.1 ± 0.4	26 ± 0.2	27.3 ± 0.3	3.2 ± 0.2	1.7 ± 0.1	2.8 ± 0.1	1.9 ± 0.2	-	-	7.1 ± 0.1
Nb_5Si_3	38.8 ± 1	19.2 ± 1.2	27 ± 1	3.1 ± 0.5	1.6 ± 0.3	1.3 ± 0.1	2.3 ± 0.3	-	-	6.7 ± 0.2

Table 6. Chemical composition (at.%) of phases in Figure 6c.

Phase	Nb	Ti	Si	Al	Cr	Hf	Mo	W	Sn	Ge
Nb_{ss}	38.3 ± 3.7	25.2 ± 2.4	3.4 ± 1.3	4.8 ± 0.6	12.6 ± 1.8	1 ± 0.5	9.7 ± 0.8	1.6 ± 0.4	2.4 ± 0.4	1
Ti-rich Nb_5Si_3 Nb/(Ti + Hf) > 1	29.7 ± 0.5	24.4 ± 0.4	24.9 ± 0.5	7.1 ± 0.3	1.4 ± 0.3	3.4 ± 0.2	-	-	-	9.1 ± 0.3
Nb_5Si_3	34.3 ± 0.9	21.3 ± 1	24.6 ± 1.2	7.2 ± 0.4	2 ± 0.5	1.8 ± 0.3	-	-	1	7.8 ± 0.4

Table 7. Chemical composition (at.%) of phases in the centre (bulk) of the rod (typical microstructure is shown in Figure 6d).

Phase	Nb	Ti	Si	Al	Cr	Hf	Mo	W	Sn	Ge
Nb_{ss}	44.9 ± 0.9	18.6 ± 2	1 ± 0.3	4.4 ± 0.5	7.6 ± 1.4	-	18.3 ± 1.7	5.1 ± 1.3	-	-
Ti-rich Nb_5Si_3	29.5 ± 0.4	26.1 ± 0.3	27.5 ± 0.6	3.4 ± 0.4	1.6 ± 0.4	3 ± 0.2	1.7 ± 0.3	-	-	7.2 ± 0.6
Nb_5Si_3	37.9 ± 0.6	19.5 ± 0.4	26.9 ± 0.5	3 ± 0.5	1.7 ± 0.3	1.3 ± 0.3	3.2 ± 0.4	-	-	6.5 ± 0.5

For the microstructure of Figure 6a, the chemical composition (at.%) of the Nb_{ss} near the edge was 43.2Nb–23.6Ti–4.3Si–4.3Al–10.9Cr–1.4Hf–8.6Mo–0.8W–1.6Sn–1.3Ge; further in, but before the transition, it was 34.9Nb–27.8Ti–3.7Si–4.9Al–14.8Cr–1.8Hf–9.1Mo–0W–3Sn–0.2Ge; at the transition, it was 39.7Nb–24.1Ti–2.5Si–5Al–12.3Cr–0.3Hf–10.6Mo–1.5W–2.5Sn–1.5Ge; and away from the transition towards the centre (bulk) of the rod. it was 42.4Nb–23.1Ti–1.8Si–5.5Al–10.1Cr–0.9Hf–10.4Mo–2.1W –2Sn–1.8Ge. In other words, compared with the Nb_{ss} in areas before the transition, the Nb_{ss} in the centre (bulk) was poorer in Si and richer in Cr, Mo, and W, but compared with the Nb_{ss} in Figure 6b, in the centre (bulk) it was richer in Si and poorer in Mo and W. For Figure 6a, at the transition, the composition of the Nb_5Si_3 was 35Nb–20.5Ti–25.5Si–6.9Al–1.9Cr–1.9Hf–0Mo–0W–0.6Sn–7.4Ge and that of Ti-rich Nb_5Si_3 was 28.9Nb–24Ti–25.2Si–6.8Al–1.1Cr–3.6Hf–0Mo–0W–0.7Sn–8.5Ge. In the transition and away from it towards the centre (bulk), both Nb_5Si_3 and Ti-rich Nb_5Si_3 were formed, both with Nb/(Ti + Hf) > 1, but for some Ti-rich silicide grains in the transition the said ratio was very close to 1.

In the centre (bulk) of the rod, the phases were Nb_{ss}, Nb_5Si_3 with Nb/(Ti + Hf) > 1 (and higher than the ratio for the silicide in the transition or towards the centre (bulk), meaning the ratio increased as we moved from the edge to the centre), and Ti-rich Nb_5Si_3 with Nb/(Ti + Hf) ratio very close to one (0.97 to 1.03) (meaning for the Ti-rich silicide the ratio did not change from the edge to the centre (bulk) of the rod). The chemical compositions of the phases are given in Table 7. For the Nb_{ss}, note that some grains contained as much as 21 Ti, 9.5 Cr, 20.4 Mo, and 6.8 W (at.%). As always, as the concentration of Mo and W increased in the Nb_{ss}, that of Ti decreased, in agreement with the data for R = 1.2 cm/h and [9,13,44], and also as the concentration of Ti in the Nb_{ss} increased, so did that of Cr, in agreement with [73].

Compared with solidification with R = 1.2 cm/h, no A15-Nb_3X, C14 $NbCr_2$ Laves, Ti_{ss}, Nb- and Cr-rich silicide, or Ti-rich silicide formed with R = 6 cm/h. Compared with the cast alloy [9], the C14 $NbCr_2$ Laves and Ti_{ss} were absent in the microstructure grown with R = 6 cm/h. The compositions of the Nb_{ss} and Nb_5Si_3 corresponded to CC phases with the

exception of the Nb_{ss} in the centre (bulk) of the rod (Tables 5–7). Note that the latter solid solution was poorer in Ti, Si, Cr, Sn, and Ge and richer in Mo, Nb, and W compared with the Nb_{ss} near the edge of the rod. Also, note the change in the concentration of Al and Mo in Nb_5Si_3 in different locations in the rod.

4.3. Growth Rate of 15 cm/h

A transition existed from the edge to the centre (bulk) of the bar, see Figure 7a. This transition was less well-defined compared with the two lower growth rates. In the centre (bulk), the microstructure consisted of two phases, namely the Nb_{ss} (indicated as ss in Figure 7b) and the Nb_5Si_3 silicide, see Figure 7b,c. No A15-Nb_3X was formed, similar to the directional solidification with R = 6 cm/h. The solid solution exhibited bright contrast and consisted of an even brighter contrast core (indicated as ss1 in Figure 7c) compared with the edges (indicated as ss2 in Figure 7c). The silicide also exhibited two contrasts, one grey and the other dark (Ti-rich Nb_5Si_3 in Figure 7c). The average chemical compositions of the said phases are given in Table 8. Note that Figure 7d shows the microstructure just before the start of the termination (see next section). In the centre (bulk), the faceting of Nb_5Si_3 was strong (Figure 7d). Such faceting was observed in the cast alloy [9] and in the RM(Nb)ICs alloys ZF6-AC [74], EZ2-AC [34], and EZ6-HT [34] (see Appendix A for alloy compositions). Also note that faceting was not observed in the microstructures grown with growth rates of 1.2 cm/h and 6 cm/h. No hafnia was observed in this part of the rod.

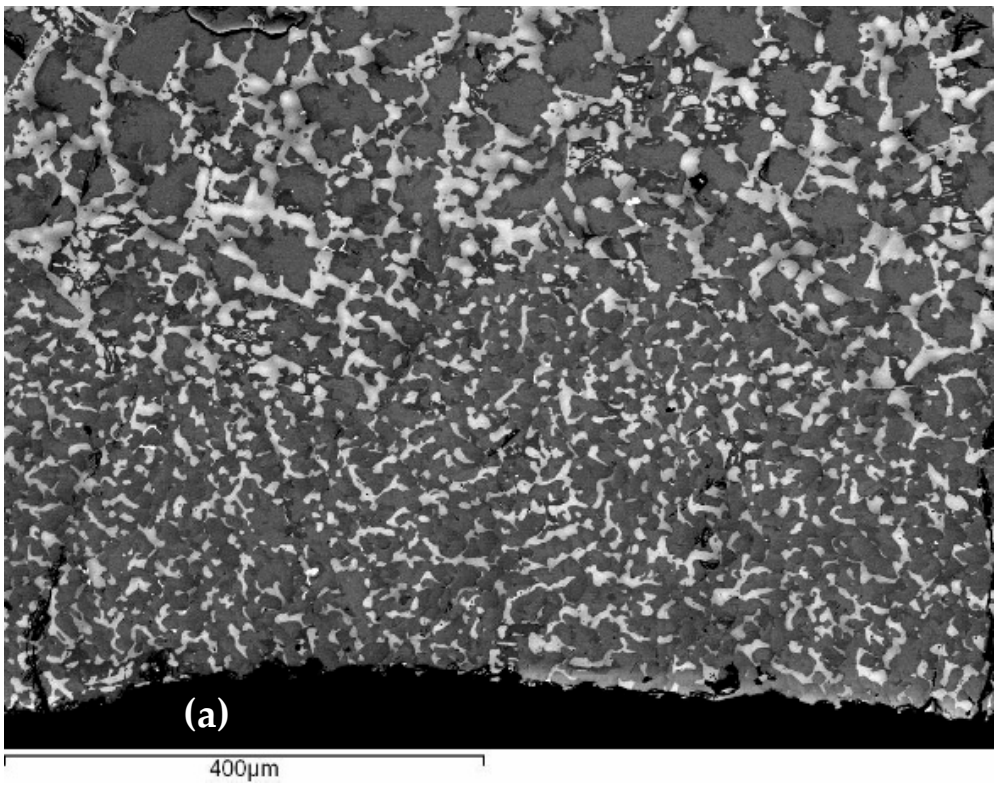

Figure 7. *Cont.*

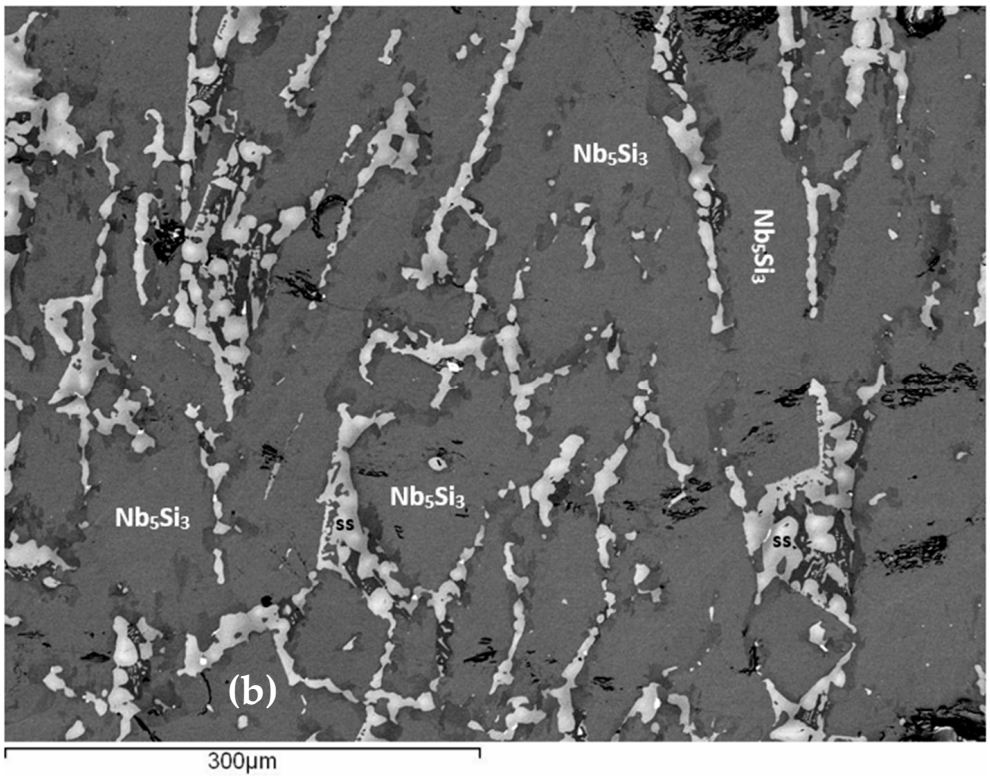

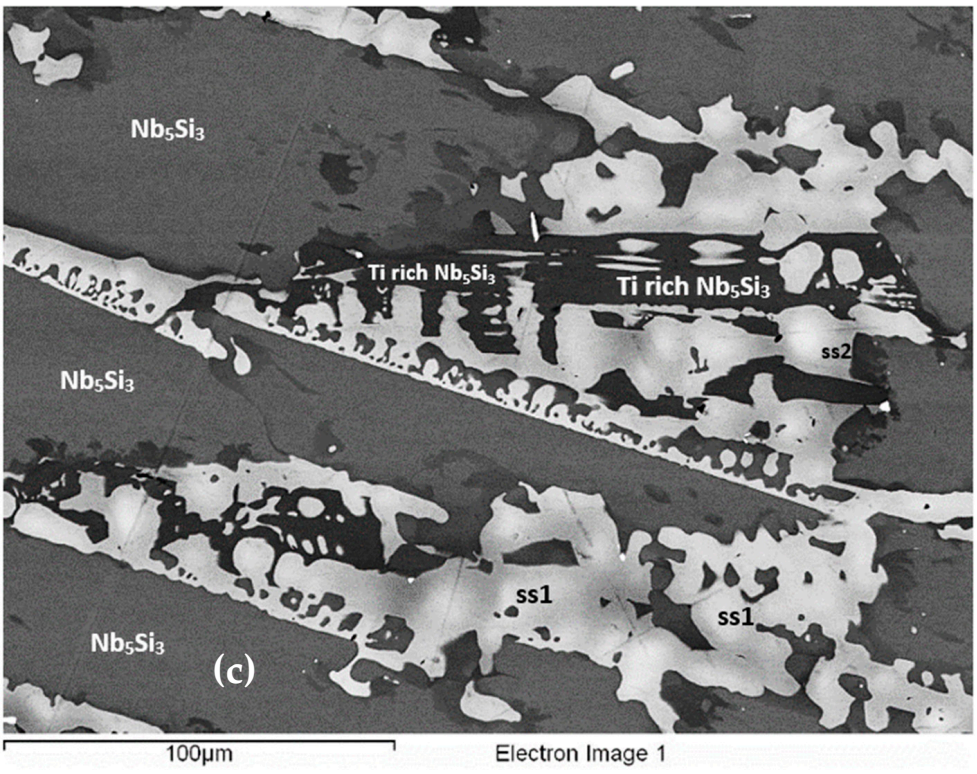

Figure 7. *Cont.*

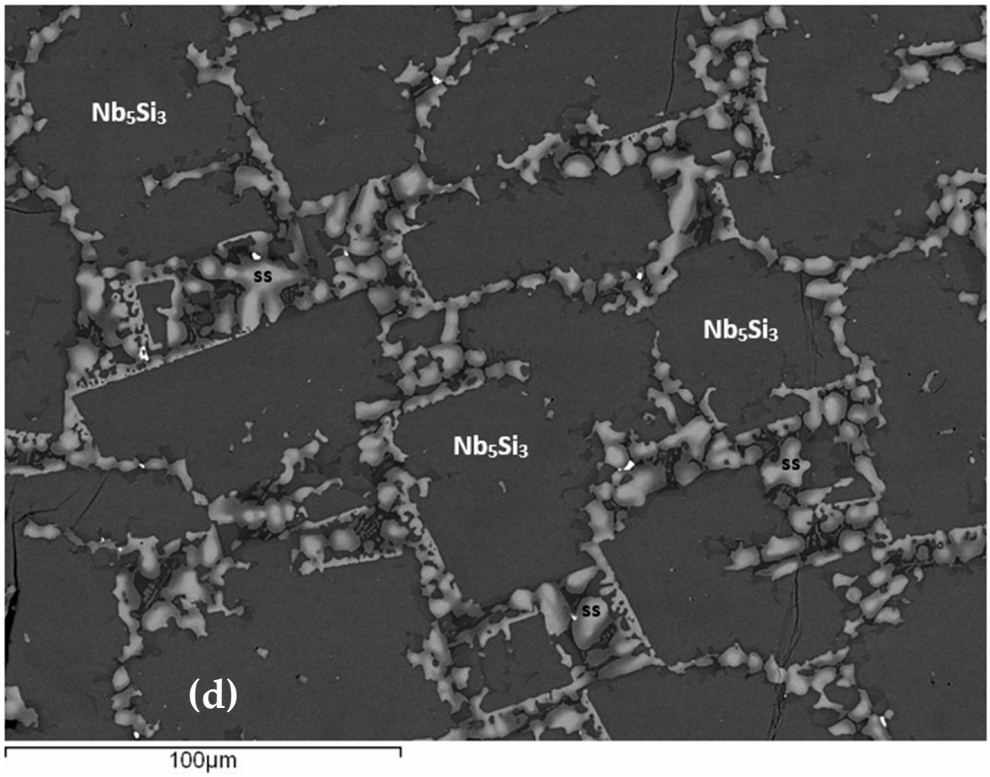

Figure 7. BSE images of the RCCA/RM(Nb)IC alloy NT1.2 that was directionaly solidified using OFZ procesing with growth rate R = 15 cm/h: (**a**) shows microstructure at the edge of the rod, and (**b**), (**c**,**d**) show mictostructure in the centre (bulk) of the rod. Note that (**d**) shows the microstructure very close to the start of the termination.

Table 8. Chemical composition (at.%) of phases in the centre (bulk) of the rod grown with R = 15 cm/h.

Phase	Nb	Ti	Si	Al	Cr	Hf	Mo	W	Sn	Ge
Nbss core (ss1)	44.9 ± 1.2	18.6 ± 1.6	0.6	3.9 ± 0.3	5.6 ± 1	-	19.3 ± 0.9	5 ± 1	1.1 ± 0.2	1
Ti-rich Nbss (ss2)	36.6 ± 1.6	27 ± 1.4	0.8	5.8 ± 0.1	12 ± 1.3	-	12.8 ± 1.2	1.6 ± 0.2	2.4 ± 0.2	1
Ti-rich Nb5Si3 Nb/(Ti + Hf) < 1	24.4 ± 0.9	31.6 ± 0.8	26.2 ± 0.1	3.4 ± 0.1	1.9 ± 0.2	3.3 ± 0.1	1.6 ± 0.1	-	-	7.6 ± 0.2
Nb5Si3	38.6 ± 1.8	19.2 ± 1.9	26.9 ± 1.4	2.4 ± 0.7	1.2 ± 0.3	1.1 ± 0.2	3.8 ± 0.4	-	-	6.8 ± 0.4

The chemical composition of the Nb_{ss} and Nb_5Si_3 in the centre (bulk) of the rod was very close to that in the bulk of the rod grown with R = 6 cm/h (compare Tables 7 and 8). There was less segregation of Si from the edge to the centre (bulk) of the rod when compared with the lower growth rates, but the average Si concentration was higher (see Table 1a and Figure 8). Furthermore, there was no significant segregation of other alloying elements from the edge to the bulk, for example, see the Al, Cr, and Sn solute profiles in Figure 8.

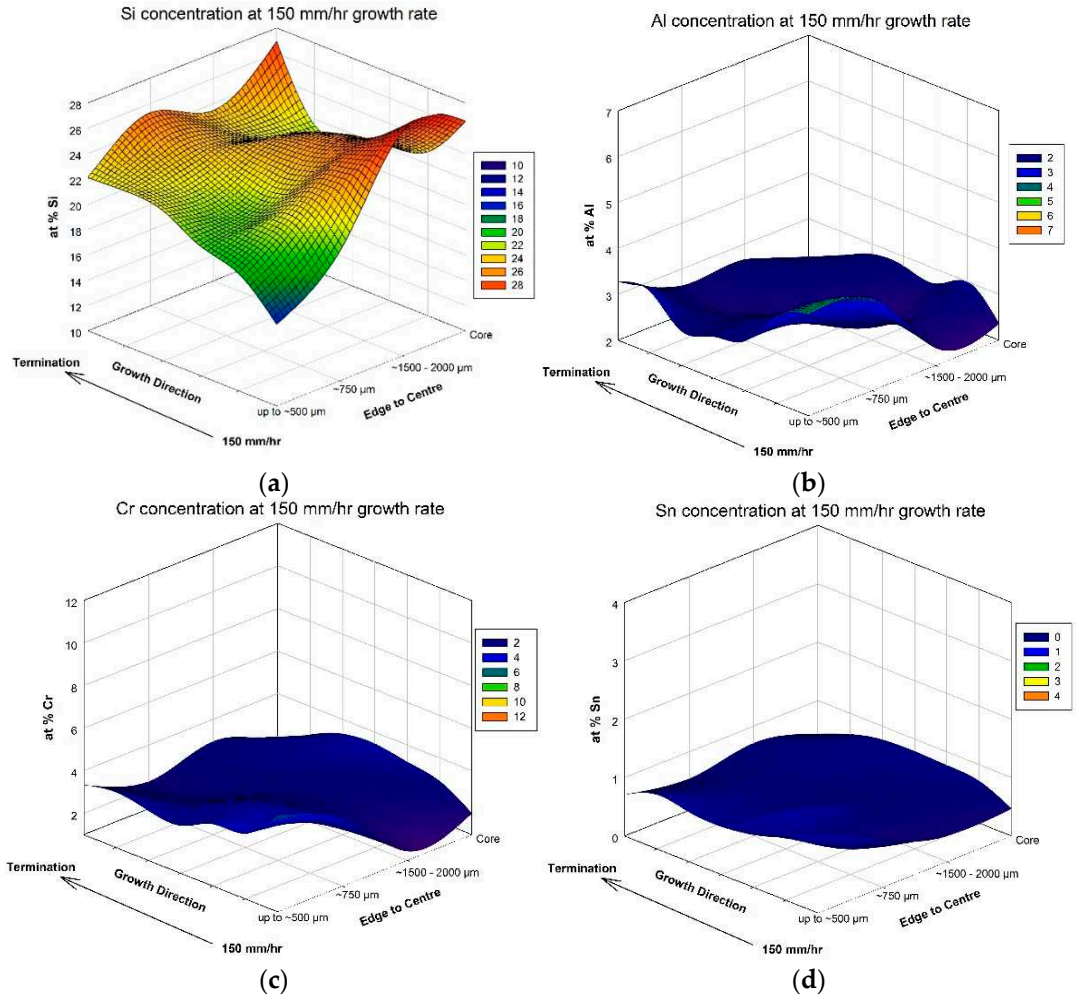

Figure 8. Concentration profiles of elelemnts of the RCCA/RM(Nb)IC alloy NT1.2 that was directionally solidified using OFZ processing with growth rate R = 15 cm/h: (**a**) Si, (**b**) Al, (**c**) Cr, and (**d**) Sn.

4.4. Termination

The microstructure of the termination is shown in Figure 9. There was no transition from the edge to the bulk of the bar, but faceting of the Nb_5Si_3 similar to that shown in Figure 7d was observed. Figure 9c shows the phases that were observed in the highlighted microstructures in Figure 9b. In the bulk, the microstructure consisted of Nb_{ss}, Nb_5Si_3 silicide, the C14-$NbCr_2$ Laves phase, and a very low vol.% of hafnia (Figure 9c). No A15-Nb_3X was observed. There was Ti-rich Nb_{ss} (indicated as Nb_{ss} Ti-rich (ss1) in Table 9) and Ti-rich Nb_5Si_3 with Nb/(Ti + Hf) ratios less or greater than one (Table 9). With the exception of the core of the Nb_{ss}, which is indicated as Nb_{ss} (ss) in Table 9, the chemical compositions of the other phases corresponded to complex concentrated (CC) phases.

The chemical composition of the Nb_{ss} and Ti-rich Nb_{ss}, and Nb_5Si_3 with Nb/(Ti + Hf) <1 was very close to that in the bulk of the bar grown with R = 15 cm/h. Compared with the data for the latter growth rate, the Nb_5Si_3 silicide had Nb/(Ti + Hf) ratio less or greater than one (compare Tables 8 and 9). The chemical composition of the Laves phase was similar to that observed for growth with R = 1.2 cm/h and the cast alloy [9], and in agreement with [72].

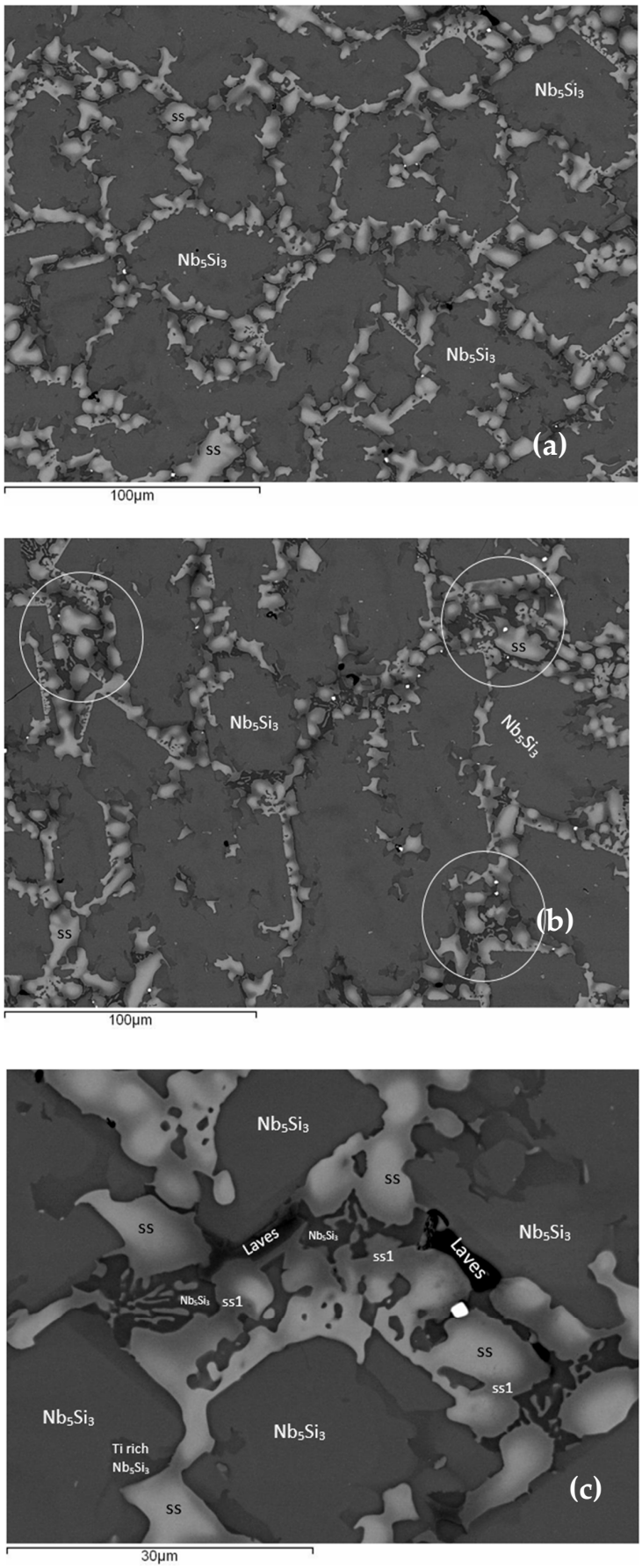

Figure 9. *Cont.*

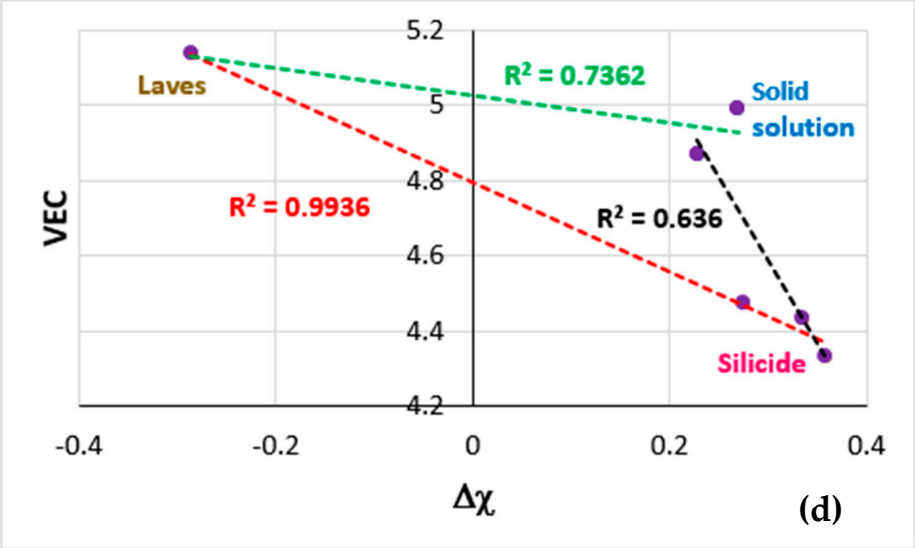

Figure 9. (**a**–**c**) BSE images of the microstructure of the termination and (**d**) VEC versus Δχ map of the phases in the termination: (**a**,**b**) show the bulk microstructure and (**c**) shows details of microstructures that are highlighted with circles in (**b**). The white contrast phase in (**c**) is hafnia. In (**d**), R^2 = 0.9936 for the Laves phase and the silicide, R^2 = 0.7362 for the Laves phase and the solid solution, and R^2 = 0.636 for the solid solution and the silicide.

Table 9. Chemical composition (at.%) of phases in the bulk of the termination.

Phase	Nb	Ti	Si	Al	Cr	Hf	Mo	W	Sn	Ge
Nb_{ss} (ss)	45.1 ± 0.9	17.7 ± 1.2	1.3 ± 0.6	4.4 ± 0.5	4.9 ± 0.8	-	19.2 ± 0.7	5.2 ± 1.1	1 ± 0.2	1.2 ± 0.3
Nb_{ss} Ti-rich (ss1)	37.3 ± 1.3	25.4 ± 1.1	0.9	5.5 ± 0.2	12.7 ± 1	-	12.9 ± 1.1	2.1 ± 0.4	2.2 ± 0.1	1 ± 0.2
Ti-rich Nb_5Si_3 Nb/(Ti + Hf) < 1	24.8 ± 0.8	30.1 ± 0.7	23.6 ± 0.3	3.8 ± 0.2	3.7 ± 0.5	3.7 ± 0.3	2.5 ± 0.2	-	1 ± 0.2	6.8 ± 0.2
Ti-rich Nb_5Si_3 Nb/(Ti + Hf) > 1	36.4 ± 0.9	20.9 ± 0.5	26.1 ± 0.2	3.3 ± 0.3	1.7 ± 0.3	1.3 ± 0.2	3.4 ± 0.2	-	-	6.9 ± 0.2
Nb_5Si_3	39.3 ± 1.5	16.6 ± 1.2	29.1 ± 1.1	1.9 ± 0.6	1	1 ± 0.3	4 ± 0.5	-	1	6.1 ± 0.4
NbC_2 Laves	22.3 ± 0.6	15.6 ± 0.7	9 ± 0.3	3.2 ± 0.2	43.4 ± 0.5	2.4 ± 0.2	2.9 ± 0.3	-	0.5	1.2 ± 0.3

The VEC versus Δχ map of the phases in the bulk of the termination, which is presented in Figure 9d shows (a) that the shape of the "territory" of the termination is similar to that of the alloy NT1.2 (see Figure 29c in [9]) and (b) that there were correlations between the phases in this part of the OFZ bar.

4.5. Change in the Parameters VEC, Δχ, and δ with Location in the OFZ Bar

The macrosegregation of solutes as indicated with the concentration profiles of elements between the edge and centre (bulk) of the bar, as shown for example in Figure 3, is attributed to multicomponent thermosolutal convective instability in the molten zone (Figure 1) and to thermocapillary flow of solutes during OFZ. The latter was discussed in [44], where it was shown that it can introduce considerable inhomogeneities even under gentle flow and can explain the chemical inhomogeneity between the edge and the centre (bulk) of the OFZ bar grown at the three different growth rates. The interested reader could refer to [44], where formation of cracks during OFZ processing was also discussed.

The concentration profiles of the solutes changed as the growth rate increased, and at the highest growth rate, it was still noted for Si but not for the other elements. For example,

see Figure 10, which shows the solutes profiles of four elements, namely Si, Al, Cr, and Sn, that are key solutes regarding oxidation behaviour, creep strength, and toughness [3,4,10].

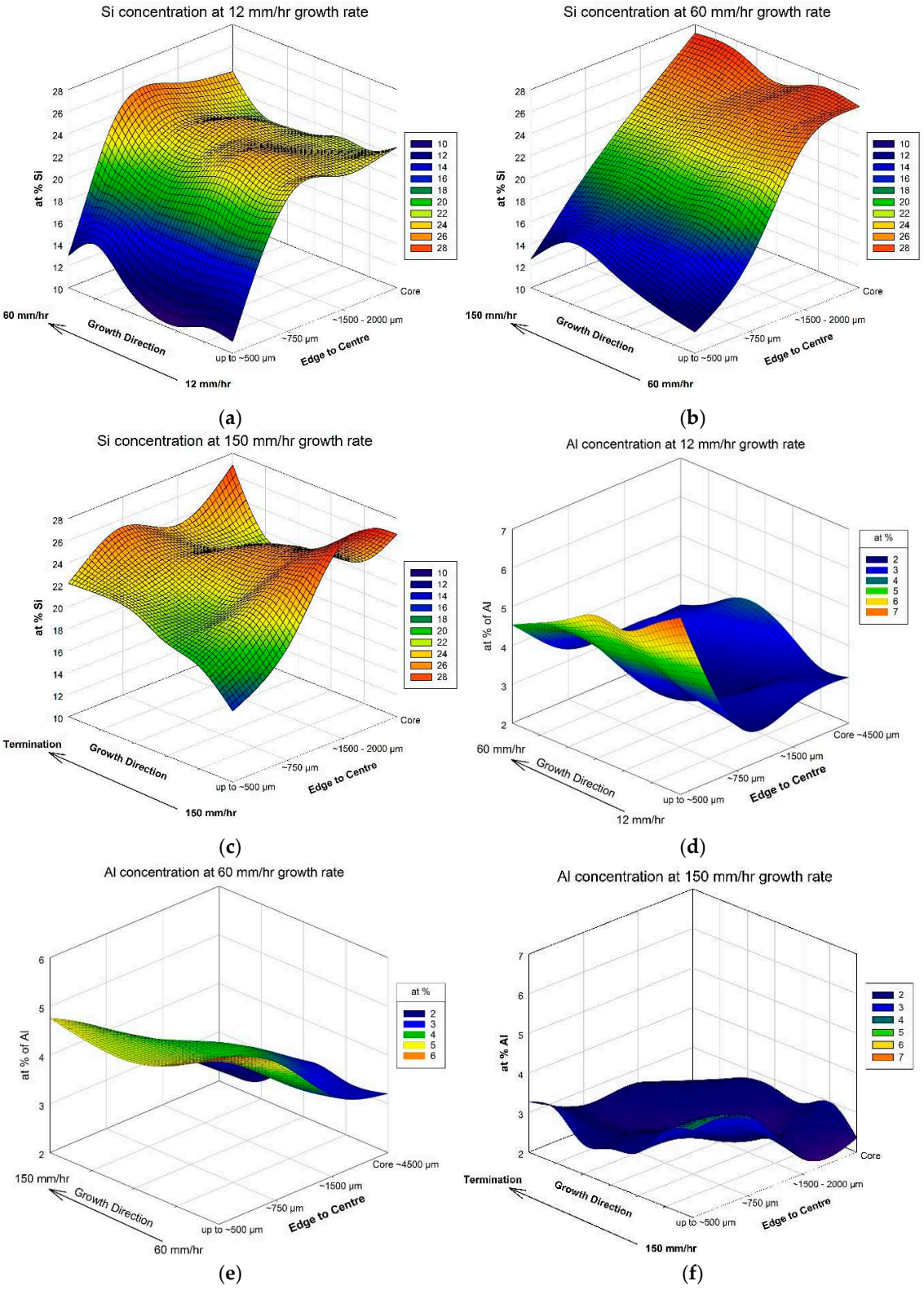

Figure 10. *Cont.*

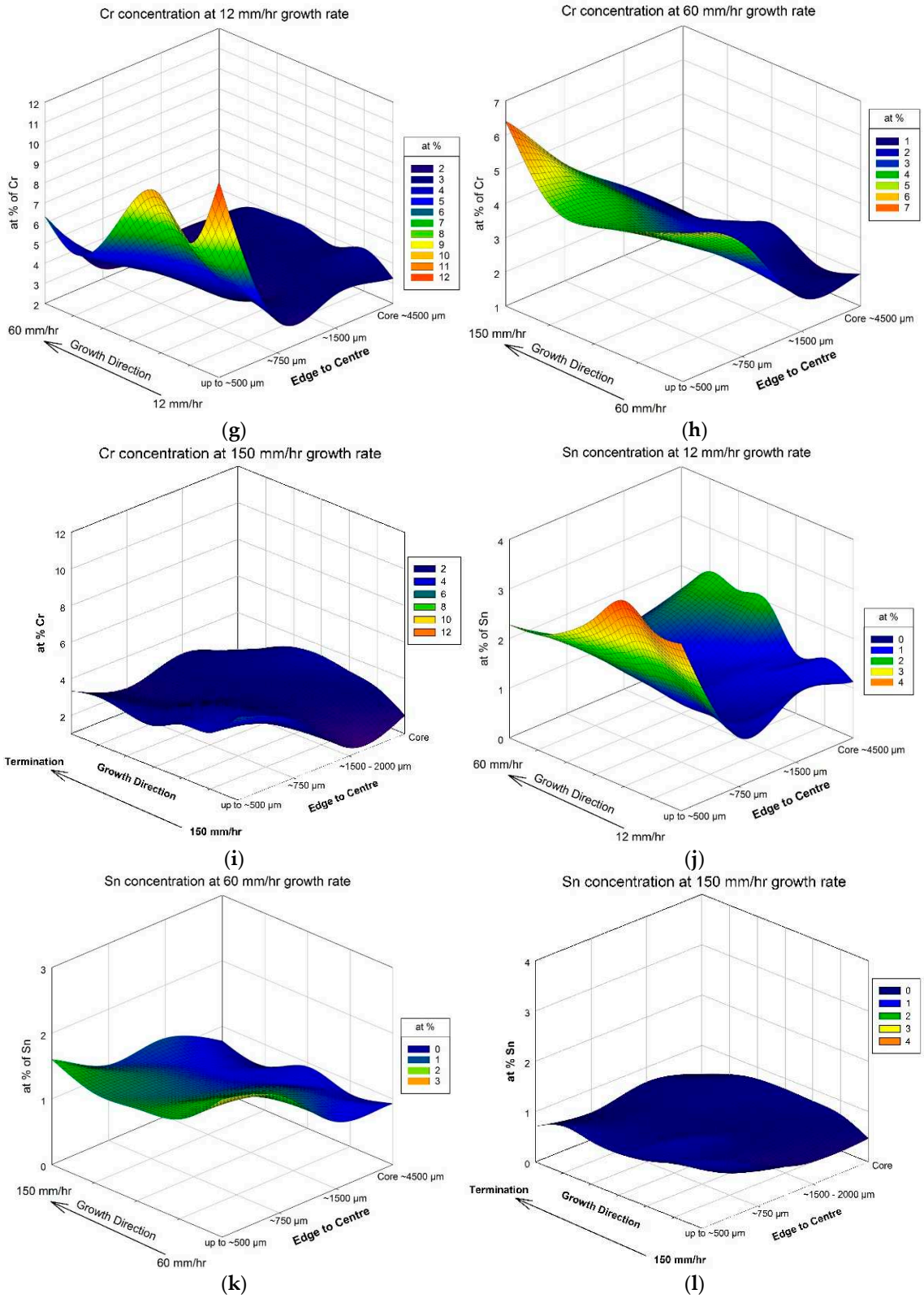

Figure 10. Concentration profiles of Si, Al, Cr, and Sn of the RCCA/RM(Nb)IC alloy NT1.2 that was directionally solidified using OFZ processing. (**a**,**d**,**g**,**j**) R = 1.2 cm/h, (**b**,**e**,**h**,**k**) R = 6 cm/h, and (**c**,**f**,**i**,**l**) R = 15 cm/h.

Properties of metallic UHTMs are related to their parameters VEC, $\Delta\chi$, and δ [1,4,10]. The relationships are used in the alloy design methodology NICE [10,75] to design and develop metallic UHTMs and UHTM systems [1,5]. We used the macrosegregation data

for each growth rate, i.e., the concentration profiles between the edge and the centre (bulk) of the OFZ bar, to calculate the said parameters (see Appendix A in [75]) for each location (Figure 2b) and each growth rate, and to show how they changed, correlations between them, between the parameters and solutes, and between solutes. Below and in the Supplemental Materials we report correlations for which $R^2 > 0.7$.

Figure 11 first shows the change in the parameter VEC with all locations A1 to G4 for R = 1.2 cm/h (Figure 11a), and A1 to E4 for R = 6 cm/h (Figure 11b) and R = 15 cm/h (Figure 11c), and then for locations A_i–B_i–C_i–D_i–E_i–F_i–G_i (i = 1, 2, 3, 4) for R = 1.2 cm/h (Figure 11d–g), and for the locations A_i–B_i–C_i–D_i–E_i (i = 1,2,3,4) for R = 6 cm/h (Figure 11h–k) and R = 15 cm/h (Figure 11l–o).

Figure 12 first shows the change in the parameter $\Delta\chi$ with all locations A1 to G4 for R = 1.2 cm/h (Figure 12a), and A1 to E4 for R = 6 cm/h (Figure 12b) and R = 15 cm/h (Figure 12c), and then for locations A_i–B_i–C_i–D_i–E_i–F_i–G_i (i = 1,2,3,4) for R = 1.2 cm/h (Figure 12d–g), and for the locations A_i–B_i–C_i–D_i–E_i (i = 1,2,3,4) for R = 6 cm/h (Figure 12h–k) and R = 15 cm/h (Figure 12l–o).

Figure 13 first shows the change in the parameter δ with all locations A1 to G4 for R = 1.2 cm/h (Figure 13a), and A1 to E4 for R = 6 cm/h (Figure 13b) and R = 15 cm/h (Figure 13c), and then for locations A_i–B_i–C_i–D_i–E_i–F_i–G_i (i = 1,2,3,4) for R = 1.2 cm/h (Figure 13d–g), and for the locations A_i–B_i–C_i–D_i–E_i (i = 1,2,3,4) for R = 6 cm/h (Figure 13h–k) and R = 15 cm/h (Figure 13l–o).

Similar or opposite trends of parameters were observed for certain location sequences and growth rates; for example, for the parameters VEC, $\Delta\chi$, and δ see Figures 11l, 12l and 13l, and Figures 11n, 12n and 13n, for the parameter $\Delta\chi$ see Figure 12d,h, and for the parameters $\Delta\chi$ and δ see Figures 12f and 13f, and Figures 12o and 13o.

Figures 14 and 15 compare the data for the parameters VEC, $\Delta\chi$, and δ for the three growth rates for the location sequence A1–A2–A3–A4–B1–B2–B3–B4–C1–C2–C3–C4–D1–D2–D3–D4–E1–E2–E3–E4. The change in $<\chi>$ and <r> for the same location sequence is shown in Figure 14 ($<x> = \Sigma c_i\chi_I$ and $<r> = \Sigma c_i r_i$ where c_i, χ_I, and r_i are, respectively, the concentration (at.%), Pauling electronegativity, and atomic radius of element i). Note (1) similar trends for VEC and $\Delta\chi$ for the growth rates of 1.2 and 6 cm/h (Figure 14a,g, and Figure 14b,h) that are opposite to the trends of the parameter δ for the same growth rates (compare with Figure 14m,n), (2) the change in the parameters VEC, $\Delta\chi$, and δ from location D1 towards E4 for the growth rate of 15 cm/h (compare Figure 13c with Figures 13i and 13o), (3) that $\Delta\chi$ and δ in (2) link with the changes in $<\chi>$ and <r> (see Figure 14f,l, and compare Figure 14f,i and Figure 14l,o), (4) the reduced variability of the parameters for the growth rate of 15 cm/h (see Figure 15g–i, and compare with Figure 15d–f), (5) that the parameters VEC and $\Delta\chi$ exhibited maxima at locations A1, B1, C1, D1, and E1 (Figure 15a,d,g, and Figure 15b,e,h) at which the parameter δ exhibited minima (for example, see Figure 15f and compare with Figure 15d,e).

The macrosegregation data showed that for the location sequence A1–A2–A3–A4–B1–B2–B3–B4–C1–C2–C3–C4–D1–D2–D3–D4–E1–E2–E3–E4 there were good correlations between the parameters VEC, $\Delta\chi$, and δ for the three growth rates (Figure 16), in particular for R = 6 cm/h (Figure 16b,e,h). The parameter values were within the ranges reported for RCCAs/RM(Nb)ICs, RHEAs/RM(Nb)ICs, and RM(Nb)ICs, see Table 1 in [75]. The parameter VEC increased with increasing $\Delta\chi$ (Figure 16a–c) and decreased with increasing δ (Figure 16d–f). The parameter $\Delta\chi$ decreased with increasing δ (Figure 16g–i). Note that similar correlations between VEC and $\Delta\chi$ have been reported in [13] for the data of the alloys OHS1, JZ3, JZ3+, JG6, EZ8, ZF9, JZ4, and JZ5 (see Appendix A for alloy compositions).

4.6. Relationships Between Parameters and Solutes Along the Thickness of the OFZ Bar

There were correlations between the parameters VEC, $\Delta\chi$, and δ and the solute elements for all sections along the thickness of the bar, see Figures 17–19 and the Supplemental Material. The said figures give data for the section A1–A2–A3–A4 for the three parameters and the solutes Si, Ti, Mo, and Cr for R = 1.2 cm/h (Figure 17), R = 6 cm/h (Figure 18), and R = 15 cm/h (Figure 19). For the other sections and solutes see the Supplemental Material. Note that for R = 1.2 cm/h the correlations along the said section and solutes for the parameter $\Delta\chi$ were poor (i.e., $R^2 < 0.7$), and that correlations with $R^2 > 0.7$ were found from section B1–B2–B3–B4. Also note opposite trends for the relationships of the parameters $\Delta\chi$ and δ and VEC and δ for the solutes, and similar trends of the parameters VEC and $\Delta\chi$ for all three growth rates.

4.7. Relationships Between Parameters and Solutes Along the Length of the OFZ Bar

There were correlations between the parameters VEC, $\Delta\chi$, and δ and the solutes Al, Cr, Ge, Hf, Mo, Nb, Si, Ti, and W along the length of the bar, from the edge to the centre (bulk). Figures 20–22 show parameter versus solute relationships for Cr, Mo, Si, and Ti. See the Supplemental Materials for other solutes. Missing data for a particular section and parameter versus solute relationship, for example, for the section A1–B1–C1–D1–E1–F1–G1 for the δ versus Ti relationship in Figure 20, means that such a relationship was not found.

Note that for R = 1.2 cm/h the trend of the $\Delta\chi$ versus Ti relationship for the section A1–B1–C1–D1–E1–F1–G1 was opposite to that for the other sections, see the top row in Figure 20. Also note the opposite trends of the $\Delta\chi$ versus Ti and δ versus Ti relationships for R = 1.2 cm/h, see the top two rows in Figure 20. In the case of Mo, the same trend, namely, an increase in parameter value with Mo concentration, was observed for all three growth rates, see the bottom two rows in Figure 20 for the VEC versus Mo relationships for growth rates 1.2 and 6 cm/h, and Figure 21 for the VEC versus Mo and $\Delta\chi$ versus Mo relationships for the three growth rates.

In the case of Cr, the parameter δ decreased with increasing Cr concentration along the length of the bar for R = 1.2 cm/h, see the top row in Figure 22. A similar trend was exhibited by the $\Delta\chi$ versus Si relationship for the same growth rate, see the second row in Figure 22. The parameter δ increased with increasing Si concentration along the length of the bar for growth rates of 6 and 15 cm/h, see the third and fourth rows in Figure 22.

4.8. Relationships Between Solutes Along the Length of the OFZ Bar

The macrosegregation data for each growth rate, i.e., the concentration profiles between the edge and the centre of the bar showed that besides the changes in the parameters VEC, $\Delta\chi$, and δ with location (Figures 11–15) and the relationships between them (Figure 16), there were also strong relationships between solutes, see Figures 23 and 24. In particular, there were good correlations between the concentration of Ti, which increased as that of Cr increased, and locations along the length of the bar from the edge (A1–B1–C1–D1–E1) to the centre (A4–B4–C4–D4–E4) for all three growth rates (Figure 23). The correlation between Ti and Cr concentration along the section A4–B4–C4–D4–E4 for R = 6 cm/h had $R^2 < 0.8$ and is not included in Figure 23.

Also, there were good correlations ($R^2 > 0.8$) between the Ti and Nb concentrations along the edge of the bar for the three growth rates and along the centre of the bar for R = 15 cm/h (top row in Figure 24), and between Ti and Mo along the centre of the bar for the growth rates of 6 and 15 cm/h (bottom row in Figure 24), which showed the Ti concentration decreasing with increasing Nb concentration and increasing with Mo concentration along the length of the OFZ bar.

4.9. Nb_{ss} and Nb_5Si_3: Relationships Between Solutes and the VEC Versus $\Delta\chi$ Map of the Phases

In the Nb_{ss} solid solution there were relationships between Ti and Al, Cr, Mo, Nb, W, Al + Cr, and Mo + W. Figure 25 shows the data for R = 15 cm/h. Data for the other two growth rates can be found in the Supplemental Materials. In the Nb_{ss}, as the concentration of Ti increased so did those of Al and Cr, in agreement with [9,73,75,76], whereas the concentration of Mo, W, and Nb decreased in agreement with [9,13,44,77,78].

In the Nb_5Si_3 silicide there were relationships between Ti and Ge, Hf, Mo, and Nb, and between Nb and Hf, and Nb and Mo, see Figure 26, which shows the data for R = 15 cm/h, and the Supplemental Materials for the other growth rates. In the silicide, as the concentration of Ti increased, so did the concentrations of Hf and Ge, in agreement, with [34] and [11,79,80], respectively, whereas the concentration of Mo decreased, in agreement with the data for the heat-treated alloy RCCA/RM(Nb)IC alloy NT1.1 [12]. Furthermore, the concentration of Hf in the silicide decreased as that of Nb increased, in agreement with [76,79,80].

Synergy between solutes and entanglement between phases (see [1]), namely the Nb_{ss} and the Nb_5Si_3 silicide, is demonstrated for Ti, Mo, and Nb, and the Nb_{ss} and Nb_5Si_3 in Figure 27a–c for the growth rate of 15 cm/h. An increase in the concentration of Ti, Mo, or Nb in the solid solution was accompanied by an increase in the concentrations of the said elements in the silicide.

The VEC versus $\Delta\chi$ map of the Nb_{ss} solid solution and the Nb_5Si_3 silicide is shown in Figure 27d. The area for R = 1.2 cm/h (red triangle) expanded and "rotated" as the growth rate increased to R = 6 cm/h (blue triangle) and expanded further (green area) for R = 15 cm/h. There were good correlations between the phases, as indicated by the different R^2 values. In Figure 27d, R^2 = 0.8653 is for the Nb_{ss} and Ti-rich Nb_5Si_3 with Nb/(Ti + Hf) = 1; R^2 = 0.9827 is for the Nb_5Si_3 and Ti-rich Nb_5Si_3 with Nb/(Ti + Hf) $\geq$ 1, the growth rates R = 6 cm/h, R = 15 cm/h, and the termination; R^2 = 0.9972 is for the Nb_5Si_3 and Ti-rich Nb_5Si_3 with Nb/(Ti + Hf) < 1 and Nb/(Ti + Hf) > 1, the growth rates R = 6 cm/h, R = 15 cm/h, and the termination; R^2 = 0.9309 is for the Nb_5Si_3 and Ti-rich Nb_5Si_3 with Nb/(Ti + Hf) < 1 and Nb/(Ti + Hf) > 1, the growth rate R = 1.2 cm/h and the termination; R^2 = 0.9084 is for the Nb_{ss} and Ti-rich Nb_{ss} for the three growth rates and the termination; and R^2 = 0.9923 is for the Nb_{ss}, Nb_5Si_3, Ti-rich Nb_5Si_3 with Nb/(Ti + Hf) < 1, and Nb/(Ti + Hf) > 1, the growth rates R = 6 cm/h, R = 15 cm/h, and the termination. For the map of the phases in the termination and correlations between the phases, see Figure 9d.

As regards the silicide, the Nb/(Ti + Hf) ratio, which indicates tetragonal silicide when it is greater that one and hexagonal silicide when it is less than one [71], increased for the "normal" silicide and decreased for the Ti-rich silicide as the growth rate increased (Table 10). In the termination, the said ratio increased further for the "normal" silicide and the Ti-rich silicide formed with ratios less or greater than one. The data would thus suggest that, in the OFZ bar, as the growth rate increased from 1.2 cm/h to 15 cm/h, a tetragonal and a hexagonal silicide would become stable.

Regarding the solid solution, in the "normal" Nb_{ss} the Al + Cr and Mo + W sums, respectively, decreased and increased with increasing growth rate, and the Ti/(Al + Cr) ratio also increased, and these solute sums and ratio did not change from R = 15 cm/h into the termination. In the Ti-rich solid solution, which formed only when the growth rate increased to R = 15 cm/h and then in the termination, the Al + Cr and Mo + W sums, respectively, increased and decreased compared with the "normal" solid solution, and the Ti/(Al + Cr) ratio also decreased (Table 10). In the termination the two sums did not change but the ratio decreased. Note that the Al + Cr and Mo + W sums and the Ti/(Al + Cr) ratio are important for the strength and ductility of the Nb_{ss} [4].

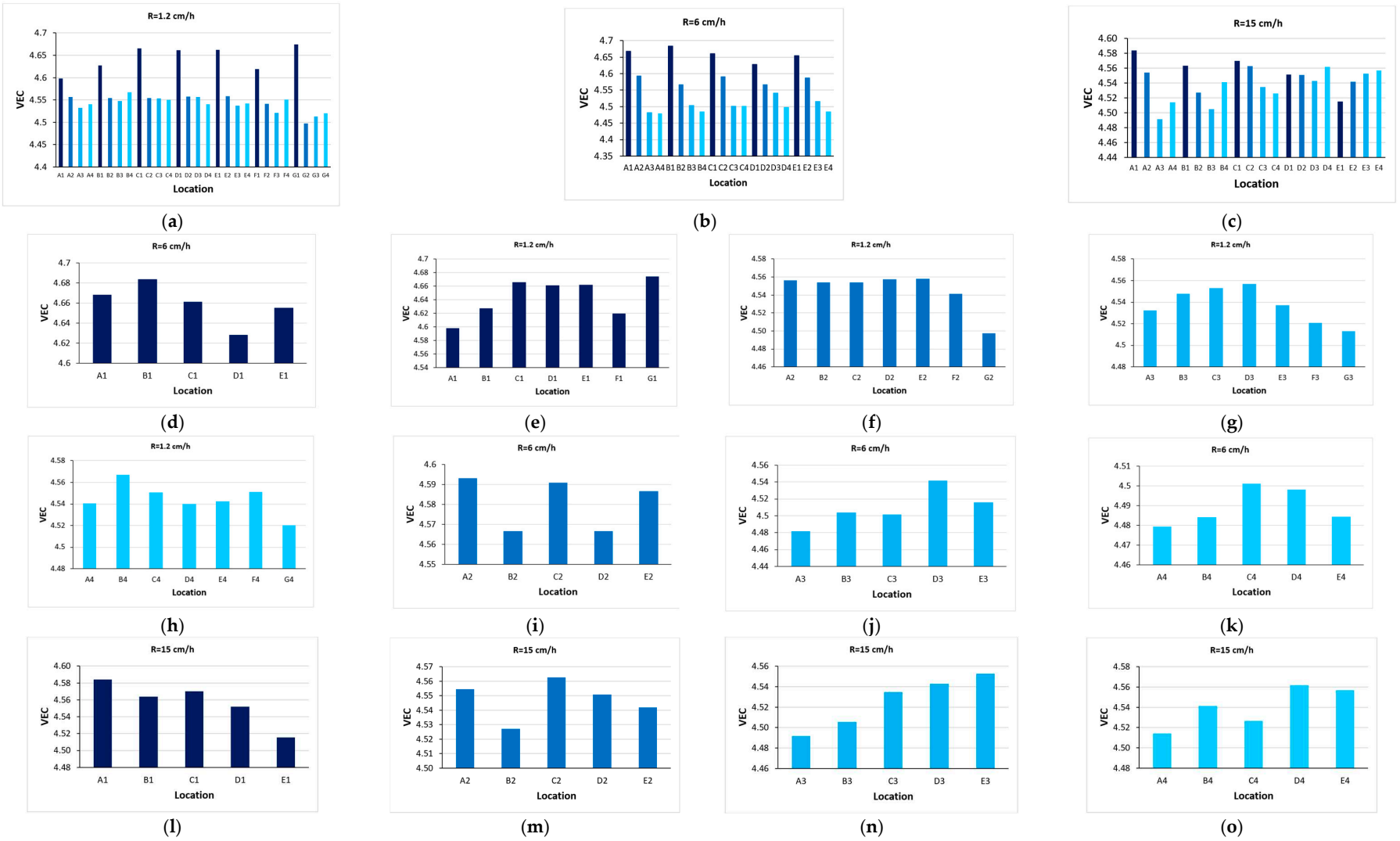

Figure 11. Parameter VEC versus location for the three growth rates. Top row from left to right: (**a**) R = 1.2, (**b**) R = 6, and (**c**) R = 15 cm/h. Second row (**d**–**g**) for R = 1.2 cm/h. Third row (**h**–**k**) for R = 6 cm/h. Forth row (**l**–**o**) for R = 15 cm/h.

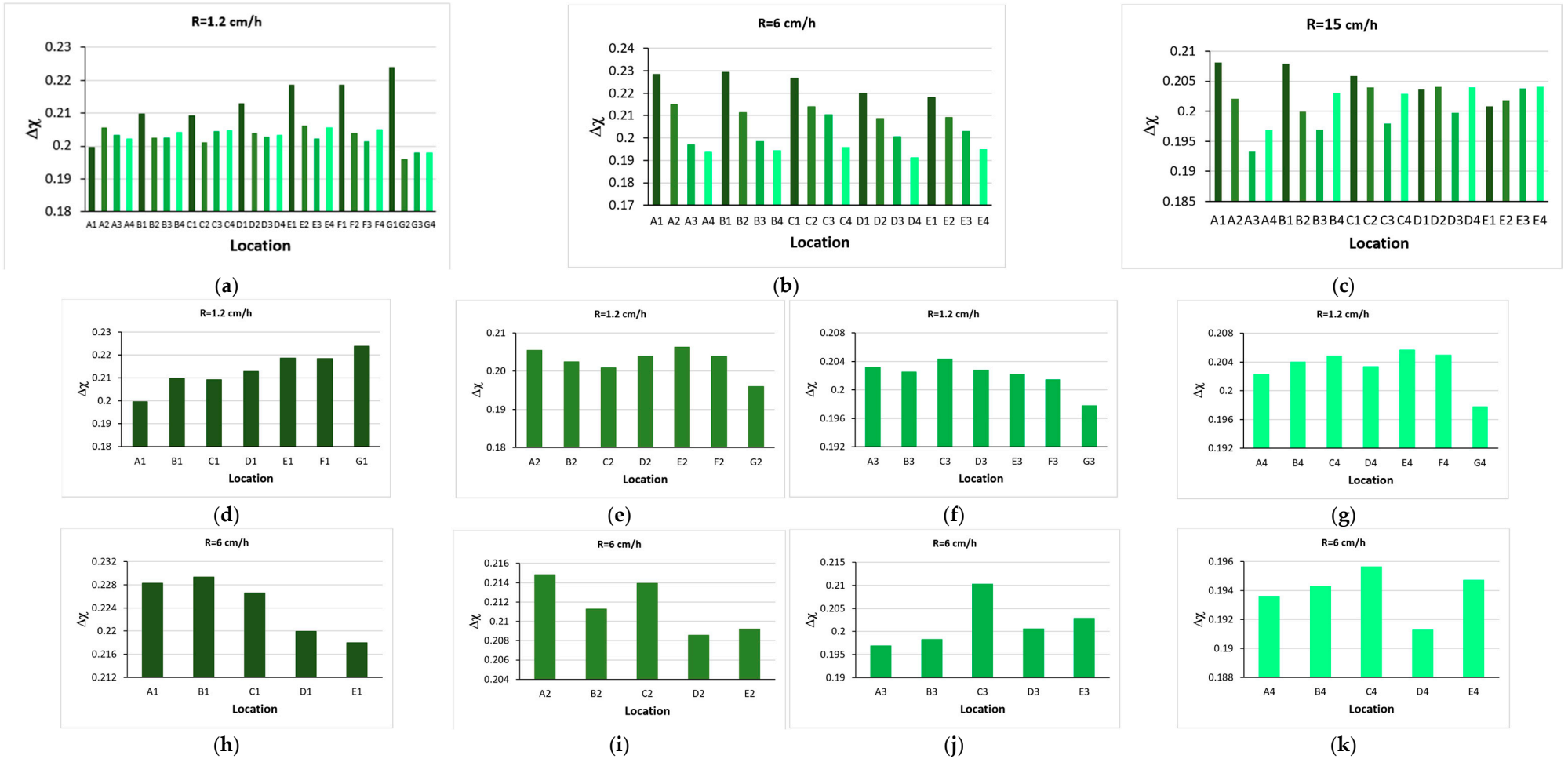

Figure 12. *Cont.*

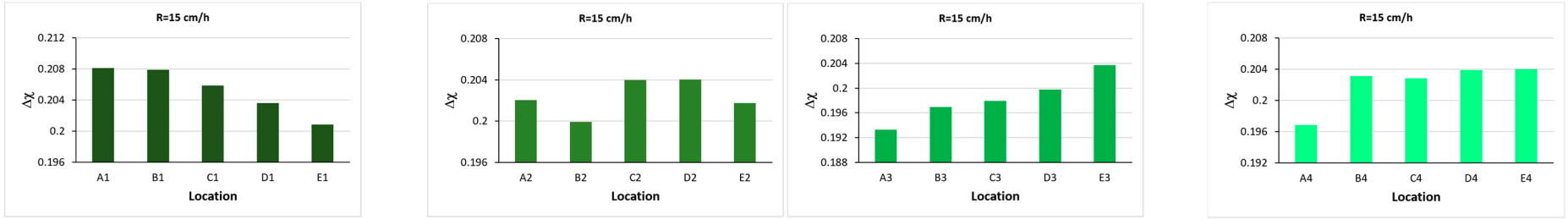

(**l**) (**m**) (**n**) (**o**)

Figure 12. Parameter Δχ versus location for the three Rs. Top row (**a**–**c**) from left to right: R = 1.2, 6, and 15 cm/h. Second row (**d**–**g**) for R = 1.2 cm/h. Third row (**h**–**k**) for R = 6 cm/h. Forth row (**l**–**o**) for R = 15 cm/h.

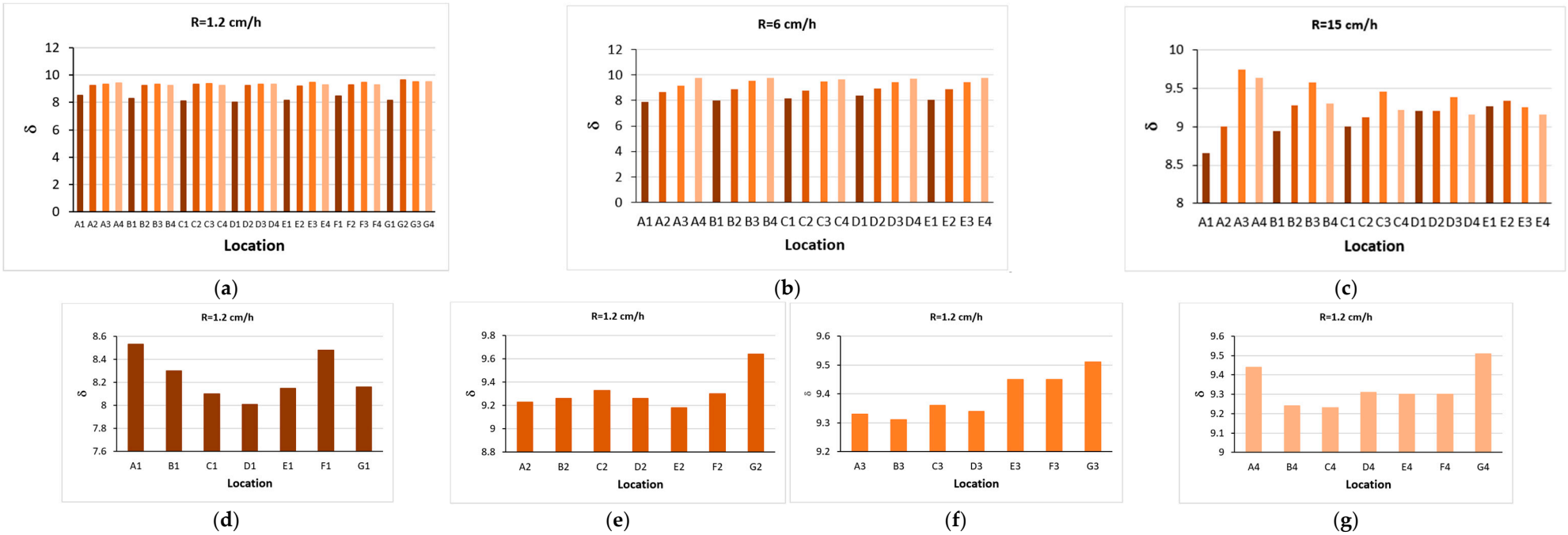

(**a**) (**b**) (**c**)

(**d**) (**e**) (**f**) (**g**)

Figure 13. *Cont.*

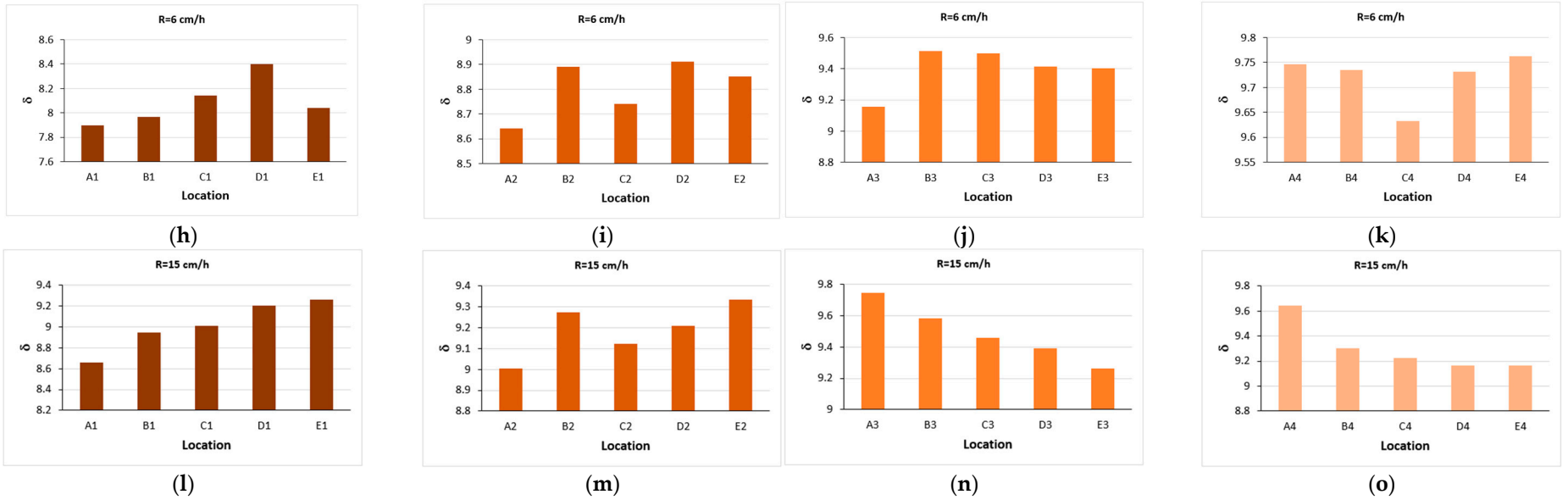

Figure 13. Parameter δ versus location for the three Rs. Top row (**a**–**c**) from left to right: R = 1.2, 6, and 15 cm/h. Second row (**d**–**g**) for R = 1.2 cm/h. Third row (**h**–**k**) for R = 6 cm/h. Forth row (**l**–**o**) for R = 15 cm/h.

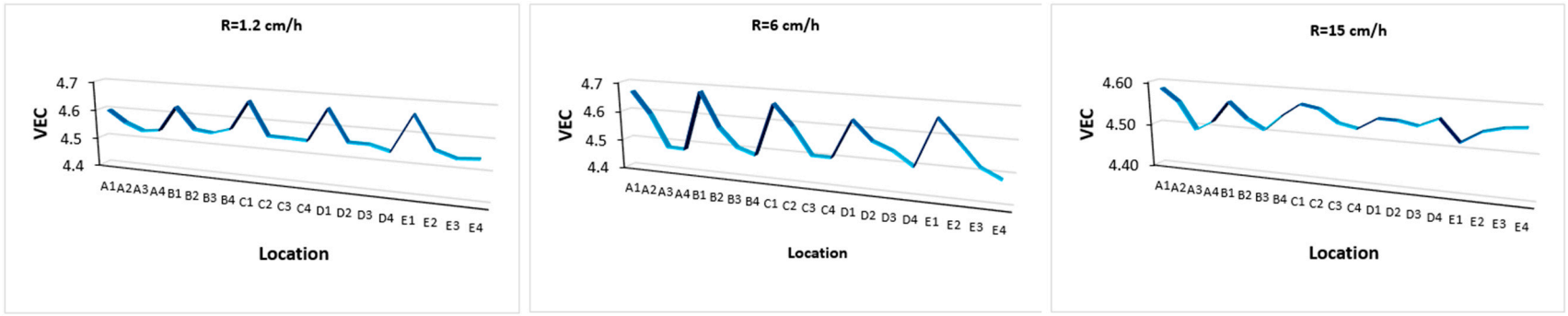

Figure 14. *Cont.*

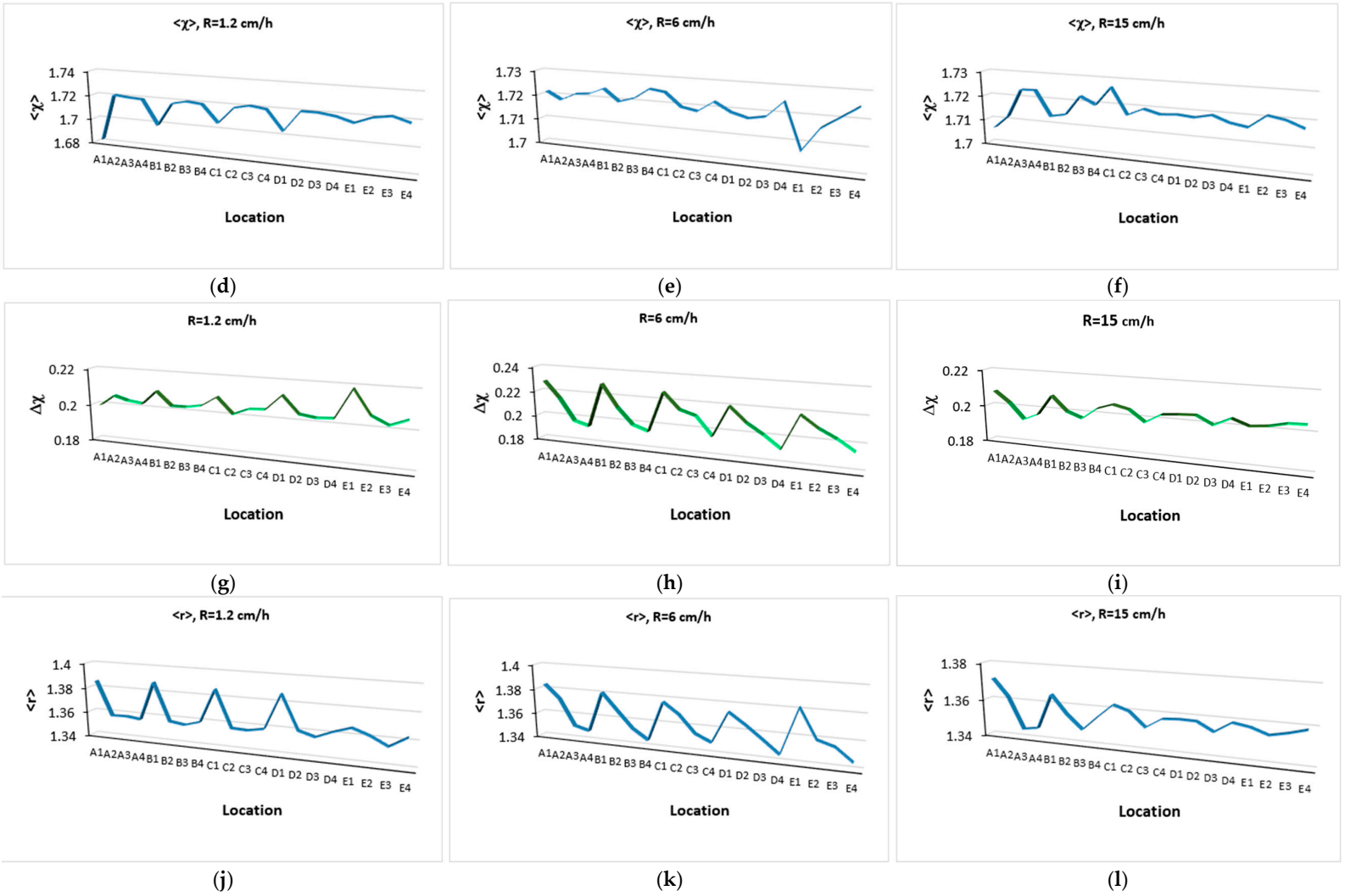

Figure 14. *Cont.*

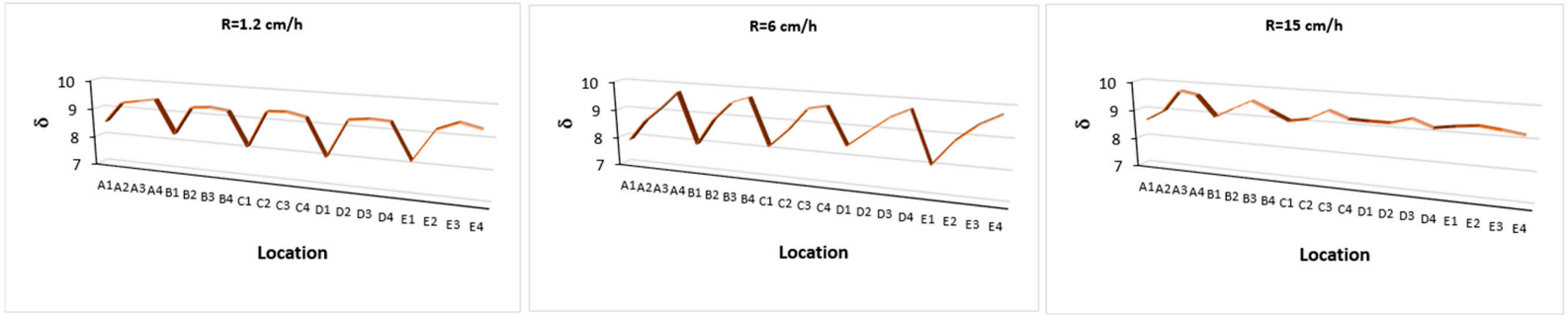

(**m**) (**n**) (**o**)

Figure 14. Parameters VEC (**a**–**c**), Δχ (**g**–**i**), and δ (**m**–**o**), and terms <χ> (**d**–**f**) and <r> (**j**–**l**) versus location for the three growth rates.

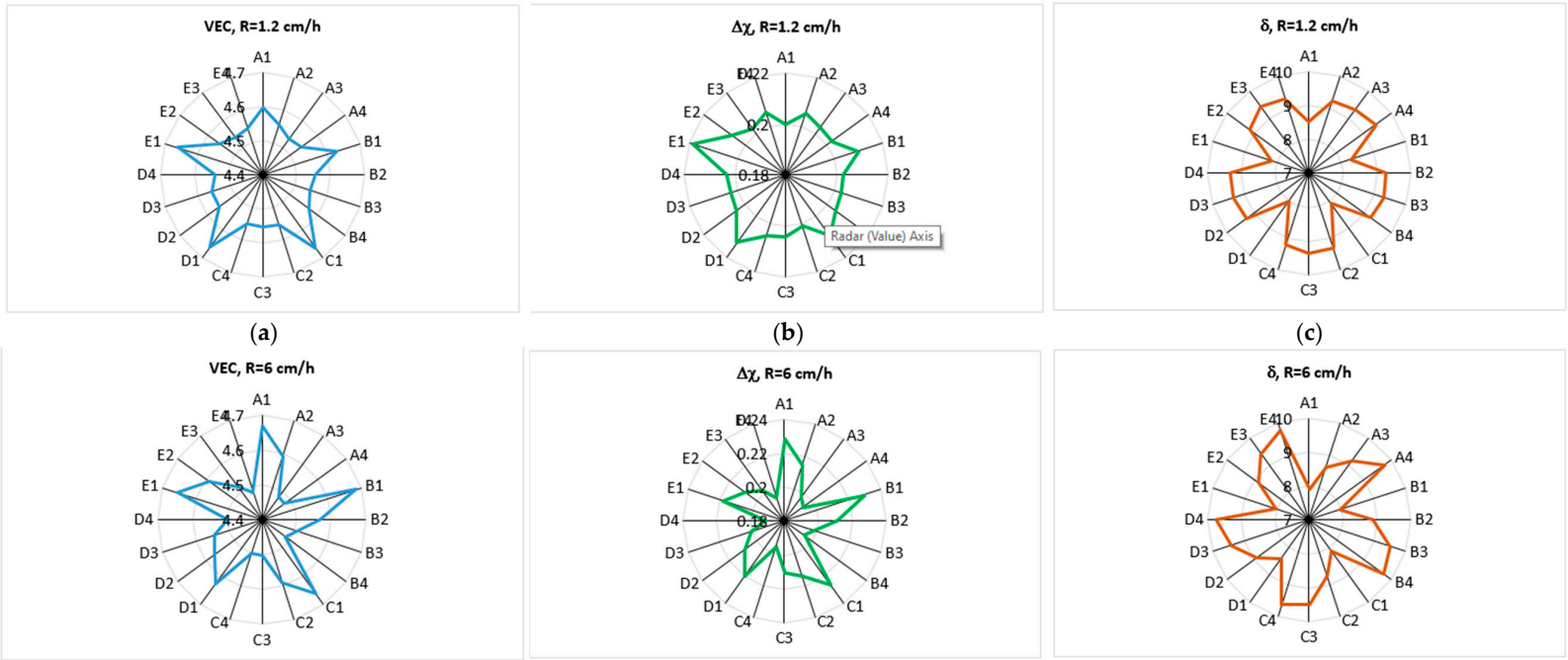

(**a**) (**b**) (**c**)

(**d**) (**e**) (**f**)

Figure 15. *Cont.*

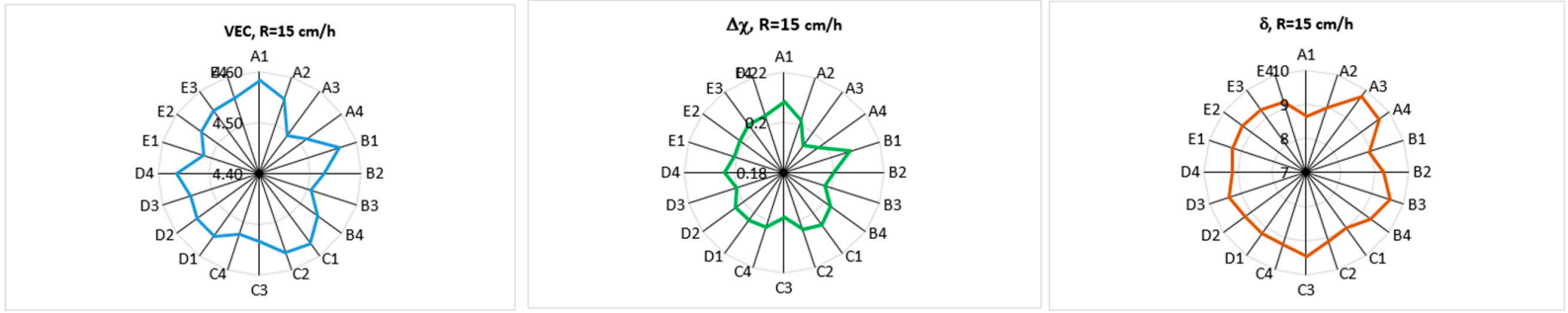

(**g**) (**h**) (**i**)

Figure 15. Parameters VEC, Δχ, and δ versus location for the three growth rates: (**a**–**c**) for R = 1.2 cm/h, (**d**–**f**) for R = 6 cm/h, and (**g**–**i**) for R = 15 cm/h. Same colours for VEC, Δχ and δ as in Figure 14a−c,g−i,m−o.

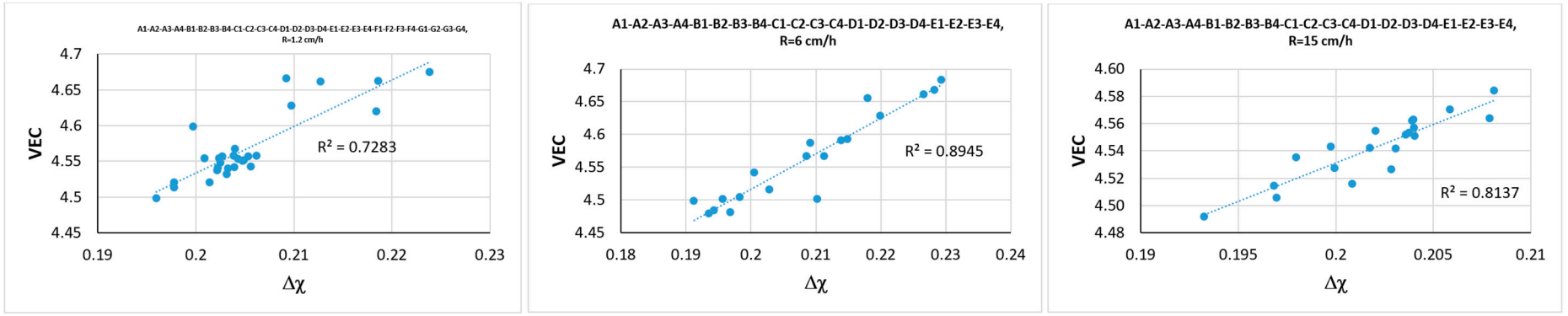

(**a**) (**b**) (**c**)

Figure 16. *Cont.*

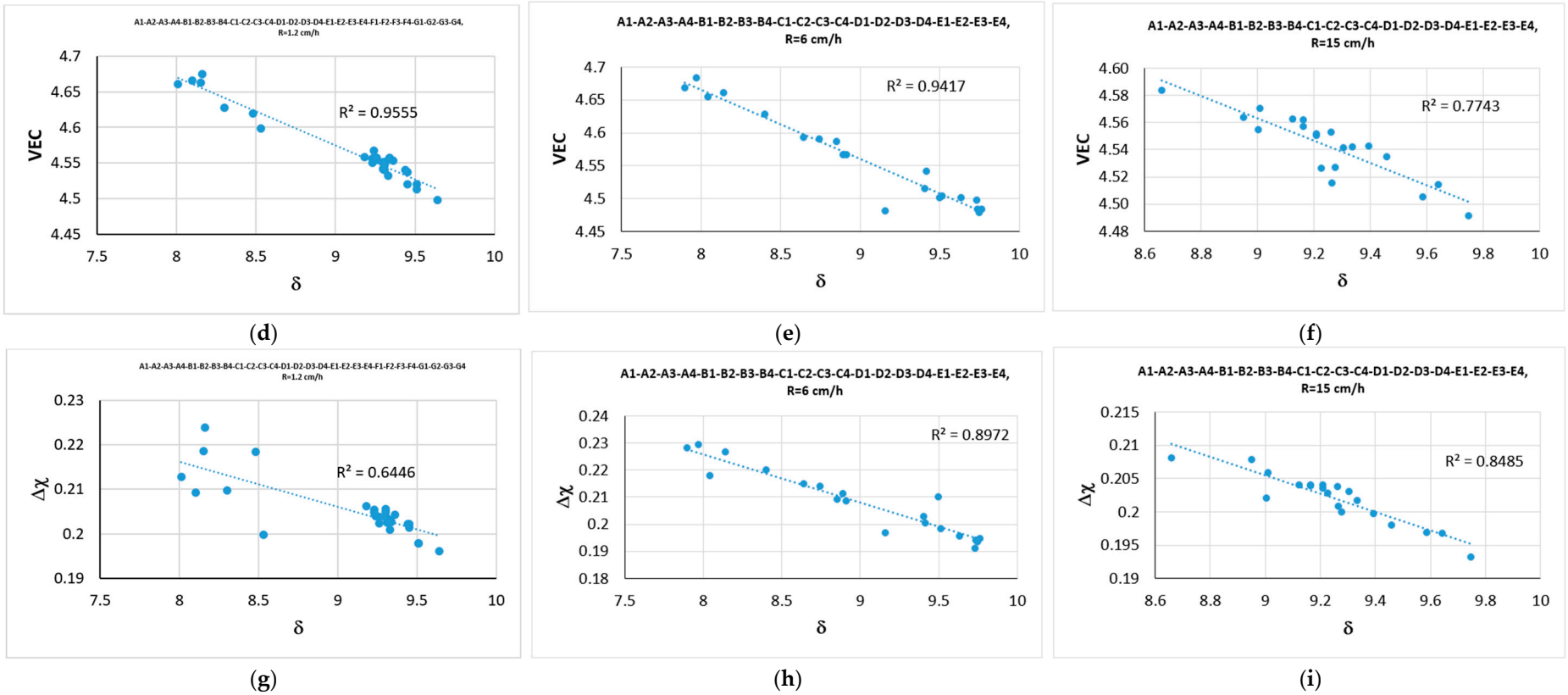

Figure 16. Relationships between the parameters VEC, Δχ, and δ for the three growth rates: (**a**–**c**) for VEC versus Δχ, (**d**–**f**) for VEC versus δ, and (**g**–**i**) for Δχ versus δ.

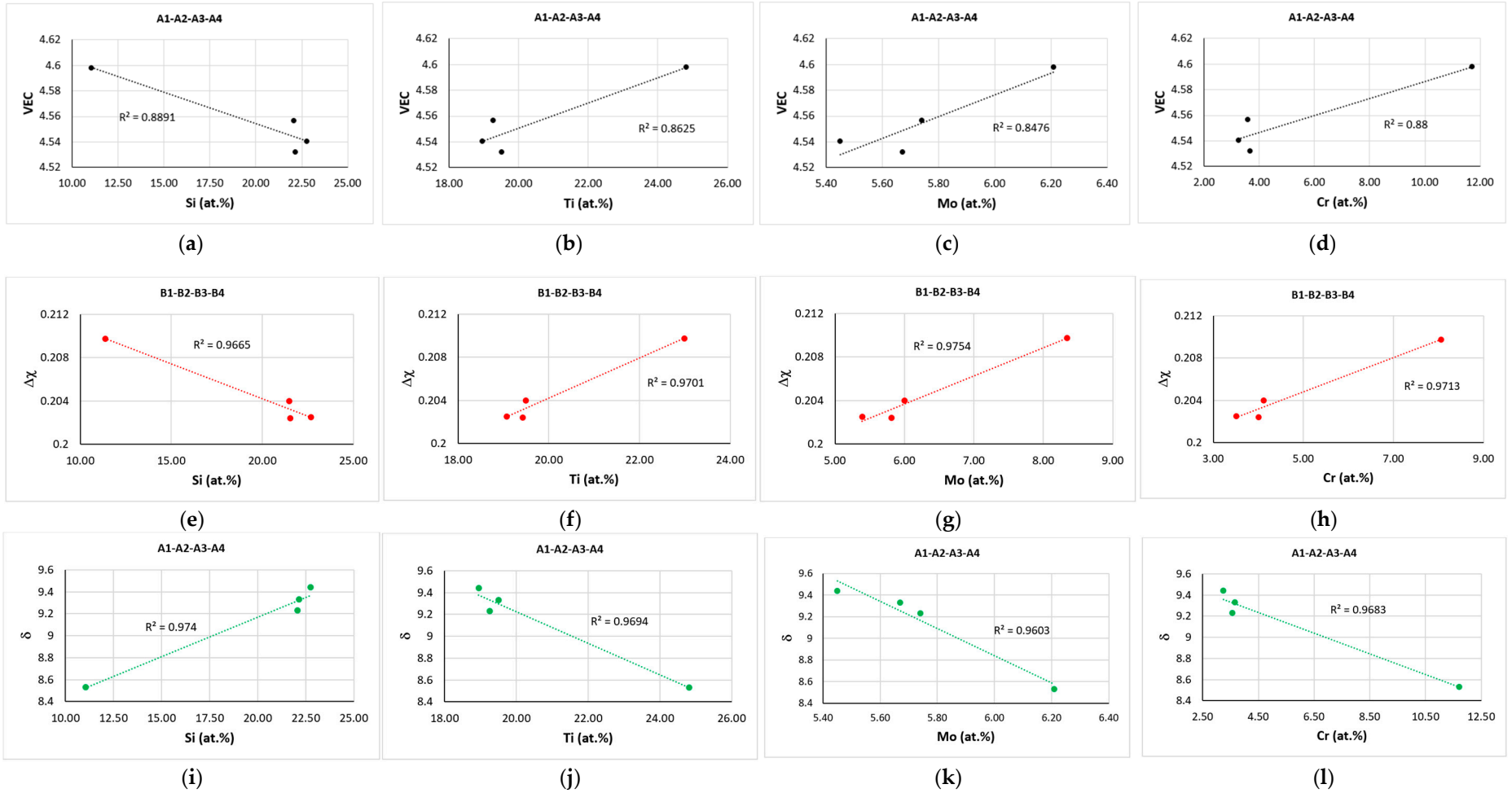

Figure 17. Relationships between the parameters VEC (**a**–**d**), Δχ (**e**–**h**), and δ (**i**–**l**), and the solutes Si (**a**,**e**,**i**), Ti (**b**,**f**,**j**), Mo (**c**,**g**,**k**), and Cr (**d**,**h**,**l**) for the sections A1–A2–A3–A4 (parameters VEC and δ) and B1–B2–B3–B4 (parameter Δχ) for R = 1.2 cm/h.

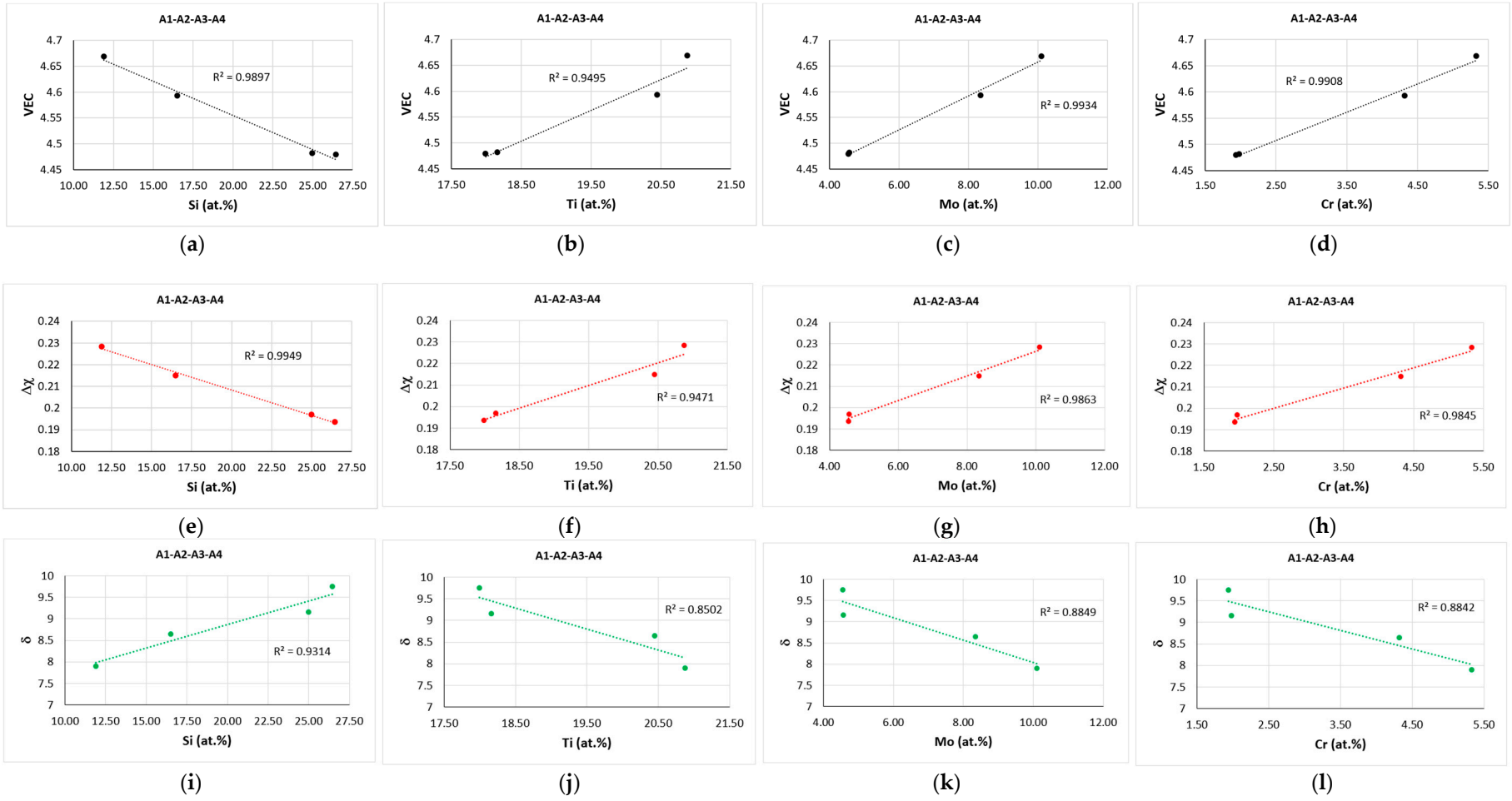

Figure 18. Relationships between the parameters VEC (**a**–**d**), Δχ (**e**–**h**), and δ (**i**–**l**), and the solutes Si (**a**,**e**,**i**), Ti (**b**,**f**,**j**), Mo (**c**,**g**,**k**), and Cr (**d**,**h**,**l**) for the section A1–A2–A3–A4 for R = 6 cm/h.

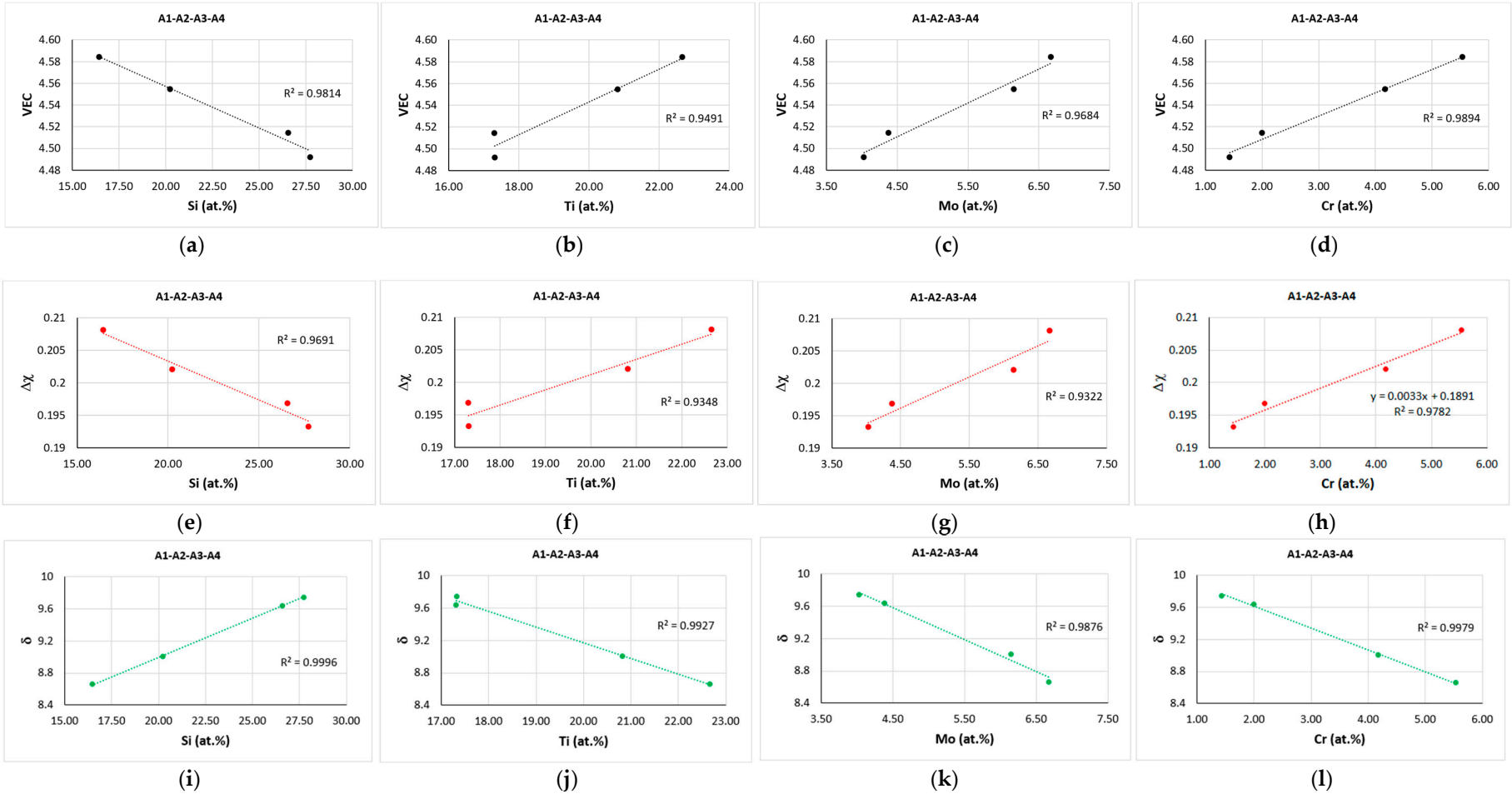

Figure 19. Relationships between the parameters VEC (**a**–**d**), Δχ (**e**–**h**), and δ (**i**–**l**), and the solutes Si (**a**,**e**,**i**), Ti (**b**,**f**,**j**), Mo (**c**,**g**,**k**), and Cr (**d**,**h**,**l**) for the section A1–A2–A3–A4 for R = 15 cm/h.

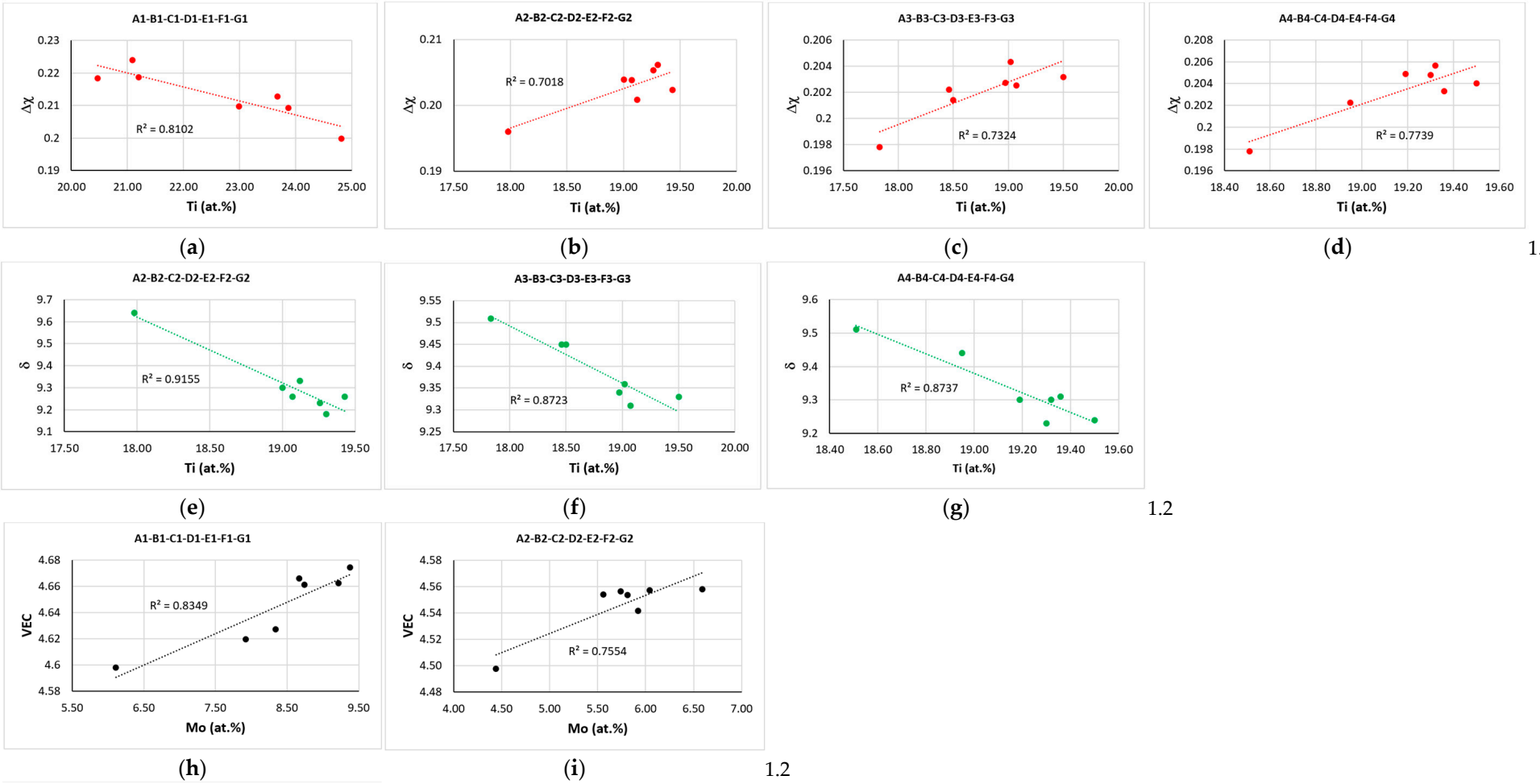

Figure 20. *Cont.*

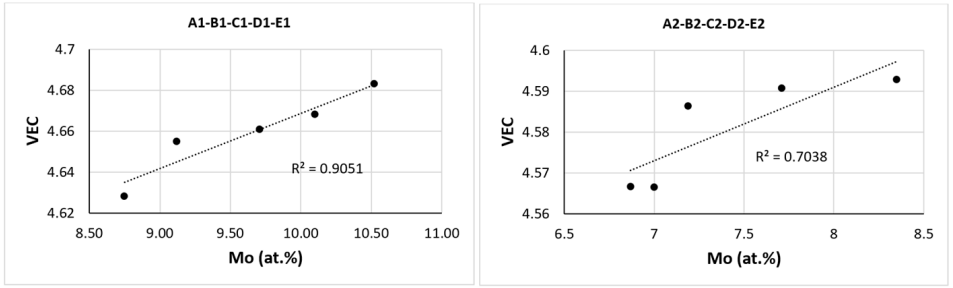

(**j**) (**k**) 6

Figure 20. Relationships between Ti (**a**–**g**) and Mo (**h**–**k**) with the parameters Δχ (**a**–**d**), δ (**e**–**g**), and VEC (**h**–**k**) for R = 1.2 cm/h, and between Mo and VEC for R = 6 cm/h for different sections along the length of the OFZ bar. The growth rate is shown at the end of each row of figures. First three rows (**a**–**i**) for R = 1.2 cm/h, and bottom row, (**j**,**k**) for R = 6 cm/h.

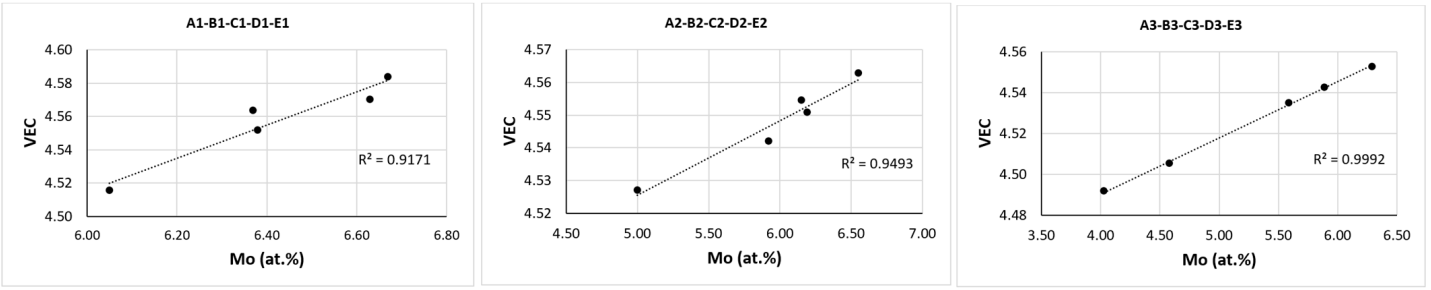

(**a**) (**b**) (**c**) 15

Figure 21. *Cont.*

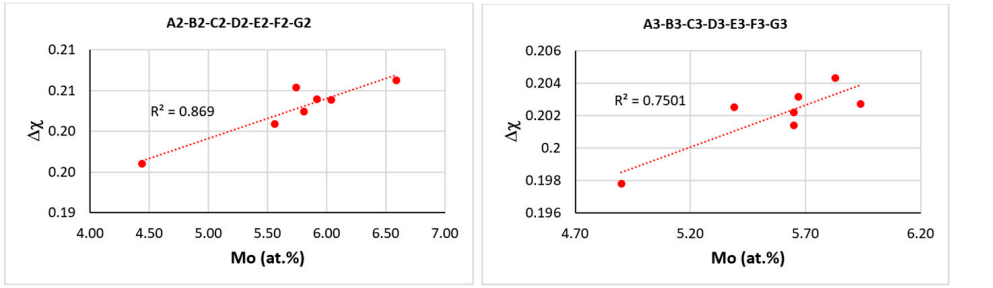

(**d**) (**e**) 1.2

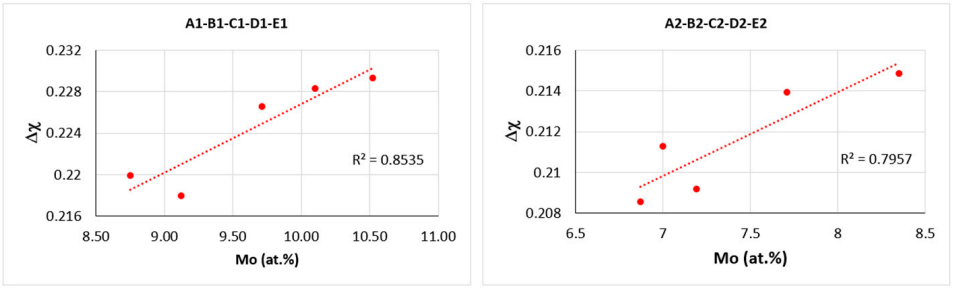

(**f**) (**g**) 6

Figure 21. Relationships between Mo with the parameters VEC and Δχ for the three growth rates for different sections along the length of the OFZ bar. The growth rate is shown at the end of each row of figures. Top row, (**a**–**c**) for R = 15 cm/h; middle row, (**d**,**e**) for R = 1.2 cm/h; and bottom row, (**f**,**g**) for R = 6 cm/h.

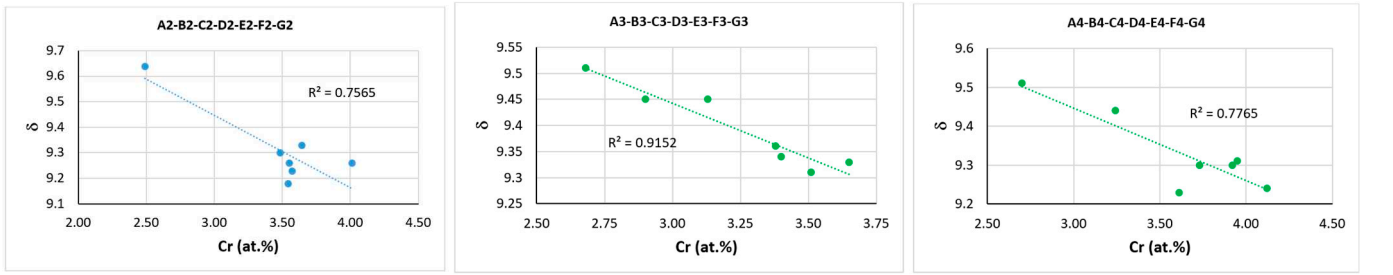

(**a**) (**b**) (**c**) 1.2

Figure 22. *Cont.*

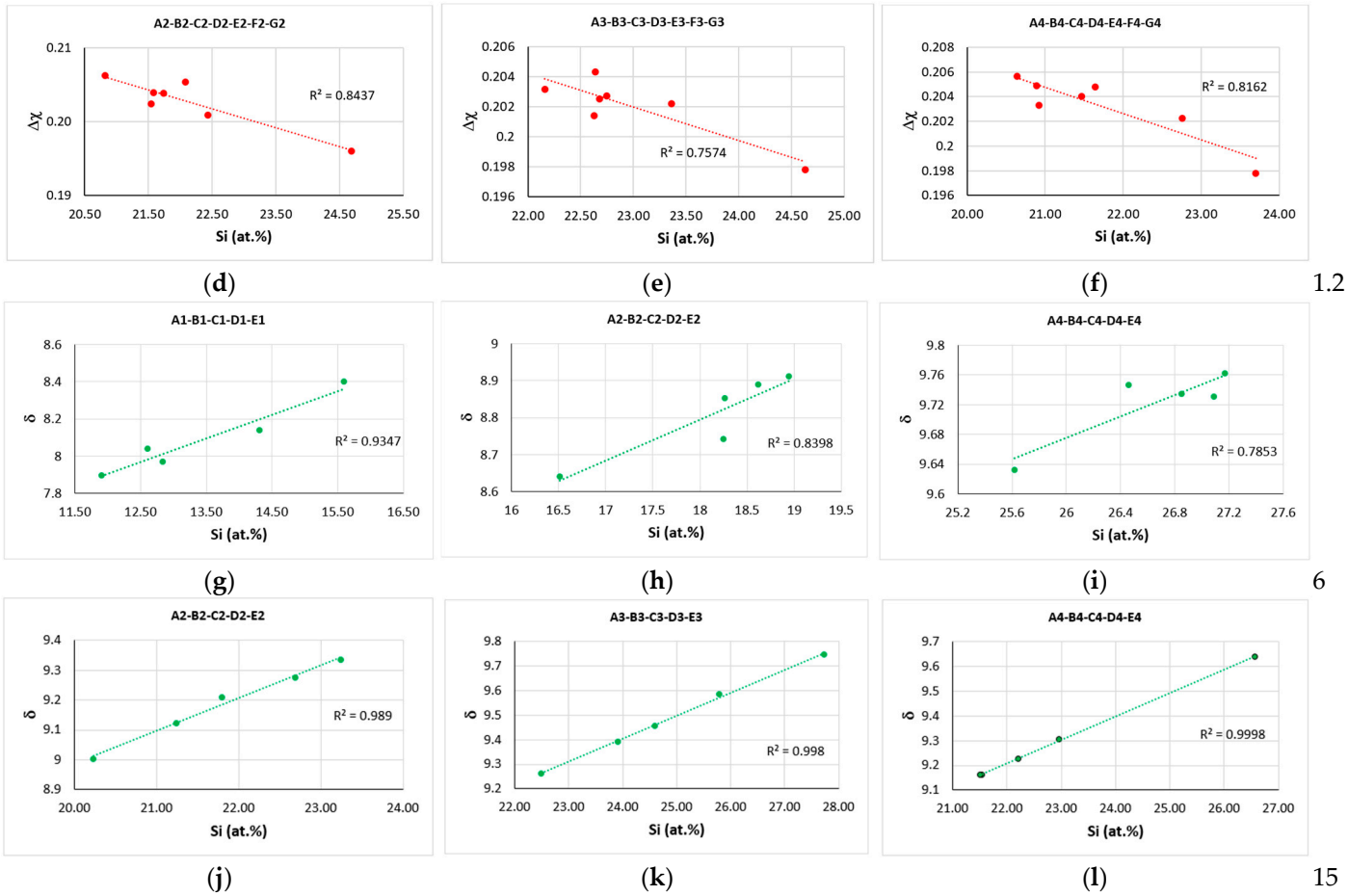

Figure 22. Relationships between Cr and Si with the parameters $\Delta\chi$ and δ for the three growth rates for different sections along the length of the OFZ bar. The growth rate is shown at the end of each row of figures. First two rows, (**a**–**c**) and (**d**–**f**) for R = 1.2 cm/h; third row, (**g**–**i**) for R = 6 cm/h; and bottom row, (**j**–**l**) for R = 15 cm/h.

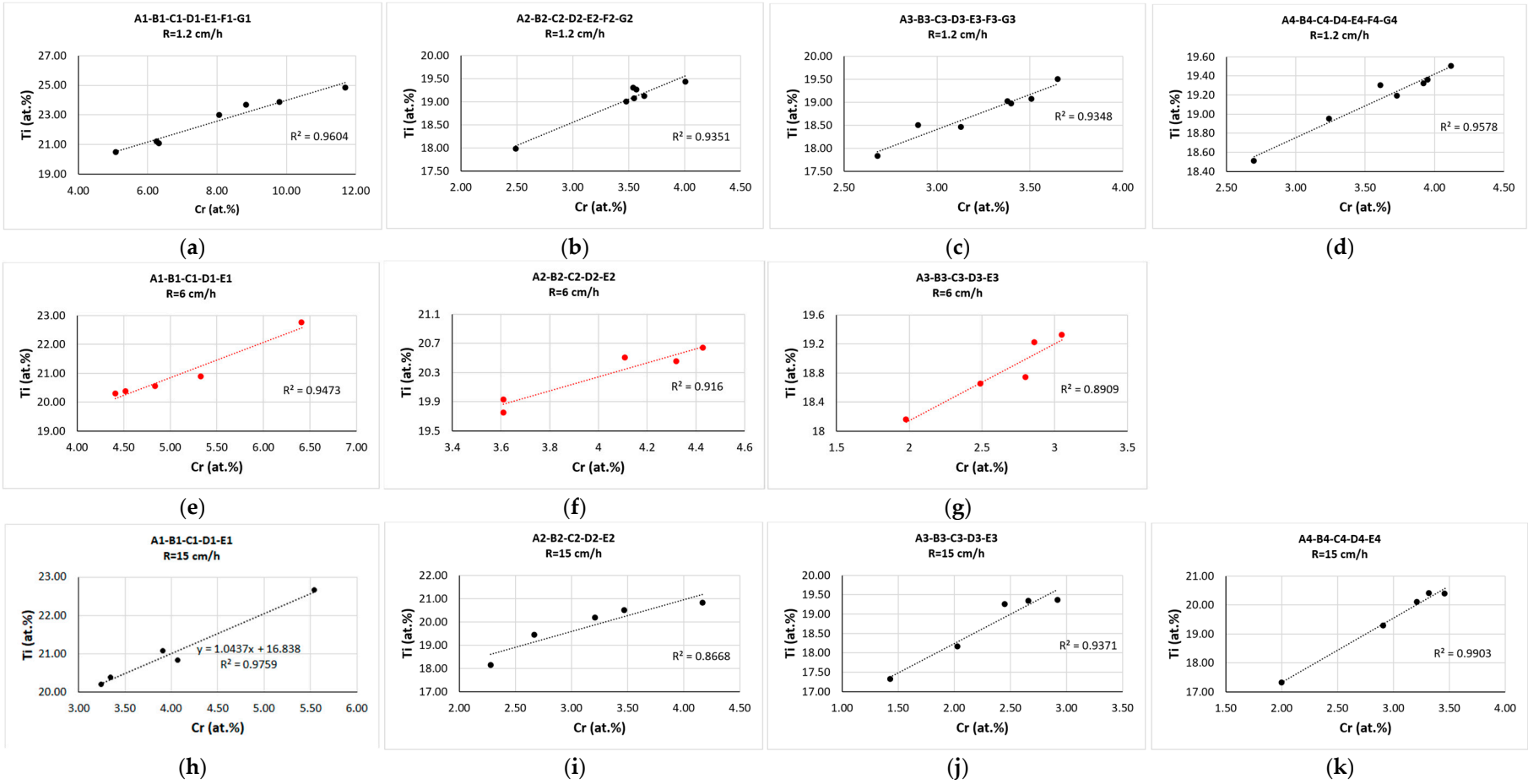

Figure 23. Ti versus Cr relationships along the length of the OFZ bar for the three growth rates: (**a**–**d**) for R = 1.2 cm/h, (**e**–**g**) for R = 6 cm/h, and (**h**–**k**) for R = 15 cm/h.

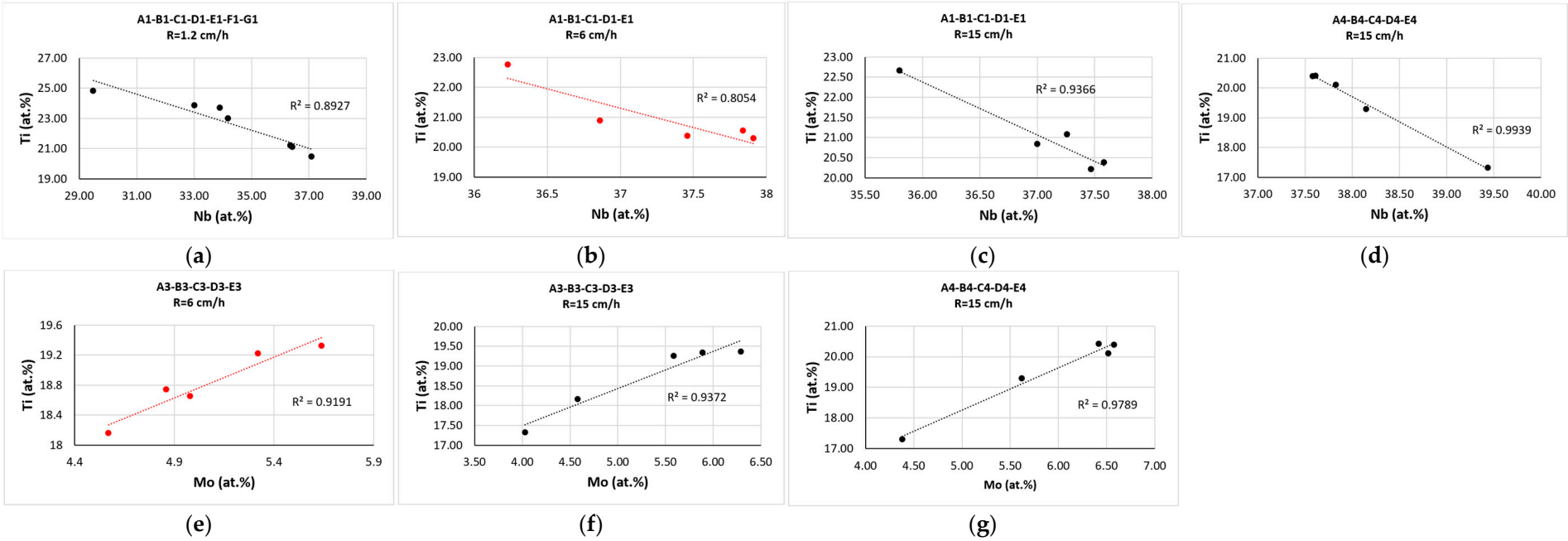

Figure 24. Ti versus Nb (**a**–**d**) or Mo (**e**–**g**) relationships along the length of the OFZ bar for specific sections and growth rates.

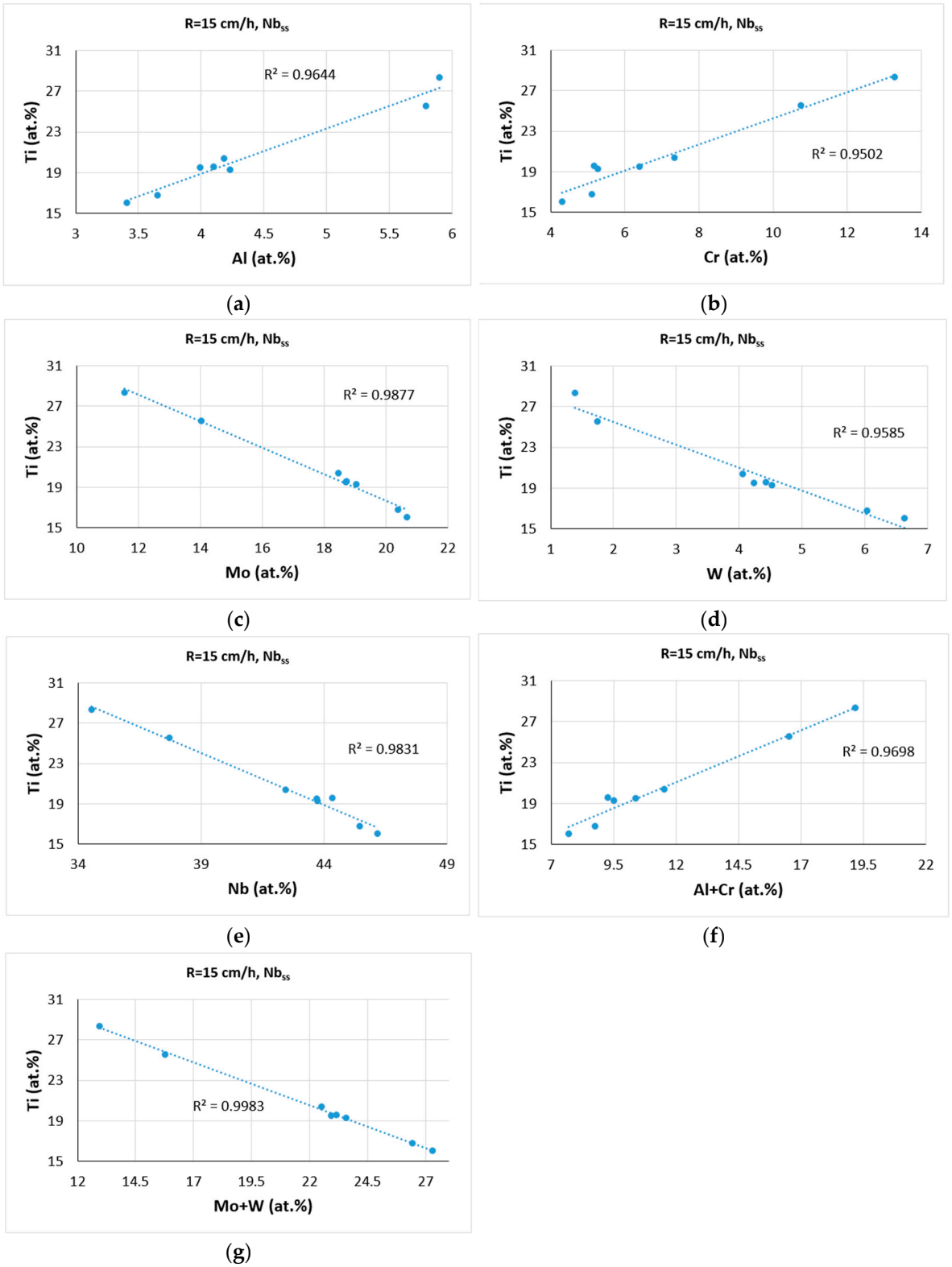

Figure 25. Relationships of Ti with the concentration of other solutes in the Nb_{ss} in the microstructure grown with R = 15 cm/h. Ti versus (**a**) Al, (**b**) Cr, (**c**) Mo, (**d**) W, (**e**) Nb, (**f**) Al + Cr, and (**g**) Mo + W.

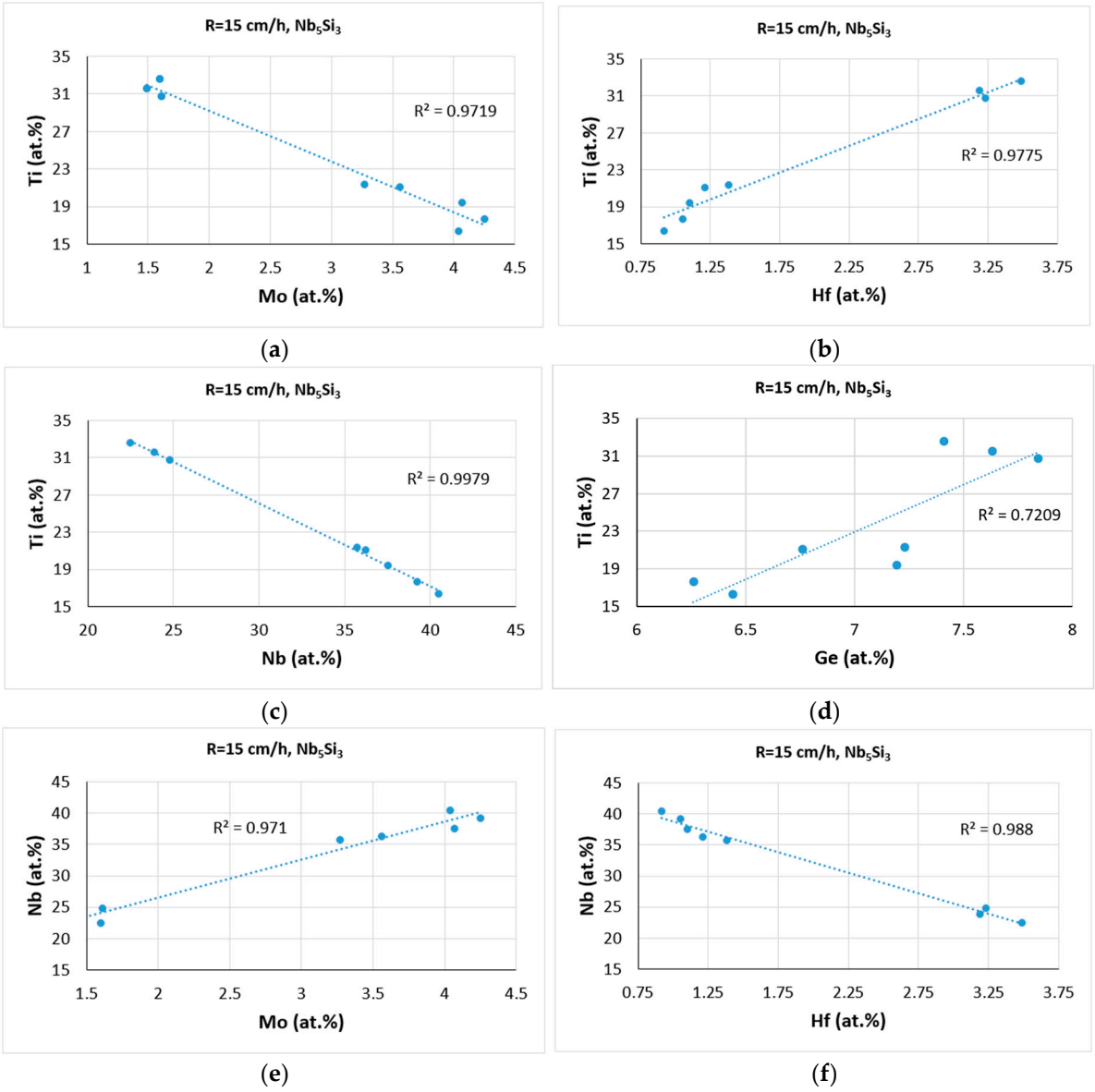

Figure 26. Relationships of Ti with the concentration of other solutes in the Nb_5Si_3 in the microstructure grown with R = 15 cm/h. Ti versus (**a**) Mo, (**b**) Hf, (**c**) Nb, and (**d**) Ge, and Nb versus (**e**) Mo and (**f**) Hf.

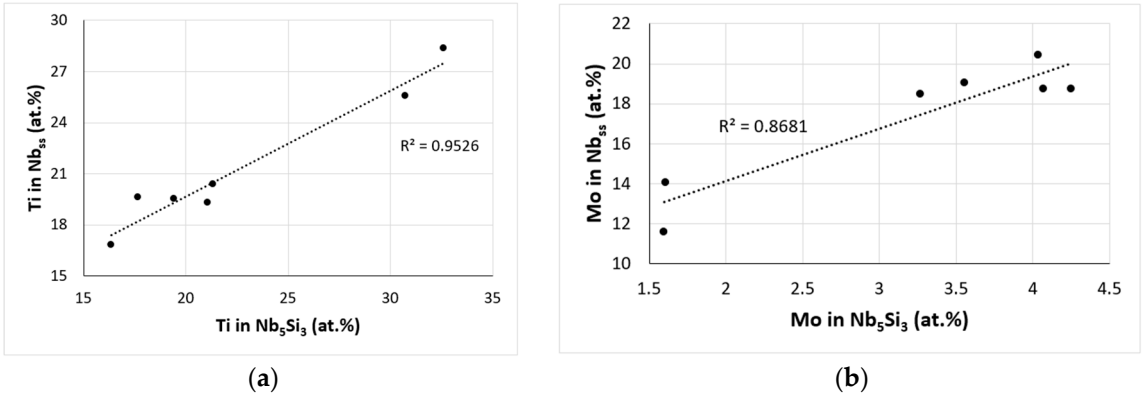

Figure 27. *Cont.*

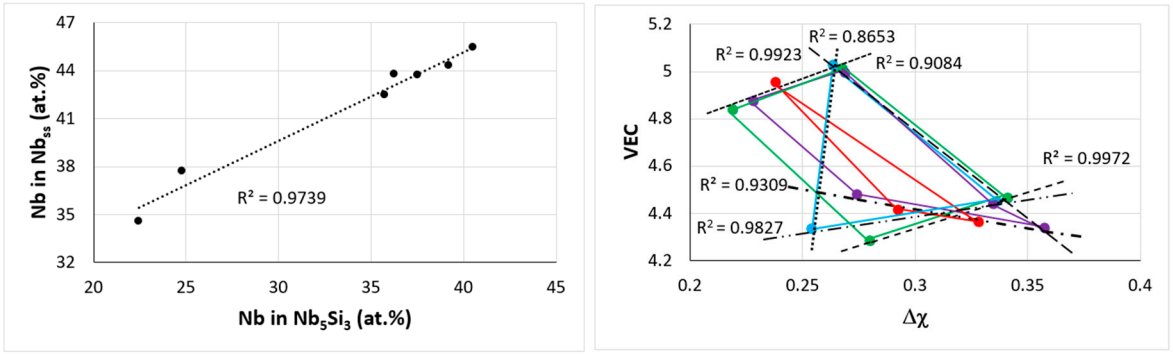

(**c**) (**d**)

Figure 27. Relationships of Ti, Mo, and Nb in the Nb_{ss} and Nb_5Si_3 in the microstructure grown with R = 15 cm/h. (**a**) Ti in Nb_{ss} versus Ti in Nb_5Si_3, (**b**) Mo in Nb_{ss} versus Mo in Nb_5Si_3, and (**c**) Nb in Nb_{ss} versus Nb in Nb_5Si_3. (**d**) VEC versus $\Delta\chi$ map of the solid solution (upper data) and silicide (lower data) in the centre (bulk) of the bar for the three growth rates and the termination. Colours are as follows: red for R = 1.2 cm/h, blue for R = 6 cm/h, green for R = 15 cm/h, and purple for termination. R^2 values are given for the black dashed lines in (**d**). See text for the R^2 values.

Table 10. Ratios and sums of solutes for the solid solution and the silicide for the three growth rates and the termination.

Growth Rate R (cm/h)	Nb_5Si_3	Ti-Rich Nb_5Si_3	Nb_{ss}			Ti-Rich Nb_{ss}		
	Nb/(Ti + Hf)		Al + Cr (at.%)	Mo + W (at.%)	Ti/(Al + Cr)	Al + Cr (at.%)	Mo + W (at.%)	Ti/(Al + Cr)
1.2	1.68	1.17	18.7	18.2	1.12	-	-	-
6	1.82	1	12	23.4	1.55	-	-	-
15	1.9	0.7	9.5	24.3	1.96	17.8	14.4	1.52
termination	2.23	0.73 1.6	9.3	24.4	1.9	18.2	15	1.4

5. Summary of the Experimental Work

The experimental results have shown how the synergy [1] of macrosegregation of the elements of the RCCA that we studied (Figures 3, 5, 8 and 10) and the growth rates R that we used in the direction solidification with OFZ gave the microstructures that were grown as R increased from 1.2 cm/h to 15 cm/h (Figures 4, 6 and 7).

The concentrations of elements from the solute profiles that resulted from the OFZ processing, e.g., Figure 3, was related (a) to each of the parameters VEC, $\Delta\chi$, and δ for different sections (i) across the thickness of the OFZ bar (Figures 17–19, and Supplemental Materials) and (ii) along the length of the OFZ bar (Figures 20–22 and Supplemental Materials), or to each other for different sections (ii) along the length of the OFZ bar (Figures 23 and 24 and Supplemental Materials), and demonstrated the synergy and entanglement [1] of processing, parameters, and solutes. There was synergy of solutes in the Nb_{ss} solid solution and Nb_5Si_3 silicide for the three growth rates (Figures 25 and 26 and Supplemental Materials), and synergy and entanglement of the two phases (Figure 27).

As a result of the aforementioned synergies and entanglements [1], there were similarities and differences as each parameter changed in the OFZ bar (Figure 11a–c, Figure 12a–c, and Figure 13a–c) and along the length of the bar from the edge to the centre (Figure 11d–o, Figure 12d–o, and Figure 13d–o), with reduced variability of parameters as the growth rate increased (Figure 14a–c,g–i,m–o) and opposite trends for the parameter δ compared with VEC and $\Delta\chi$ (Figure 15).

Also, because of the aforementioned synergies and entanglements [1], there were relationships between the parameters for each growth rate in the OFZ bar with VEC increasing with increasing Δχ and decreasing with increasing δ, and Δχ decreasing with increasing δ (Figure 16), and for all growth rates (Figure 28), with larger spread of the data for the two lower growth rates (Figure 14a,b,g,h,m,n and Figure 28).

On account of the synergy and entanglement of processing, parameters, and solutes in each part of the OFZ bar that was grown with a specific growth rate, properties would "emerge" [81]. In the next section, we comment on the creep and oxidation properties that are calculated as guided by the alloy design methodology NICE [1,4,5,10].

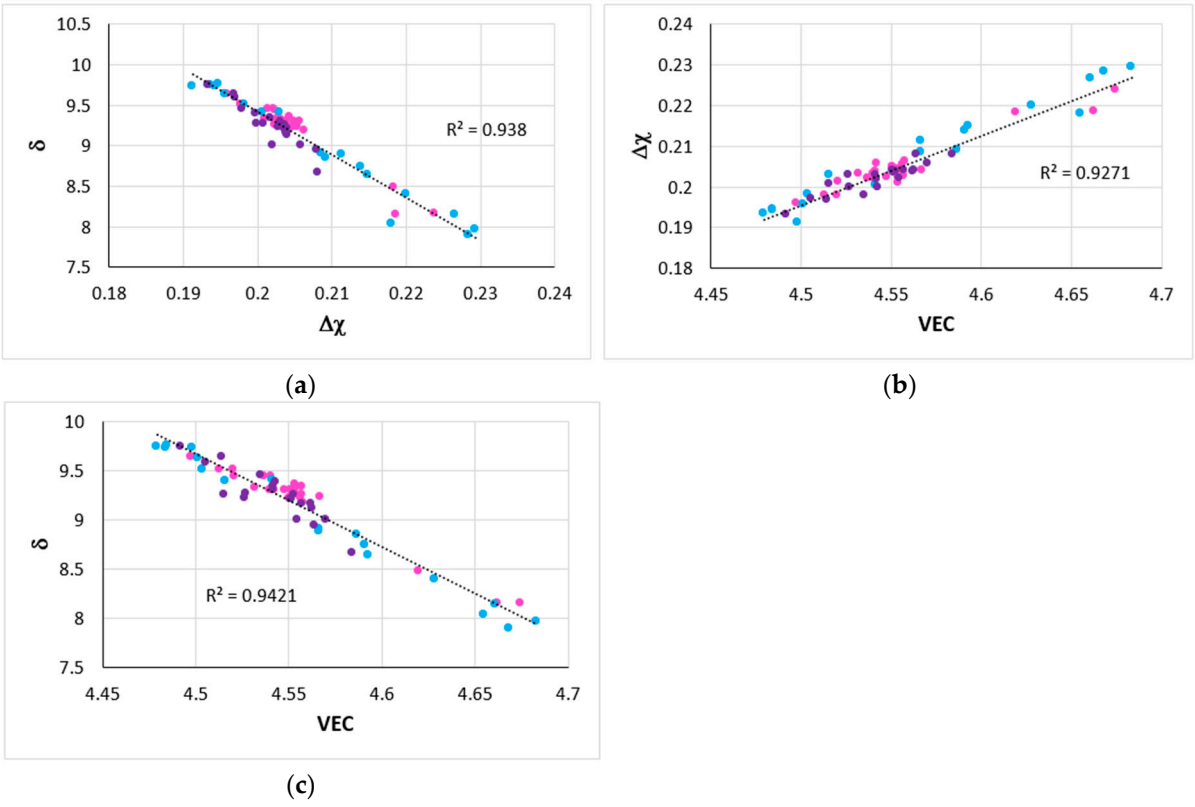

Figure 28. Relationships between the parameters VEC, Δχ, and δ in the OFZ bar. Data for all three growth rates. (**a**) δ versus Δχ, (**b**) Δχ versus VEC, (**c**) δ versus VEC. Colours are as follows: pink for R = 1.2 cm/h, blue for R = 6 cm/h, and purple for R = 15 cm/h.

6. Calculated Creep and Oxidation Properties of the OFZ Bar

The alloy design methodology NICE has shown that experimental data for alloy or phase properties is linked with the alloy or phase parameters VEC, Δχ, and δ [10]. Thus, experimental data is (can be) used to derive equations that relate said parameters with properties. The relationships between the creep rate of RM(Nb)ICs and their parameters δ, Δχ, and VEC concern the contributions to creep made by intrinsic resistances to deformation, not extrinsic ones, see [4,10,75].

NICE shows that in order to meet the creep goal or to have low creep rates, the alloy parameters VEC and Δχ should be high and the parameter δ should be low. On the other hand, for low mass change in isothermal oxidation, the alloy parameter VEC should be low and the parameters Δχ and δ should be high. Of the above three parameters, Δχ has the strongest effect on the creep rate [10]. On account of the different trends of the said parameters and alloy properties, namely creep and oxidation, the alloy designer can either aim to satisfy a particular property, which is possible for RM(Nb)ICs and RCCAs/RM(Nb)ICs

vis-à-vis their creep [4], or to achieve a balance of properties, which (the balance) is agreed with industry. At the same time as s/he addresses each of these options, the alloy designer should take into account material costs, issues related to the processing of the alloy, e.g., macrosegregation of solutes in cast alloys (which is unfortunately ignored in current research on cast metallic UHTMs) or contamination with interstitials, processing costs, risk (IRIS), material–environment interactions (CEMIs), and sustainability (ETS and ESSERE) (see the Abbreviations and [1]).

Creep rate data (e.g., [4,10,75,82–84]) and mass change data from isothermal oxidation experiments (see [1] for references) for RM(Nb)ICs and RCCAs/RM(Nb)ICs with TM, RM, and simple metal and metalloid element additions in similar composition ranges have been linked with each of the aforementioned parameters. The resulting mathematical relationships are used in NICE [10] to select alloys to meet a specific property goal or to obtain a balance of properties [1,4,5,10,75]. We have used such relationships to calculate the creep rate for the goal condition (T = 1200 °C, σ = 170 MPa [10]) and mass change for isothermal oxidation at 1200 °C or 800 °C for 100 h for different locations along the length of the OFZ bar. Examples are shown in Figure 29a,b for creep and Figure 29c,d for isothermal oxidation at 1200 °C for the edge and the centre of the bar from the start of growth with R = 1.2 cm/h to the end of growth with R = 15 cm/h.

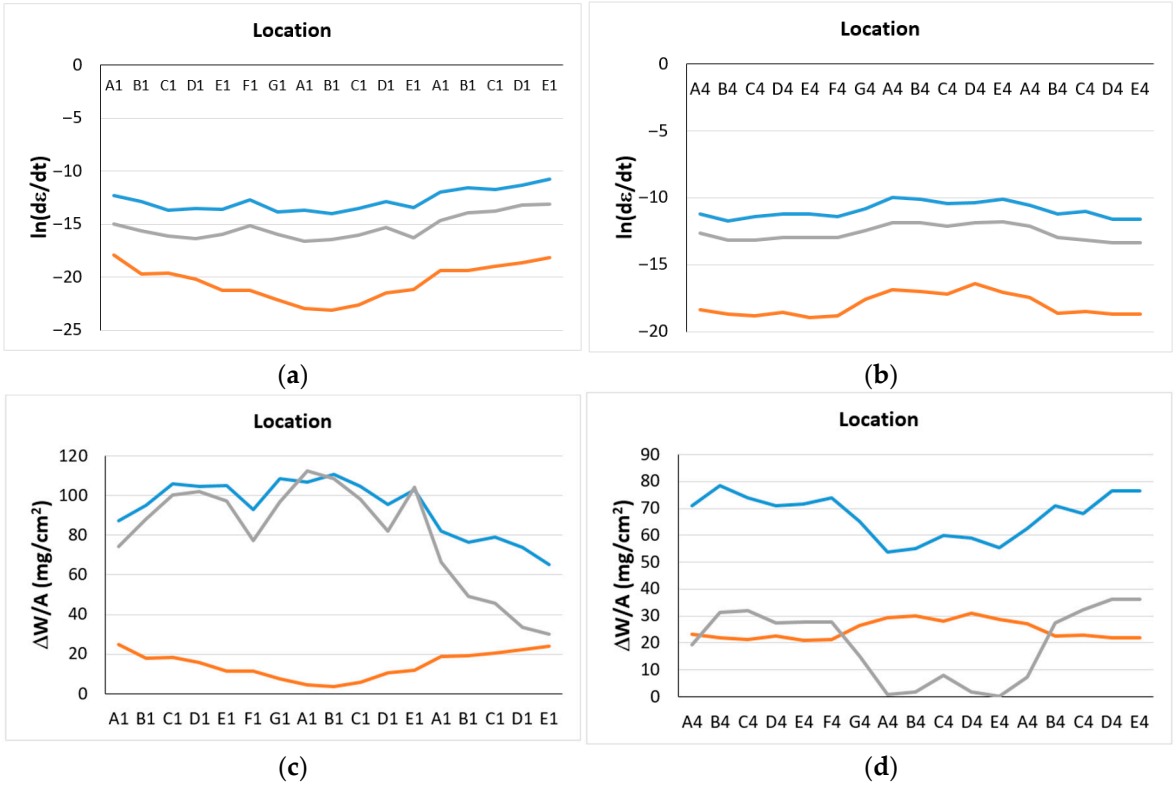

Figure 29. Calculated creep rate (**a**,**b**) (shown as ln(dε/dt)) for the goal condition, namely for T = 1200 °C and σ = 170 MPa, see [10]), and calculated mass change (**c**,**d**) for isothermal oxidation at 1200 °C for 100 h along the length of the OFZ bar for locations at the edge and centre of the bar (see Figure 2b). Blue line for parameter VEC, grey line for parameter δ, and orange line for parameter Δχ.

Figure 30 shows the average creep rate for T = 1200 °C, σ = 170 MPa (Figure 30a) and the average mass change for isothermal oxidation at 1200 °C for 100 h (Figure 30b). Four locations were considered along the length of the bar, from the edge towards the centre of the bar, which in Figure 30 are indicated as Ai–Bi–Ci–Di–Ei–Fi–Gi–Aj–Bj–Cj–Dj–Ej–Ay–By–Cy–Dy–Ey, where i, j, and y = 1 at the edge of the bar and i, j, and y = 4 at the centre

of the bar (see Figure 2b). For each location, e.g., along the edge of the bar where i, j, and y = 1, the average creep rate in Figure 30a was $\ln(d\varepsilon/dt) = ([\ln(d\varepsilon/dt)]_{VEC} + [\ln(d\varepsilon/dt)]_{\Delta\chi} + [\ln(d\varepsilon/dt)]_{\delta})/3$ and the average mass change in Figure 30b was $\Delta W/A = ([\Delta W/A]_{VEC} + [\Delta W/A]_{\Delta\chi} + [\Delta W/A]_{\delta})/3$. Note that the calculated average creep rate for each location along the length of the bar is the creep rate due to intrinsic resistances to deformation, see [4,10].

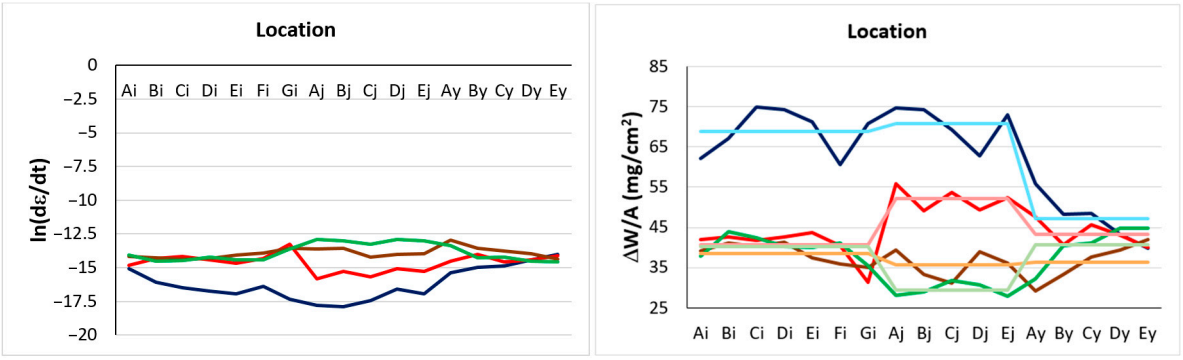

(**a**) (**b**)

Figure 30. Calculated (**a**) average creep rate (see text) and (**b**) average mass change (see text) for locations along the length of the OFZ bar. Locations are indicated as Ai–Bi–Ci–Di–Ei–Fi–Gi–Aj–Bj–Cj–Dj–Ej–Ay–By–Cy–Dy–Ey, where i, j, and y = 1 at the edge of the bar and i, j, and y = 4 at the centre of the bar (see Figure 2b). In (**a**,**b**), colours are as follows: dark blue for i,j, and y = 1, red for i,j, and y = 2, brown for i,j, and y = 3, and green for i,j, and y = 4. In (**b**), soft blue, soft red, soft brown, and soft green show average value for each i, j, and y. Creep rate for the goal condition (T = 1200 °C and σ = 170 MPa, see [10]), and mass change for isothermal oxidation at 1200 °C for 100 h.

According to NICE, along the edge of the bar the lowest creep rate would be for the growth with R = 6 cm/h, with the creep rate mostly decreasing along the length grown with R = 1.2 cm/h, and increasing for that grown with R = 15 cm/h, and with almost similar creep rates at the start and end of the OFZ run (Figure 29a). Regarding the centre (bulk) of the bar, the highest creep rate would be for the growth with R = 6 cm/h, with the creep rate not changing significantly for the growth with R = 1.2 cm/h, and decreasing from the transition from R = 6 cm/h to R = 15 cm/h to the end of the OFZ run (Figure 29b). Along the edge and the centre of the bar, the contribution to creep rate calculated by NICE was highest for VEC and lowest for Δχ (Figure 29).

Also according to NICE, along the edge of the bar the value and variability of mass change calculated from the parameters VEC and δ would be similar to the start of the growth with R = 15 cm/h, after which the mass change calculated from δ would decrease noticeably compared with that calculated from VEC and would approach the mass change calculated from the parameter Δχ. The latter would decrease from the start of growth with R = 1.2 cm/h to just after the start of growth with R = 6 cm/h and then would increase to the end of the OFZ run (Figure 29c). In the centre of the bar, there would be similar variability of mass change from the start to the end of the OFZ run, with very low mass change calculated from the parameter δ for the growth with R = 6 cm/h. The mass change calculated from the parameter Δχ would be lowest for almost the whole of the growth with R = 1.2 cm/h and for the growth with R = 15 cm/h (Figure 29d).

According to NICE, for the part of the bar that was grown with R = 1.2 cm/h the average creep rate would be lowest along the edge and would not change significantly from the edge to the centre. For the part grown with R = 6 cm/h the average creep rate would be lowest along the edge, with the lowest value just after the start of growth, and would increase towards the centre where the creep rate would be the highest in the whole

bar. Just before the end of the growth with R = 6 cm/h, the creep rate would increase along the edge and decrease along the centre of the bar grown with R = 15 cm/h, with the creep rate "converging" to 5×10^{-7} s^{-1} at the end of the OFZ run (Figure 30a).

The average mass change along the edge and centre of the bar after isothermal oxidation at 800 °C for 100 h is shown in Figure 31a,b. The average mass change along the edge was calculated as $\Delta W/A = \{([\Delta W/A]_{1,\ R = 1.2\ cm/h})/7 + ([\Delta W/A]_{1,\ R = 6\ cm/h})/5 + ([\Delta W/A]_{1,\ R = 15\ cm/h})/5\}$ and along the centre of the bar as $\Delta W/A = \{([\Delta W/A]_{4,\ R = 1.2\ cm/h})/7 + ([\Delta W/A]_{4,\ R = 6\ cm/h})/5 + ([\Delta W/A]_{4,\ R = 15\ cm/h})/5\}$. The average mass change shown in Figure 31c was calculated as described above for the isothermal oxidation at 1200 °C.

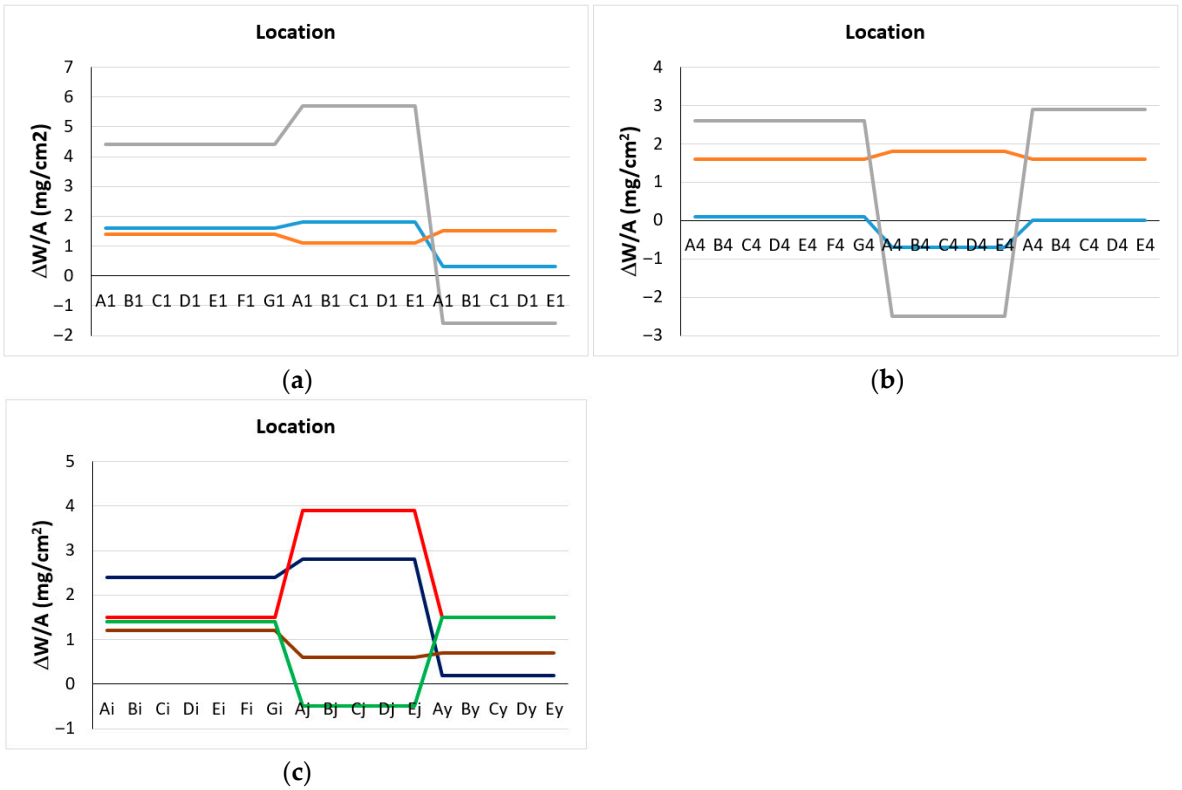

Figure 31. Calculated average mass change (see text) (**a**,**b**) for isothermal oxidation at 800 °C for 100 h along the length of the OFZ bar for locations at the edge and centre of the bar (see Figure 2b). Blue line for parameter VEC, grey line for parameter δ, and orange line for parameter Δχ. (**c**) Calculated average mass change (see text) for locations along the length of the OFZ bar. Locations are indicated as Ai–Bi–Ci–Di–Ei–Fi–Gi–Aj–Bj–Cj–Dj–Ej–Ay–By–Cy–Dy–Ey, where i, j, and y = 1 at the edge of the bar and i, j, and y = 4 at the centre of the bar (see Figure 2b). Colours are as follows: blue for i, j, and y = 1, red for i, j, and y = 2, brown for i, j, and y = 3, and green for i, j, and y = 4. Note that for the bar grown with R = 15 cm/h, the average mass change for i, j, and y = 2 and i, j, and y = 4 was the same, thus only the green line appears in (**c**).

NICE indicated (a) that the alloy would not suffer from pest oxidation at 800 °C, (b) that mass changes would be small, on average about 1 mg/cm^2 at the end of growth, and (c) that at 1200 °C there would be no catastrophic oxidation. Isothermal oxidation experiments at 800 C for 100 h using specimens of the cast alloy [9] confirmed (i) the absence of pest oxidation and (ii) low mass change of 1.5 mg/cm^2. Also, isothermal oxidation experiments at 1200 °C of the cast alloy confirmed (iii) no catastrophic oxidation and (iv) mass change of 26 mg/cm^2 after 100 h. Taking into consideration the existence of macrosegregation in the cast alloy [9], note the agreement of NICE of (a), (b), and (c) with (i), (ii), and (iii). Also, note the agreement of NICE with (iv) for the part of the OFZ bar that was grown with R = 6 cm/h (Figure 30b).

7. Implications for the Design and Development of Metallic UHTMs

This paper has shown that using OFZ processing and changing the growth rate during solidification, one can directionally grow a bar (i) contamination-free (see below) and (ii) with different chemical composition across its thickness (i.e., radially) and along its length (i.e., longitudinally). This was possible because (a) of the solute profiles that developed in the bar owing to macrosegregation in OFZ processing and (b) of the limitation (restriction, control) of oxygen to the "root" of the bar, where the oxygen was scavenged by Hf.

To put it another way, our research (see also [44]) could suggest that a component with a high aspect ratio, in principle, could be grown with different chemical composition from its "root" to its "tip" and across its thickness, and therefore with differing properties from "root" to "tip" and across its thickness. In other words, a component based on a metallic UHTM with "functionally graded" composition, microstructure, and properties could be directionally grown. Depending on the chemical composition of RCCA/RM(Nb)IC, contamination with oxygen could be controlled to enhance strength or to improve strength and ductility (depending on alloy composition) [1,4,7,85–87].

Dimension issues, for example, change in component diameter because of growth rate change(s), in principle, could be "handled" (taken care of successfully, managed, dealt with) (i) by optimisation of processing parameters and, if required, (ii) with machining. The functionality of the component could be tailored to the requirements of its application.

The alloy design methodology NICE enables the design and development of such a component. Indeed, processability issues, material and manufacturing costs, and material–environment interactions and properties are key in its "landscape" (see Sections 5 to 9 in [1]). For the design and development of such a "functionally graded" component, NICE uses (a) the macrosegregation of the alloy elements, which, as we demonstrated for the RCCA/RM(Nb)IC of this study, (1) can be significant depending on growth rates and (2) can persist for some elements, depending on growth rates, as demonstrated in the case of Si for the higher growth rate used in the research discussed in this paper, and (b) the synergy and entanglement (i) of macrosegregation with the parameters VEC, $\Delta\chi$, and δ, (ii) of the latter three parameters with each other and with the alloy elements, and (iii) of elements and phases. As a result of (a) and (b), the "emerging" properties of each part of the component along its length and across its thickness are calculated with NICE. Calculated "emerging" creep and oxidation properties for the directionally grown bar of this study were discussed in the previous section.

To our knowledge, research on the directional solidification of metallic UHTMs is still in its infancy (see Sections 2.2, 2.3, 2.3.1 and 2.3.2 and Section OFZ Processing of Metallic UHTMs). Currently, OFZ directionally grown metallic UHTMs are small (see Section OFZ Processing of Metallic UHTMs and this research), are produced one at a time, and their growth is (can be) slow (2.5 h in the case of the alloy of this study, see Section 3). Can OFZ processing be scaled up? Should alloy developers work closer with the producers of OFZ facilities?

8. Conclusions

With OFZ solidification processing, one could directionally grow a metallic UHTM with different microstructures radially and longitudinally because (i) of the solute profiles that develop owing to macrosegregation in the solidifying bar at a specific growth rate and as the growth rate increases, and (ii) of the synergy and entanglement of processing, the parameters VEC, $\Delta\chi$, and δ, the alloy elements, and the phases. In principle, a component based on a metallic UHTM with "functionally graded" composition, microstructure, and properties could be directionally grown.

Supplementary Materials: The following supporting information can be downloaded at: https://www.mdpi.com/article/10.3390/alloys4040029/s1.

Author Contributions: Conceptualization, P.T.; Software, C.U.; Investigation, N.T. and C.U.; Resources, P.T.; Writing—original draft, N.T.; Writing—review & editing, C.U. and P.T.; Supervision, C.U. and P.T.; Project administration, P.T.; Funding acquisition, P.T. All authors have read and agreed to the published version of the manuscript.

Funding: Engineering and Physical Sciences Research Council, No. EP/H500405/1; Engineering and Physical Sciences Research Council, No. EP/L026678/1.

Data Availability Statement: Data is contained within the article.

Acknowledgments: The support of this work by the University of Sheffield, Rolls-Royce Plc, and EPSRC (EP/H500405/1, EP/L026678/1) is gratefully acknowledged. We are grateful to Rolls-Royce and the University of Cambridge Rolls-Royce UTC in Advanced Materials for permission to use the OFZ facility and to R Thompson for assistance with its operation. For open access, the authors have applied a 'Creative Commons Attribution (CC BY) licence to any Author Accepted Manuscript version arising.

Conflicts of Interest: The authors declare no conflict of interest.

Abbreviations

AC	as-cast
CC	complex concentrated (also compositionally complex)
CEMI	correlative environment material interactions [1]
CCDS	cold crucible directional solidification
DS	directional solidification
ESSERE	entanglement synergy self-regulation [1]
ETS	evolution through survival [1]
FBD	fluidised bed quenching
GCC	gas cooling casting
HE	high entropy
HEA	high entropy alloy
HT	heat-treated
IDS	integral directional solidification
IRIS	interwoven risk [1]
LMC	liquid metal cooling
NICE	Niobium Intermetallic Composite Elaboration [10]
OFZ	optical floating zone
RM	refractory metal
RMIC	refractory metal intermetallic composite
RHEA	refractory metal high entropy alloy
RCCA	refractory metal complex concentrated alloy
RMIC/RHEA	RMIC that also meets the definition of RHEA
RM(Nb)IC	refractory metal intermetallic composite based on Nb
RM(Nb)IC/RCCA	RM(Nb)IC that also meets the definition of RCCA
RM(Nb)IC/RHEA	RM(Nb)IC that also meets the definition of RHEA
SM	simple metal
TM	transition metal
UHTM	ultra-high temperature material

Appendix A. RM(Nb)IC and RCCA/RM(Nb)IC Alloy Nominal Chemical Compositions (at.%)

EZ2	48Nb–24Ti–18Si–5Hf–5Sn [34]
EZ6	43Nb–24Ti–18Si–5Cr–5Hf–5Sn [34]
EZ8	38Nb–24Ti–18Si–5Al–5Cr–5Hf–5Sn [34]
NT1.1	33Nb–20Ti–19Si–5Al–5Cr–1Hf–5Ge–5Sn–6Mo–1W [11]
NT1.2	36Nb–20Ti–22Si–3.5Al–4Cr–1Hf–6Ge–1.5Sn–5Mo–1W [9]
OHS1	38Nb–24Ti–18Si–5Al–5Cr–5Ge–5Sn [12]
JG6	36Nb–24Ti–18Si–5Al–5Cr–5Hf–5Sn–2Mo [86]
JZ3	40.5Nb–12Ti–18Si–5Al–5Cr–1Hf–5Ge–5Sn–6Ta–2.5W [78]
JZ3+	38Nb–12Ti–18Si–5Al–5Cr–1Hf–5Ge–7.5Sn–6Ta–2.5W [78]
JZ4	43.8Nb–11.5Ti–18Si–4.7Al–4.5Cr–1Hf–4.6Ge–4.9Sn–5Mo–2W [13]
JZ5	36Nb–21Ti–18Si–3.7Al–4Cr–0.8Hf–4.2Ge–4.4Sn–6.7Mo–1.2W [13]
ZF6	43Nb–24Ti–18Si–5Al–5Cr–5Ge [74]
ZF9	38Nb–24Ti–18Si–5Al–5Cr–5Hf–5Ge [74]

References

1. Tsakiropoulos, P. A Perspective of the Design and Development of Metallic Ultra-High Temperature Materials: Refractory Metal Intermetallic Composites, Refractory Complex Concentrated Alloys and Refractory High Entropy Alloys. *Alloys* **2023**, *2*, 184–212. [CrossRef]
2. Senkov, O.N.; Miracle, D.B.; Chaput, K.J. Development and exploration of refractory High entropy alloys—A review. *J. Mater. Res.* **2018**, *33*, 3092–3128. [CrossRef]
3. Bewlay, B.P.; Jackson, M.R. Chapter 3.22—High-Temperature In Situ Composites: Processing and Properties. In *Comprehensive Composite Materials*; Anthony, K., Carl, Z., Eds.; Elsevier: Amsterdam, The Netherlands, 2000; pp. 579–615. ISBN 9780080429939. [CrossRef]
4. Tsakiropoulos, P. Alloys for application at ultra-high temperatures: Nb-silicide in situ composites: Challenges, breakthroughs and opportunities. *Prog. Mater. Sci.* **2022**, *123*, 100714. [CrossRef]
5. Tsakiropoulos, P. Refractory Metal Intermetallic Composites, High-Entropy Alloys, and Complex Concentrated Alloys: A Route to Selecting Substrate Alloys and Bond Coat Alloys for Environmental Coatings. *Materials* **2022**, *15*, 2832. [CrossRef] [PubMed]
6. Barwinska, I.; Kopec, M.; Kukla, D.; Senderowski, C.; Kowalewski, Z.L. Thermal Barrier Coatings for High-Temperature Performance of Nickel-Based Superalloys: A Synthetic Review. *Coatings* **2023**, *13*, 769. [CrossRef]
7. Tsakiropoulos, P. On the Stability of Complex Concentrated (CC)/High Entropy (HE) Solid Solutions and the Contamination with Oxygen of Solid Solutions in Refractory Metal Intermetallic Composites (RM(Nb)ICs) and Refractory Complex Concentrated Alloys (RCCAs). *Materials* **2022**, *15*, 8479. [CrossRef]
8. Tsakiropoulos, P. On the Nb_5Si_3 Silicide in Metallic Ultra-High Temperature Materials. *Metals* **2023**, *13*, 1023. [CrossRef]
9. Tankov, N.; Utton, C.; Tsakiropoulos, P. On the Microstructure and Properties of Complex Concentrated bcc Solid Solution and Tetragonal $D8_m$ M_5Si_3 Silicide Phases in a Refractory Complex Concentrated Alloy. *Alloys* **2024**, *3*, 59–95. [CrossRef]
10. Tsakiropoulos, P. On Nb Silicide Based Alloys: Alloy Design and Selection. *Materials* **2018**, *11*, 844. [CrossRef]
11. Tankov, N.; Utton, C.; Tsakiropoulos, P. Microstructure and Properties of Complex Concentrated C14–MCr_2 Laves, A15–M_3X and $D8_m$ M_5Si_3 Intermetallics in a Refractory Complex Concentrated Alloy. *Alloys* **2024**, *3*, 190–231. [CrossRef]
12. Hernández-Negrete, O.; Tsakiropoulos, P. On the Microstructure and Isothermal Oxidation at 800 and 1200 °C of the Nb-24Ti-18Si-5Al-5Cr-5Ge-5Sn (at.%) Silicide-Based Alloy. *Materials* **2020**, *13*, 722. [CrossRef] [PubMed]
13. Zhao, J.; Utton, C.; Tsakiropoulos, P. On the Microstructure and Properties of Nb-18Si-6Mo-5Al-5Cr-2.5W-1Hf Nb-Silicide Based Alloys with Ge, Sn and Ti Additions (at.%). *Materials* **2020**, *13*, 4548. [CrossRef] [PubMed]
14. Sha, J.B.; Hirai, H.; Tabaru, T.; Kitahara, A.; Ueno, H.; Hanada, S. High-temperature strength and room-temperature toughness of Nb–W–Si–B alloys prepared by arc-melting. *Mater. Sci. Eng.* **2004**, *364*, 151–158. [CrossRef]
15. Meng, X.; Liu, C.; Jiang, Y.; Wang, F.; Xu, Y.; Su, Y.; Guo, J.; Luo, L. Microstructure and high temperature compressive properties of Nb based alloys fabricated by plasma arc-induction hybrid melting. *Mater. Res. Express* **2019**, *6*, 056519. [CrossRef]

16. Juan, C.-C.; Tsai, M.-H.; Tsai, C.-W.; Lin, C.-M.; Wang, W.-R.; Yang, C.-C.; Chen, S.-K.; Lin, S.-J.; Yeh, J.-W. Enhanced mechanical properties of HfMoTaTiZr and HfMoNbTaTiZr refractory high-entropy alloys. *Intermetallics* **2015**, *62*, 76–83. [CrossRef]
17. Senkov, O.N.; Wilks, G.B.; Scott, J.M.; Miracle, D.B. Mechanical properties of $Nb_{25}Mo_{25}Ta_{25}W_{25}$ and $V_{20}Nb_{20}Mo_{20}Ta_{20}W_{20}$ refractory high entropy alloys. *Intermetallics* **2011**, *19*, 698. [CrossRef]
18. Bridgman, P.W. Certain Physical Properties of Single Crystals of Tungsten, Antimony, Bismuth, Tellurium, Cadmium, Zinc, and Tin. *Proc. Am. Acad. Arts Sci.* **1925**, *60*, 305–383. [CrossRef]
19. Bridgman, P.W. Crystals and Their Manufacture. U.S. Patent 1,793,672, 16 February 1926.
20. Stockbarger, D.C. The Production of Large Single Crystals of Lithium Fluoride. *Rev. Sci. Instrum.* **1936**, *7*, 133–136. [CrossRef]
21. Versnyder, F.L.; Shank, M.E. The development of columnar grain and single crystal high temperature materials through directional solidification. *Mater. Sci. Eng.* **1970**, *6*, 213–247. [CrossRef]
22. Giamei, A.F.; Tschinkel, J.G. Liquid metal cooling: A new solidification technique. *Metall. Trans. A* **1976**, *7*, 1427–1434. [CrossRef]
23. Nakagawa, Y.G.; Ohtomo, Y.; Sajga, Y. Heat Treatment, Microstructure, and Creep Strength of γ/γ'-α Eutectic Directionally Solidified by Fluidized Bed Quenching. In *Superalloys 1980*; Tien, J.K., Wlode, K.S.T., Morrow, H.I., Gell, M., Mauer, G.E., Eds.; American Society for Metals: Metals Park, OH, USA, 1980; pp. 267–274.
24. Konter, M.; Kats, E.; Hofmann, N. A Novel Casting Process for Single Crystal Gas Turbine Components. In *Superalloys 2000*; Pollock, T.M., Kissinger, R.D., Bowman, R.R., Green, K.A., McLean, M., Olson, S.L., Schirra, J.J., Eds.; TMS: Warrendale, PA, USA, 2000; pp. 189–200.
25. Schneider, M.C.; Gu, J.P.; Beckermann, C.; Boettinger, W.J.; Kattner, U.R. Modelling of micro- and macrosegregation and freckle formation in single-crystal nickel-base superalloy directional solidification. *Metall. Mater. Trans. A* **1997**, *28*, 1517–1531. [CrossRef]
26. Liu, L.; Huang, T.; Qu, M.; Liu, G.; Zhang, J.; Fu, H. High thermal gradient directional solidification and its application in the processing of nickel-based superalloys. *J. Mat. Proc. Techn.* **2010**, *210*, 159–165. [CrossRef]
27. Ma, S.G.; Zhang, S.F.; Gao, M.C.; Liaw, P.K.; Zhang, Y. A Successful Synthesis of the CoCrFeNiAl0.3 Single-Crystal, High-Entropy Alloy by Bridgman Solidification. *JOM* **2013**, *65*, 1751–1758. [CrossRef]
28. Liu, G.; Liu, L.; Liu, X.; Wang, Z.; Han, Z.; Zhang, G.; Kostka, A. Microstructure and mechanical properties of Al0.7CoCrFeNi high-entropy alloy prepared by directional solidification. *Intermetallics* **2018**, *93*, 93–100. [CrossRef]
29. Zheng, H.; Chen, R.; Qin, G.; Li, X.; Su, Y.; Ding, H.; Guo, J.; Fu, H. Microstructure evolution, Cu segregation and tensile properties of CoCrFeNiCu high entropy alloy during directional solidification. *J. Mater. Sci. Technol.* **2020**, *38*, 19–27. [CrossRef]
30. Xu, Y.; Li, C.; Huang, Z.; Chen, Y.; Zhu, L. Microstructure Evolution and Mechanical Properties of FeCoCrNiCuTi0.8 High-Entropy Alloy Prepared by Directional Solidification. *Entropy* **2020**, *22*, 786. [CrossRef]
31. Peng, P.; Li, S.; Chen, W.; Xu, Y.; Zhang, X.; Ma, Z.; Wang, J. Phase selection and mechanical properties of directionally solidified $AlCoCrFeNi_{2.1}$ eutectic high-entropy alloy. *J. Alloys Compd.* **2022**, *898*, 162907. [CrossRef]
32. Campo, K.N.; Wischi, M.; Rodrigues, J.F.; Starck, L.F.; Sangali, M.C.; Caram, R. Directional solidification of the $Al0.8CrFeNi_{2.2}$ eutectic high-entropy alloy. *J. Mater. Res. Technol.* **2024**, *30*, 8874–8881. [CrossRef]
33. Zhang, S.; Shi, X.; Sha, J. Microstructural evolution and mechanical properties of as-cast and directionally-solidified Nb-15Si-22Ti-2Al-2Hf-2V-(2, 14) Cr alloys at room and high temperatures. *Intermetallics* **2015**, *56*, 15–23. [CrossRef]
34. Zacharis, E.; Utton, C.; Tsakiropoulos, P. A Study of the Effects of Hf and Sn on the Microstructure, Hardness and Oxidation of Nb-18Si Silicide-Based Alloys-RM(Nb)ICs with Ti Addition and Comparison with Refractory Complex Concentrated Alloys (RCCAs). *Materials* **2022**, *15*, 4596. [CrossRef]
35. Tsakiropoulos, P. On the macrosegregation of silicon in niobium silicide based alloy. *Intermetallics* **2014**, *55*, 95–101. [CrossRef]
36. Bondarenko, Y.A.; Echin, A.B.; Kolodyazhnyi, M.Y. In situ Formation of the Composite Structure of a Eutectic Nb–Si Alloy during Directional Solidification in a Liquid-Metal Coolant. *Russ. Metall. (Met.)* **2017**, *2017*, 461–466. [CrossRef]
37. Ma, L.M.; Yuan, S.N.; Cui, R.J.; Tang, X.X.; Li, Y.L.; Gao, M.; Zhang, H. Interactions between Nb-silicide based alloy and yttria mould during directional solidification. *Int. J. Refract. Met. Hard Mater.* **2012**, *30*, 96–101. [CrossRef]
38. Huang, Y.; Jia, L.; Jin, Z.; Kong, B.; Guo, Y.; Sha, J.; Zhang, H. Effect of Sc on the microstructure and room temperature mechanical properties of Nb-Si based alloys. *Mater. Des.* **2018**, *160*, 671–682. [CrossRef]
39. Guo, H.; Guo, X. Microstructure evolution and room temperature fracture toughness of an integrally directionally solidified Nb–Ti–Si based ultrahigh temperature alloy. *Scr. Mater.* **2011**, *64*, 637–640. [CrossRef]
40. Guo, X.P.; Guo, H.S.; Yao, C.F.; Guan, P. Integrally Directionally Solidified Microstructure of an Niobium Silicide Based Ultrahigh Temperature Alloy. *Int. J. Mod. Phys. B* **2009**, *23*, 1093–1098. [CrossRef]
41. Fang, X.; Guo, X.; Qiao, Y. Microstructural transition of Nb-Si based alloy during directional solidification upon abruptly decreasing withdrawal rate. *J. Alloys Compd.* **2020**, *843*, 156073. [CrossRef]
42. Wang, S.; Wang, Q.; Chen, R.; Jin, Y.; Chen, D.; Wang, L.; Su, Y.; Guo, J.; Fu, H. Numerical analysis for solid-liquid interface shape at various temperature gradient in electromagnetic cold crucible directional solidification. *Int. J. Heat Mass Transf.* **2022**, *199*, 123443. [CrossRef]

43. Lu, Y.Y.; Zhang, J.; Tian, L.X.; Li, Y.L.; Ma, C.L. Microstructural Evolution of Unidirectionally Solidified Nb_{ss}-Nb_5Si_3 Eutectic Alloy. *Rare Met.* **2011**, *30*, 335–339. [CrossRef]
44. McCaughey, C.; Tsakiropoulos, P. Type of Primary Nb_5Si_3 and Precipitation of Nb_{ss} in αNb_5Si_3 in a Nb-8.3Ti-21.1Si-5.4Mo-4W-0.7Hf (at.%) Near Eutectic Nb-Silicide-Based Alloy. *Materials* **2018**, *11*, 967. [CrossRef]
45. Guo, J.T.; Tian, Y.; Cheng, G.; Zhou, L.; He, L.; Ye, H. Microstructural characteristics and high temperature compressive properties at 1623 K of a directionally solidified Nb-silicides based in-situ composite. *J. Alloys Compd.* **2009**, *470*, 606–609. [CrossRef]
46. Sekido, N.; Kimura, Y.; Miura, S.; Wei, F.-G.; Mishima, Y. Fracture toughness and high temperature strength of unidirectionally solidified Nb–Si binary and Nb–Ti–Si ternary alloys'. *J. Alloys Compd.* **2006**, *425*, 223–229. [CrossRef]
47. Tian, Y.; Cheng, G.; Guo, J.; Zhou, L.; He, L.; Ye, H. Microstructure and Mechanical Properties of Directionally Solidified Nb-22Ti-16Si-7Cr-3Al-3Ta-2Hf-0.1Ho Alloy. *Adv. Eng. Mater.* **2007**, *9*, 963–966. [CrossRef]
48. Fang, X.; Guo, X.; Qiao, Y. Microstructural characterization of integrally directionally solidified Nb-Si based alloys at high withdrawal rates. *Intermetallics* **2019**, *110*, 106481. [CrossRef]
49. Fang, X.; Guo, X.; Qiao, Y. Variation in morphology and crystallographic orientation of directionally solidified Nb–Si based alloys at high withdrawal rates. *J. Alloys Compd.* **2020**, *819*, 153023. [CrossRef]
50. Fang, X.; Guo, X.; Qiao, Y. Effect of Ti addition on microstructure and crystalline orientations of directionally solidified Nb–Si based alloys. *Intermetallics* **2020**, *122*, 106798. [CrossRef]
51. Wang, Y.; Guo, X.; Qiao, Y. Interactions between Nb-Si based ultrahigh temperature alloy and yttria matrix mould shells. *Mater. Des.* **2017**, *116*, 461–471. [CrossRef]
52. Yan, Y.; Ding, H.; Song, J. Solidification structure analysis of cold crucible directionally solidified Nb-Si based alloy. *Procedia Eng.* **2012**, *27*, 1033–1041. [CrossRef]
53. Kang, Y.; Yan, Y.; Song, J.; Ding, H. Microstructures and mechanical properties of Nb_{ss}/Nb_5Si_3 in-situ composite prepared by electromagnetic cold crucible directional solidification. *Mater. Sci. Eng. A* **2014**, *599*, 87–91. [CrossRef]
54. Bewlay, B.P.; Lipsitt, H.; Jackson, M.; Reeder, W.; Sutliff, J. Solidification processing of high temperature intermetallic eutectic-based alloys. *Mater. Sci. Eng. A* **1995**, *192–193*, 534–543. [CrossRef]
55. Bewlay, B.P.; Jackson, M.R.; Lipsitt, H.A. Ti-Modified Niobium-Silicide Based Directionally Solidified in-situ Composites. *MRS Online Proc. Libr.* **1996**, *460*, 715–725. [CrossRef]
56. Ding, H.; Nie, G.; Chen, R.; Guo, J.; Fu, H. Influence of oxygen on microstructure and mechanical properties of directionally solidified Ti–47Al–2Cr–2Nb alloy. *Mater. Des.* **2012**, *41*, 108–113. [CrossRef]
57. Zhang, M.; Chen, G.; Cai, Z.; Liu, J.; Tang, Y.D.; Hou, X.; Bai, S.; Li, C. A comparative study on the corrosion of Al_2O_3, MgO and $BaZrO_3$ refractory by TiZrNbV high-entropy alloy. *Ceram. Int.* **2023**, *49*, 37464–37474. [CrossRef]
58. He, J.; Wei, C.; Wang, S.; Meng, D.; Lu, X.; Wang, H.; Li, C. $BaZrO_3$ refractory applied to the directional solidification of TiAl alloys, in 4th International Conference on Advances in Solidification Processes (ICASP-4). *IOP Conf. Ser. Mater. Sci. Eng.* **2016**, *117*, 012033. [CrossRef]
59. Ning, S.-Y.; Yang, X.; Wang, Y.; Zhu, Z.; Zhang, J. Single crystal growth of GdB6 by the optical floating-zone technique. *Cryst. Eng. Comm.* **2020**, *22*, 8236. [CrossRef]
60. Xu, Y.; Loser, W.; Liu, L.; Buchner, B. Solidification and crystal growth of binary Tb_5Si_3 intermetallics. *J. Cryst. Growth* **2011**, *321*, 45–49. [CrossRef]
61. Cao, C.; Klingeler, R.; Leps, N.; Behr, G.; Löser, W. Single crystal growth of the $ErPd_2Si_2$ intermetallic compound. *J. Cryst. Growth* **2014**, *401*, 601–604. [CrossRef]
62. Xu, Y.-K.; Löser, W.; Guo, Y.-J.; Zhao, X.-B.; Liu, L. Crystal growth of Gd2PdSi3 intermetallic compound. *Trans. Nonferrous Met. Soc. China* **2014**, *24*, 115–119. [CrossRef]
63. Lee, S.-H.; Hagihara, K.; Oh, M.-H.; Nakano, T. Single-crystal growth and plastic deformation behaviour of a Ti-15Mo-5Zr-3Al alloy for biomedical application. *J. Phys. Conf. Ser.* **2009**, *165*, 012086. [CrossRef]
64. Johnson, D.R.; Inui, H.; Yamaguchi, M. Crystal growth of TiAl alloys. *Intermetallics* **1998**, *6*, 647–652. [CrossRef]
65. Šmilauerová, J.; Pospíšil, J.; Harcuba, P.; Holý, V.; Janeček, M. Single crystal growth of TIMETAL LCB titanium alloy by a floating zone method. *J. Cryst. Growth* **2014**, *405*, 92–96. [CrossRef]
66. Takesue, N.; Shimizu, Y.; Yano, T.; Hara, M.; Kuramoto, S. Single-crystal growth of Ti–Nb–Ta–Zr–O alloys and measurement of elastic properties. *J. Cryst. Growth* **2009**, *311*, 3319–3324. [CrossRef]
67. Bei, H. Directional Solidification, Microstructures and Mechanical Properties of Cr-Cr3Si Eutectic Alloys. Ph.D. Thesis, University of Tennessee, Knoxville, TN, USA, December 2003. Available online: http://trace.tennessee.edu/utk_graddiss/1958 (accessed on 1 March 2025).
68. Huang, Q.; Guo, X.-P.; Kang, Y.-W.; Song, J.-X.; Qu, S.-Y.; Han, Y.-F. Microstructures and mechanical properties of directionally solidified multi-element Nb-Si alloy. *Prog. Nat. Sci. Mater. Int.* **2011**, *21*, 146–152. [CrossRef]
69. Souptel, D. Crystal Growth and Perfection of Selected Intermetallic and Oxide Compounds. Ph.D. Thesis, Leibniz Institute for Solid State and Materials Research Dresden, Dresden, Germany, 2005.

70. Miura, S.; Murasato, Y.; Ohkubo, K.; Kimura, Y.; Sekido, N.; Mishima, Y.; Mohri, T. Microstructure control of Nb-Si alloy doped with Zr and Mg through eutectic and eutectoid reactions and its deformation behaviour. *Mater. Res. Soc. Symp. Proc.* **2007**, *980*, 327–332.
71. Bewlay, B.P.; Sitzman, S.D.; Brewer, L.N.; Jackson, M.R. Analyses of eutectoid phase transformations in Nb-silicide in-situ composites. *Microsc. Microanal.* **2004**, *10*, 470–480. [CrossRef]
72. Tsakiropoulos, P. Alloying and Properties of C14–$NbCr_2$ and A15–Nb_3X (X = Al, Ge, Si, Sn) in Nb–Silicide-Based Alloys. *Materials* **2018**, *11*, 395. [CrossRef]
73. Tsakiropoulos, P.; Zelenitsas, K.; Vellios, N. Study of the effect of Al, Cr and Sn additions on the microstructure and properties of Nb silicide based alloys. *Mater. Res. Soc. Symp. Proc.* **2011**, *1295*, 367–372. [CrossRef]
74. Li, Z.; Tsakiropoulos, P. On The Microstructures and Hardness of The Nb-24Ti-18Si-5Al-5Cr-5Ge and Nb-24Ti-18Si-5Al-5Cr-5Ge-5Hf (at.%) Silicide Based Alloys. *Materials* **2019**, *12*, 2655. [CrossRef]
75. Tsakiropoulos, P. Refractory Metal (Nb) Intermetallic Composites, High Entropy Alloys, Complex Concentrated Alloys and the Alloy Design Methodology NICE—Mise-en-scène † Patterns of Thought and Progress. *Materials* **2021**, *14*, 989. [CrossRef]
76. Nelson, J.; Ghadyani, M.; Utton, C.; Tsakiropoulos, P. A Study of the Effects of Al, Cr, Hf, and Ti Additions on the Microstructure and Oxidation of Nb-24Ti-18Si Silicide Based Alloys. *Materials* **2018**, *11*, 1579. [CrossRef]
77. Thandorn, T.; Tsakiropoulos, P. On the microstructure and properties of Nb-Ti-Cr-Al-B-Si-X (X=Hf,Sn,Ta) refractory complex concentrated alloys. *Materials* **2021**, *14*, 7615. [CrossRef]
78. Zhao, J.; Utton, C.; Tsakiropoulos, P. On the Microstructure and Properties of Nb-12Ti-18Si-6Ta-5Al-5Cr-2.5W-1Hf (at.%) Silicide-Based Alloys with Ge and Sn Additions. *Materials* **2020**, *13*, 3719. [CrossRef] [PubMed]
79. Zacharis, E.; Utton, C.; Tsakiropoulos, P. A Study of the Effects of Hf and Sn on the Microstructure, Hardness and Oxidation of Nb-18Si Silicide Based Alloys without Ti Addition. *Materials* **2018**, *11*, 2447. [CrossRef] [PubMed]
80. Tsakiropoulos, P. On the Alloying and Properties of Tetragonal Nb_5Si_3 in Nb-Silicide Based Alloys. *Materials* **2018**, *11*, 69. [CrossRef] [PubMed]
81. Tsakiropoulos, P. On the Desing of Ultra-High-Temperature Material Systems. *Materials* **2025**, *18*, 5203. [CrossRef]
82. Drawin, S.; Heilmaier, M.; Jehanno, P.; Hu, D.; Belaygue, P.; Tsakiropoulos, P.; Vilasi, M. Creep and oxidation resistance of refractory metal silicide based materials. In Proceedings of the 17th International Plansee Seminar 2009, International Conference on High Performance P/M Materials, Reutte, Austria, 25–29 May 2009; Volume 4.
83. Tsakiropoulos, P. Alloys. U.S. Patent 10,227,680 B2, 12 March 2019.
84. Graham, S.J.; Gallagher, E.; Baxter, G.J.; Azakli, Y.; Weeks, J.; Gelmetti, M.; D'SOuza, N.; Boettcher, C.; Roebuck, B.; Tsakiropoulos, P.; et al. Powder production, FAST processing and properties of a Nb-silicide based alloy for high temperature aerospace applications. *J. Mater. Res. Technol.* **2024**, *28*, 3217–3224. [CrossRef]
85. Vellios, N.; Keating, P.; Tsakiropoulos, P. On the Microstructure and Properties of the Nb-23Ti-5Si-5Al-5Hf-5V-2Cr-2Sn (at.%) Silicide-Based Alloy—RM(Nb)IC. *Metals* **2021**, *11*, 1868. [CrossRef]
86. Vellios, N.; Tsakiropoulos, P. The Effect of Fe Addition in the RM(Nb)IC Alloy Nb–30Ti–10Si–2Al–5Cr–3Fe–5Sn–2Hf (at.%) on Its Microstructure, Complex Concentrated and High Entropy Phases, Pest Oxidation, Strength and Contamination with Oxygen, and a Comparison with Other RM(Nb)ICs, Refractory Complex Concentrated Alloys (RCCAs) and Refractory High Entropy Alloys (RHEAs). *Materials* **2022**, *15*, 5815. [CrossRef]
87. Geng, J.; Tsakiropoulos, P. A study of the microstructures and oxidation of Nb–Si–Cr–Al–Mo in situ composites alloyed with Ti, Hf and Sn. *Intermetallics* **2007**, *15*, 382–395. [CrossRef]